Mathematical Modelling of Embryonic Tissue Development

Thesis submitted in accordance with the requirements of the University of Liverpool for the degree of Doctor in Philosophy by

Abdulaziz Rasheed Abdullah

May 2018

Acknowledgements

I would first and foremost like to express deep gratitude to my excellent supervisor, Dr Bakhtier Vasiev, for his help, guidance and patience throughout these years of my PhD project. I would also like to thank Dr Nigel Harrison and Dr Demetri Avrram for their assistance and valuable discussions on the research. My appreciation goes to the Ministry of Higher Education and Scientific Research of Iraq for allowing me the opportunity to study for my PhD at the University of Liverpool. I would also like to express my appreciation to my wife, Kurdistan Jarjees, and to our wonderful children, Omar, Rozheen, Saman and Dariyan for their constant support, patience, and encouragement. In addition, I wish to express my special appreciation to my mother and to my late father, also to my sisters and brothers for their lifelong support and encouragement. Finally, but not in the least, I wish to acknowledge my uncle, the late Mr. Hassan, and my aunt, the late Mrs. Mastikhan, for their unfailing kindness and generosity during the very happy childhood that I spent with them.

Abstract

Computational mathematics plays a significant role in the analysis and understanding of the outcomes of biological observations. Modelling cells and tissues is a current topic in mathematical biology. In this work, various mathematical tools including the vertex dynamics model that is implemented, for simulations, by the open software, Chaste, were used to investigate cellular dynamics in epithelial tissues. The results can be split into three parts:

1. Using the vertex dynamics model, mechanical properties of epithelial cells were studied by exposing them to stretching and contraction. The outcomes of numerical simulations, as well as of analytical studies, indicate that the vertex dynamics model confirms the elastic properties of cells.

2. Using the vertex dynamics model as well as analytical tools, topological features of epithelial tissue in the case of cell divisions, namely the distribution of cells according to the number of their edges, were studied. It was found that the histograms obtained via this model reproduced the experimental observations fairly well. Moreover, an analytical model of growing tissue which explained and reproduced topological features of epithelial tissues was developed. Also, a cellular automata model was developed that also confirmed the universal nature of epithelial tissue topology.

3. The vertex dynamics model was modified in a way that it reproduced dynamical changes in the cell shapes observed in the epithelial tissues. The model provided an explanation of patterns of cell migration and cell shape changes observed in experiments. Using this modification to investigate the impact of cellular dynamics, namely the rearrangement of cells and particularly the T1-transition (i.e. switching process of connected edge with their neighbours) processes, on tissue topology, it was found that the histograms of cell-edge distribution (CED) are approximately identical to that formed by proliferating cells.

A paper constructed from the results, short version, of chapter three and four, was submitted to the Journal of Physical Review Letters and also published in arXiv: 1710.08527 (1).

Contents

List of Figures **9**

List of Tables **12**

1 Introduction **14**

1.1 Biological background 14

1.1.1 Cells 15

1.1.2 Cytoskeleton and its role in cell movement 16

1.1.3 Mechanics of the cytoskeleton 20

1.1.4 Epithelial tissue 22

1.1.5 Cell division 23

1.2 Mathematical studies of cellular dynamics 26

1.2.1 The Potts models 27

1.2.2 The cell-centre model 28

1.2.3 The vertex dynamics model 28

1.2.4 The GPNP model 30

1.2.5 The SCWN models 33

1.3 Some important previous models and rules 35

1.3.1 Lewis' experiments 36

1.3.2 Aboav-Weaire's Law 37

1.3.3 Kolmogorov's Concept 38

1.4 The vertex dynamics model with Chaste 39

1.4.1 The Chaste implementation of the vertex dynamics model . . 41

1.5 Aim of this these 42

1.6 Remainder of thesis overview 43

2 Mechanical properties of tissue in Chaste implementation of the vertex dynamics model 45

2.1 Introduction . . . 46

2.2 Forces in the vertex dynamics model . . . 48

2.2.1 The tension force . . . 49

2.2.2 The resistance to the deformation due to incompressibility (deformation force) . . . 50

2.2.3 The perimeter force . . . 51

2.3 Simulation of the tissue using Chaste . . . 52

2.4 Numerical study of relaxation of deformed tissue . . . 60

2.4.1 The case of a single cell . . . 61

2.4.2 The case of tissue containing $N \times N$ ($N \in Z^+$) cells . . . 63

2.4.3 The case of a single cell and modified model, applying forces F_d, F_p and F_e (F_e instead of F_i) . . . 64

2.4.4 Case of a single cell and modified model with applying forces F_d, and F_e (F_e instead of F_i) . . . 64

2.5 Analysis of the dynamics of a single deformed cell . . . 66

2.6 Analysis of the dynamics of deformed tissue of infinite size . . . 75

2.7 Conclusions . . . 78

3 Mathematical study of epithelial tissue topology 80

3.1 Introduction . . . 81

3.2 Numerical simulation using the vertex dynamics model . . . 85

3.2.1 CEDH for growing tissue in numerical simulations . . . 86

3.2.2 Verification of Aboav's Law in numerical simulations . . . 87

3.2.3 Dependence of the frequency of cellular division on the number of edges of dividing cell . . . 91

3.3 Analytical model describing the evolution of CEDH in epithelial tissue 92

3.3.1 Three scenarios of cellular division . . . 94

3.3.2 Linear model . . . 96

3.3.3 Nonlinear model . . . 99

3.4 Cellular automata model . . . 101

3.5 Conclusion . . . 103

4 Modelling cellular mixing in epithelial tissue **107**

4.1 Introduction . . . 108

4.2 Feedback mechanism in the definition of tension force allows dynamic changes in tissue . . . 110

4.3 Cell-edge distribution in simulations of dynamic tissue undergoing cellular mixing . . . 112

4.4 Analytical model for cell-edge distribution in tissue with cellular mixing 115

4.4.1 Master equations . . . 115

4.4.2 Eigen-solution for the linear model . . . 117

4.4.3 Nonlinear model . . . 119

4.4.4 Cellular automata model for the dynamics of cell-edge distribution in the course of cell mixing . . . 119

4.5 Conclusion . . . 120

5 Conclusions and discussion **122**

5.1 The fundamental findings . . . 122

5.2 Elasticity behaviour in epithelial tissue . . . 124

5.3 The characteristics of the cell-edge distribution model for the cell divisions . . . 126

5.4 The characteristics of the cell-edge distribution model pertaining to plastic deformation . . . 128

5.5 Future research . . . 129

A Appendix **131**

A.1 GPNP model and the second SCWN model . . . 131

A.2 First and third SCWN models . . . 132

A.3 Analytical model represented by master equations in the case of cell division. . . . 132

A.4 Cellular automata model in the case of cell division . . . 134

A.5 Analytical model that is represented by master equations in the case of plastic deformation . . . 136

A.6 Cellular automata model in the case of plastic deformation . . . 137

B Appendix **139**

B.1 How to install and deal with Chaste 139

Bibliography **141**

List of Figures

1.1 The three fundamental cytoskeletal elements in the epithelial cells. . . 17
1.2 An image of a cell where microtubules are clearly visible 20
1.3 Different classes of polarized epithelial cell junctions and their interactions with the elements of two connected cells 24
1.4 View of the apical side of epithelial tissue in vitro 24
1.5 Illustration of the phases that the eukaryotic cell undergoing during its cell cycle 25
1.6 Schematic representation of the Potts modell. 28
1.7 Schematic representation of the cell-centre model. 29
1.8 Distribution of cells according to the number of edges in experiments 33
1.9 Comparison of histograms obtained using the three modifications of SCWN model with experimental data 34
1.10 Junction rearrangement during T1-transition 40

2.1 Fragment of virtual tissues modelled by the vertex dynamics model and show the effect of the forces. 49
2.2 Fragment of virtual tissue modelled by the vertex dynamics model . . 50
2.3 Illustration of the tissue collapse in the absence of the deformation force, F_d 53
2.4 Tissues formed by regular hexagonal cells are shown 55
2.5 The relation between the number of cells and the time that these cells need to reach the destination area. 56
2.6 Area of cells as a function of model parameters where only two forces F_d with F_i or F_d with F_p are applied. 57

2.7 Area of cells as a function of model parameters where all three forces F_d, F_i, and F_p are applied. 58
2.8 Elastic deformation 59
2.9 Plastic deformation 59
2.10 Migration of group of cells under the influence of the external force . 60
2.11 The exponential behaviour of the relaxation after stretching/shrinking a single cell with applying forces: 61
2.12 The exponential relaxation of a stretched single cell 15% in the y-axix direction after the cell subjected to the forces F_d, F_i and F_p, the parameters were in the default values. 62
2.13 The exponential behaviour of the relaxation after shrinking more than one cell 64
2.14 The exponential relaxation and the relaxation times for a stretched cell when the forces F_d, F_e and F_p are applied 65
2.15 The exponential relaxation and the relaxation times for a stretched cell when the forces F_d and F_e are applied 65
2.16 The hexagon cell with vertices 67
2.17 A domain of infinite tissue formed by regular hexagonal cells 76

3.1 Experimental images and data 82
3.2 Frequency of cellular divisions as depending on the number of edges of dividing cell 84
3.3 CEDH from simulations on vertex model as compared with the CEDH obtained by GED 87
3.4 Bar charts showing fractions of j-sided cells neighbouring i-sided cells 89
3.5 Aboav relationship for the virtual tissue obtained in numerical simulation using the vertex model: 90
3.6 Frequencies of j-sided cells (bars) neighbouring i-sides cells (panels). . 90
3.7 Correlation between the frequency of cell division and the number of edges i of mother cell in numerical simulations on the vertex model. Error bars represent standard deviation and best fit exponential function is shown. 92
3.8 Division of hexagonal cell into two identical daughter cells. 93

3.9 Possible division scenarios of i-sided mother cells and corresponding sidedness of daughter cells 95
3.10 CEDHs obtained in three versions (differing on probabilities of different division scenarios) of linear model as compared with the experimental CEDH. The Matlab codes are presented in Appendix A.3. 99
3.11 CEDHs obtained in the versions of analytical model with included dependence of the frequency of cellular division on the sidedness of dividing cell 100
3.12 CEDHs obtained in the versions of analytical model with included dependence of the frequency of cellular division on the sidedness of dividing cell in comparison with the CEDHs that obtained by experimental observations and by simulation results. 101
3.13 Histograms of theoretical cell-edge distribution. 102
3.14 CEDHs obtained for the cells with 4 to 8, 9, 10 and 11 edges. 105
3.15 CEDHs of the dependent (using exponential relationship) and independent automata models in comparison to the experimental observations. 106

4.1 The cells undergo topological changes as a result of T1-transitions which change the area and the number of vertices (and edges) of cells. 113
4.2 Comparison of cell-edge distribution obtained in experiments (black bars) and simulations 114
4.3 Frequency of n-sided cells gaining (a_n^+) and loosing (a_n^-) an edge in the course of T1-transitions as obtained from numerical simulations using the vertex model. Best fit means best fitting exponential function. 115
4.4 Cell-edge distribution predicted by the linear model is uniform (yellow bars) and is not comparable with experimental data, LZED, (grey bars). 117
4.5 Cell-edge distribution in nonlinear model as compared with the experimental observations and simulations 120
4.6 Cell-edge distribution in three realisations of cellular automata model as compared with the experimental observations, LZED, (grey) 121

List of Tables

1.1 Data on the frequencies of cells representing polygons with different number of edges and their involvement in cellular division 36

2.1 The relaxation times (τ) for the three situations that are shown in Figure 2.11. 62

2.2 The relaxation times (τ) for the 2×2 and 3×3 number of cells and applying F_d, F_i and F_p. 63

2.3 The relaxation times (τ) for the $N \times N$ number of cells and applying F_d, F_i and F_p, where $N = 1, 2, ..., 10$. The parameters at default values. 64

3.1 Numbers of j-sided cells neighbouring i-sided cell (where $i, j = 4, ..., 9$) found in the numerical simulation. 88

Nomenclature, symbols and abbreviations

CED	Cell-edge distribution
CEDH	Cell-edge distributions histogram
CNN	Cell's number of neighbours
Nm	Newton metre
GPa	GigaPascal (GPa = 10^9 N.m^{-2})
GPNP	Abbreviation of the surnames of the authors
SCWN	Abbreviation of the surnames of the authors
pN	picoNewton (1 pN= 1×10^{-12} N-Newton)
F_i	The tension force
F_d	The deformation force
F_p	The perimeter force
nm	nanometre
LED	Lewis's experimental data
GED	Gibson's experimental data
LZED	La Porta-Zapperi experimental data
σ	The parameter of the deformation force
ρ	The parameter of the tension force
γ	The parameter of the perimeter force

Chapter 1

Introduction

Mathematical modelling is one of the fundamental methods that is widely used nowadays in studies of biological systems in order to understand the accumulated experimental information (66; 67). It is applied to studies of topological characteristics of cells, including changes in cell shape, cell division and rearrangement of cells in tissues. This is often combined with the study of the mechanical properties of cells underlying these cellular processes.

The understanding of mechanisms of cellular migration associated with the early stages of the organism's development is another important area of application of the computational models (13). For example, modelling the behaviour of epithelial cells in a *Drosophila* embryo is considered as a powerful tool in the investigation and understanding of developmental processes in biological tissues.

Mathematics has recently been employed in studies of many serious diseases, such as cancer, that result from the abnormal cell divisions. Through the modelling, attempts are made to understand the initiation, growth and migration of the resulting cells. Mathematical modelling is often accompanied by computer simulations, which are the most widely used methods to find the outcome of the model, thus helping, research into pathology can be further developed (52).

1.1 Biological background

Biology focuses on understanding life and organisms on the planet, whether in the past, present, or future. This science studies the physical and chemical properties of

living organisms, alongside aspects of an organism's development and the evolution of living things, in microscopic, molecular and cellular, and macroscopic scales (92).

During the last two centuries and through experimental observations, scientists have realised that the study and understanding of the cells' complex structure and their multi-function are of vital important. Cell studies provide an explanation for underlying causes of diseases and enable researchers to interpret the differences between the organisms biologically, and how these various organisms can generate new generations faithfully or with some mutations (6). Mathematical models are indispensable for dealing with complex phenomena of this kind, where the mathematics not only supplies the quantitative methods to organize, examine and understand the massive amount of data but also is used to construct models that help to simulate the biological processes and reveal mechanisms that would be difficult to establish experimentally. Therefore, these simulations present the optimum solutions for investigating these mechanisms.

Building a useful and an objective biological mathematical model requires that the model is based on the most significant biological relevant factors, where the more reliable model is the one that predicts the manner in which the process will respond to introduced conditions and predicts next future experiments to be performed (66; 67).

1.1.1 Cells

Cells are considered as the principal units of life. There are two types of cells: the eukaryotic cell that contains a nucleus which stores most of the genetic material, and the prokaryotic cell that lacks a nucleus, with the genetic material distributed in the cytoplasm (6; 57).

In the multicellular organisms, the differentiated cells that have a distinctive structure and have the same functions are often assembled into a tissue. Cells of a certain tissue work together cooperatively to carry out a particular task. There are four main kinds of tissue that form the organs of animals, namely epithelial, muscular, nervous, and connective. epithelial cells are covering the outer surface of the body and also lining the inside body cavity (4). Later in this chapter, epithelial cells are described in further detail. Muscle cells carry out a highly specialized

task—contraction. In vertebrates, there are three different types of muscle cells; skeletal muscle for producing voluntary movements such as walking; cardiac muscle and smooth muscle for producing involuntary movements such as heart pumping and the intestine, respectively (4). Nerve cells, or neurons, execute highly specialized service that is receiving and transmitting signals throughout the body. For example, neurons of the eye and ear transmit signals to the brain and spinal cord (4). There are various kinds of connective tissues such as adipose, tendons, bone, cartilage and red blood. These tissues made up from different type of cells (adipocytes, fibroblast, osteoblasts, chondrocytes, erythrocytes, respectively). Each of these connective tissues has a different task, for example, bones help in movement and red blood function in oxygen transport (16).

Cells have various complex components that are used for many different functions. For example, the plasma membrane is central to enclose and maintain the cell as a unit of life; it surrounds and protects the interior components of the cell by segregating it partially from its environment. The membrane is a dynamic fluid structure, which is semi-permeable, that regulates the transport of ions and molecular materials that cross the membrane from one side to the other. There are many other functions of the membrane, such as its role in connecting the neighbouring cells to each other, in the transducing of the chemical signalling and in the connecting of the cytoskeleton networks. Many components of the cell are inside the plasma membrane, including the cytoplasm which composes all the internal content of a cell except the nucleus; the nucleus that contains the DNA; the mitochondria that generate the energy; the cytoskeletal components that control the shape and the movement, and many other organelles and vesicles (6; 57). The next subsection is centred on the role of the cytoskeleton in the mechanical properties of eukaryotic cells, especially the epithelial cells.

1.1.2 Cytoskeleton and its role in cell movement

Cytoskeleton is a dynamic network of protein filaments that provides the structural strength to cells. The cytoskeleton is comprised of three fundamental types of filaments: actin filaments (microfilaments), intermediate filaments and microtubules. Furthermore, the actin-binding proteins are essential components

of the actin cytoskeleton. Molecular motor proteins such as myosin, kinesins, and dynein families convert chemical energy to mechanical work to generate force and movement. The cytoskeletal elements, in association with molecular motor proteins, use the external energy sources and play a crucial role in many cellular processes such as cell migration, adhesion, organelle and vesicle transport, ion gradient generation and cell division (12; 15).

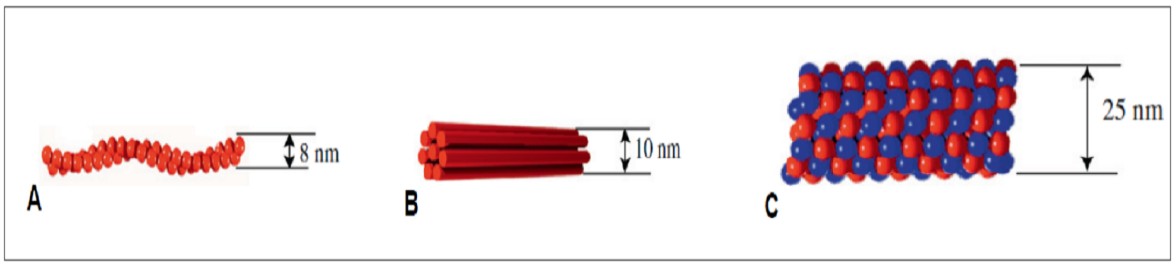

Figure 1.1: The three fundamental cytoskeletal elements in the epithelial cells. (A) Actin filament. (B) Intermediate filament. (C) Microtubule. The figure is taken from (90).

Actin filaments (Figure 1.1A): Actin is the (cytoskeleton) protein most abundant in the majority of cells. It is in the form of globular monomer, G-Actin, which can polymerize to a filamentous form, F-actin. Actin filament, which is a dynamic structure, has two ends, bared (+) end and the pointed (-) end. These filaments fall into two structures, two-dimensional bundles or three-dimensional elastic networks with semisolid gel properties, where actin filaments are being cross-linked via other associated proteins (15; 47). Actin-binding proteins play a crucial role in a variety of actin activities such as assembly and disassembly of actin filaments, formation of bundles and networks that are mediated by cross-linking and their interaction with cell membrane and other cytoskeletal elements (5; 91).

Actin filaments polymerize from G-Actin monomers. An actin filament can be considered as two parallel proto-filaments that twist around each other in order to constitute a right-handed helix of approximately 8 nm in diameter, the main mechanical element of the cytoskeleton (90). The connection of actin network with the transmembrane adhesion proteins generates pathways for chemical signals from the external cell environment that enable cells to react to both mechanical and chemical signals (46).

Actomyosin, a product of an interaction between actin and myosin, has a central

role in muscle contraction and many non-muscle movements such as cell division, where myosin converts the chemical energy of adenosine-triphosphate (ATP) to generate forces and movement. Although there are different types of myosins and each of them has a different function in the cell such as myosin I that helps to transport vesicles and organelles, all myosins use the actin filaments to create movement (15).

Intermediate filaments (Figure 1.1B): Intermediate Filaments (IFs) in many vertebrate cells and tissues represent a primary element of the cytoskeleton system (19). They are approximately 10 nm in diameter, which is between the diameter of actin filaments and that of the microtubule filaments. Despite the diversity of the proteins that constitute the intermediate filaments, these fibrous proteins share common structural features (5; 15; 77).

The different intermediate proteins, more than 65 (15), can be categorized into five main classes based on their similarities in the biochemical characteristics of amino acid, a small organic molecule representing the building blocks of proteins and in the structure of the associated genes. The types I and II comprise two classes of keratin filaments that are found exclusively in epithelial cells. The type III intermediate filaments comprise vimentin, which is found in a number of cells types, such as white blood cells, and desmin, which is especially found in muscle cells. The type IV intermediate filament proteins are the neurofilaments, which are expressed in nerve cells. The type V intermediate filaments are known as nuclear lamins, which are fibrous proteins lining the nucleus of many eukaryotic cells. The first four types of intermediate filaments are found in the cytoplasm, while the latter is found in the nucleus. Fibrous filaments for each type are constituted by assembling their constituent intermediate filament subunits. Each proto-filament of the intermediate filament consists of an alpha-helical rod domain and two terminals, the head and tail domains. The assembling of proto-filaments constitutes the intermediate filaments (5; 15; 77).

Intermediate filament proteins have a high tensile strength. They are more stable and durable than the other two elements of the cytoskeleton and they play the central role in not only providing the mechanical strength, thereby regulating the structures of the cells and tissues, but also in providing a scaffold for the positioning

of the cellular processes. The mechanical strength of cells enables them to resist the mechanical stress when they undergo stretching. The distributing effect of the topically applied forces is one of the most important functions of the intermediate filaments. This distribution helps the epithelial cells to maintain themselves and prevents their membranes from tearing as a result of the mechanical shear (5).

Microtubule filaments (Figure 1.1C): Microtubules are dynamic structures that are built from subunits called tubulin, which are dimers consisting of two globular proteins: α-tubulin and β-tubulin. These dimers polymerize to constitute microtubules. They have hollow cylindrical structures, 25 nm in diameter, and are composed of 13 parallel proto-filaments. Microtubules in all eukaryotic cells not only have an important role in determining cell shape and in regulating many cell movements associated with actin filaments, but also play a critical role in organizing and in separating chromosomes from the daughter cells during mitosis. Entering the process of mitosis allows the cytoplasmic microtubules to enter the process of disassembling and then reassembling in order to constitute a complex structure termed mitotic spindle (5; 15).

The two important molecular motors, kinesin and dynein, use the microtubules to move along in opposite directions. The microtubule has two ends (+) and (-): kinesin moves toward (+) end and dynein moves towards (-) end for transporting many intracellular components such as vesicles and organelles, where kinesin and dynein convert chemical energy into mechanical work using Guanosine-triphosphate (GTP) hydrolysis. Moreover, beating cilia and flagella are stable structures that microtubules can also form in eukaryotic cells to enable cells to swim or remove fluid from their surfaces (5; 15).

The microtubules (green) and the nucleus (blue), are shown clearly in the Figure 1.2, on image taken from research undertaken by the author in the Institute of Molecular and Cellular Anatomy (MOCA), University of Aachen as a part of the work within the workshop " Multimodal monitoring of cell migration (CGPW05)" that was held from 27^{th} to 31^{st} of July 2015.

Gomez and his co-workers (28) observed that in the epithelial cells the microtubule organization that lies underneath the apical surface and that occurs at the same time as epidermal cell elongation during the development of *Drosophila*

embryos is responding to perturbations in the cell shape. This observation can be shown in varied epithelia (28).

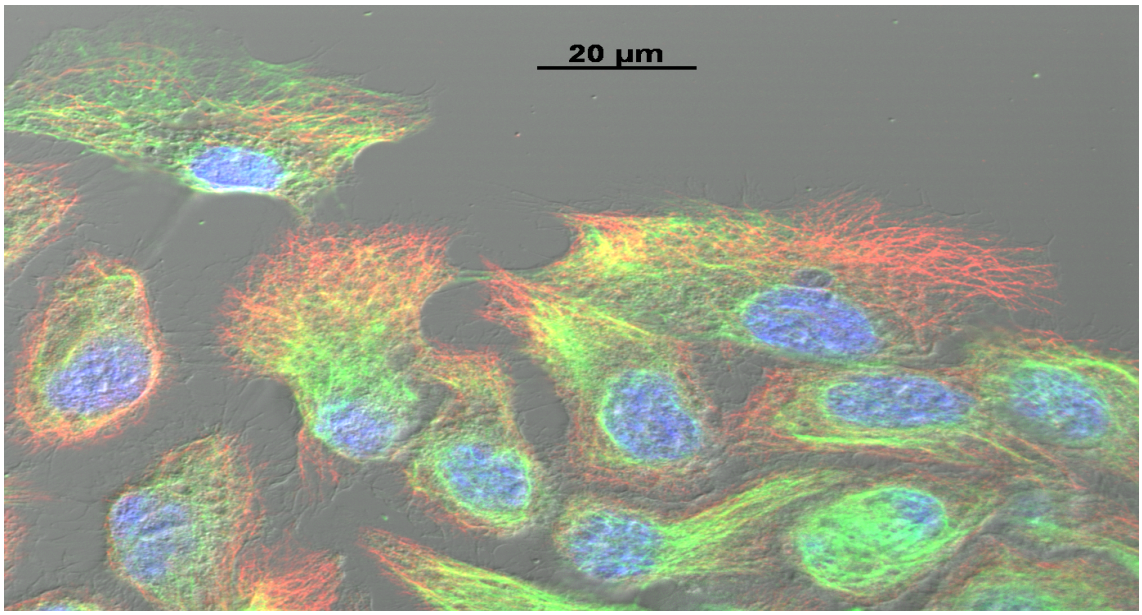

Figure 1.2: An image of a cell where microtubules (green) and nucleus (blue) are clearly visible. The picture was produced by the author during his trip to the summer school in RWTH Aachen University.

The epithelial monolayer sheets were the focus of this study.
In conclusion, we note that the cytoskeletal elements especially the actomyosin play a central role in determining the mechanical properties of epithelial cells.

1.1.3 Mechanics of the cytoskeleton

Knowing the mechanical properties of the cytoskeletal filaments and the location of these filaments inside the cytoplasm as well as the geometry of their crosslinking proteins gives a solid base to understand and predict the mechanical properties of cells (42).

The persistence length, L_p, is the parameter that describes the resistance of the filament to the thermal forces, which is defined as follows:

$$L_p = \frac{EI}{kT} \tag{1.1}$$

where k is the Boltzmann constant ($k = 1.3806 \times 10^{-21} J/K$) and T represents the absolute temperature. $kT = 4.116 \times 10^{-21}$ Nm at the standard temperature

$25°C$ (298.15 K. EI is the flexural rigidity (resistance generated by a structure undergoing bending), E refers to Young's modulus and I refers to the second moment of inertia (42).

Gittes and his co-workers (26) attempted to measure the persistence length of actin and microtubules filaments using the observations of thermal fluctuations in their shape. The flexural rigidities were estimated to be 7.3×10^{-26} Nm^2 and 2.1×10^{-23} Nm^2 of phalloidin-stabilized actin filaments, with Young's module 2.6 GPa, and taxol-stabilized microtubule filaments, with Young's module 1.2 GPa, respectively. Subsequently, according to the Equation (1.1), the persistence length of the actin filaments is $\sim$ 17.7 μm and of the microtubule filaments is $\sim$ 5 mm. Other observations, using different techniques, found that the persistence length of actin filaments is $\sim$ 15 μm and of the microtubule filaments is $\sim$ 6 mm (42).

Regarding the pure and hydrate intermediate filaments, the flexural rigidity is very low. The electron micrographs show the persistence length is $\sim$ 1 μm for neurofilaments and $\sim$ 3 μm for vimentin (42).

The relaxation time can be used to give information about the time that the shape of a filament takes to change. The relaxation time can be expressed as follows:

$$\tau_n \cong \frac{\vartheta}{EI}\left[\frac{L}{\pi(n+1/2)}\right]^4, \qquad n = 1, 2, 3, ... \tag{1.2}$$

where ϑ is the coefficient of the perpendicular drag per unit length of a filament (cylinder) near a surface, Here n and L are mode number and the length of the filament, respectively. ϑ can be given as

$$\vartheta = \frac{4\pi\acute{\eta}}{ln(2h/r)}$$

where $\acute{\eta}$ represents the viscosity, $\acute{\eta} = 0.89 \times 10^{-3}$ $\mathrm{kgm}^{-1}\mathrm{s}^{-1}$ at $25°C$. Here h and r are the height above the surface and the hydrodynamics radius of the filament, respectively. For actin filaments with $r \sim 4.5$ nm and $L = 22.7$ μm, the relaxation time for the first mode is $\tau_1 = 15$ s and for the second mode is $\tau_2 = 2.0s$. In the case of microtubule filaments with $r \sim 15$ nm and $L = 63.2$ μm, $\tau_1 = 3.9$ s (26).

These physical parameters are not connected directly to the models in this thesis since this thesis dealt with the mechanical properties of the cells rather than the

mechanical properties of the cytoskeletal elements. However, cytoskeletal elements play a fundamental role in the mechanical properties of the cells, therefore it is interest to understand their behaviour.

1.1.4 Epithelial tissue

In the epithelial tissue, the cells are aligned to constitute a sheet-like structure which is, in turn, arranged either in a monolayer, as in the lining of the gut and the developing embryo, or in a multilayer, as in the outermost layer of the skin, which is termed epidermis (32). The simple epithelium is that tissue with a monolayer sheet, while the stratified epithelium is the tissue with a multilayer sheet. Additionally, the epithelial sheets carry out a different number of functions in the multicellular organisms. In the skin, the epidermis sheets work as protector; in the gut, the monolayer sheet absorbs the nutrients while other sheets secrete many important products such as hormones, tears and milk. Some others respond to the light signals, as in the eye retina or to the sound signals as in the ear hair cells. Epithelia also play a significant role not only in the protection of the organisms from diseases by preventing the microorganisms from entering the body but also in maintaining the fluid inside the body. However, despite the different functions of the epithelial tissues, they clearly share many common structural features (5; 6).

An epithelial cell has three surfaces, namely apical, lateral, and basal, which refer to the upper, sides and lower domain of the cell, respectively. While the basal and lateral surfaces are together referred to as the basolateral surface, the apical and basal are jointly known as the apicobasal surface. Finally, the apical and lateral surfaces are collectively termed the apicolateral surface (80).

For creating an epithelial sheet, the cells link to one another through cell junctions (23) where the tight junctions, anchoring junctions and gap junctions are the three principal classes of the cell junctions that have been clearly observed in the epithelial tissues (Figure1.3). The function of these junctions is to link tightly epithelial cells to each other for constituting epithelial sheets. The tight and the anchoring junctions provide the strength and rigidity to these sheets. Moreover, these junctions play a central role in the communication between these cells (57). In addition, the tight junctions serve as selective gateways that constitute

barriers to separate the apical and basolateral surfaces for regulating the paracellular diffusion of ions, solutes, and other materials, and for preventing the exchange of the membrane elements between these two domains. The tight junctions also play a significant role in the process of signal transduction that guides the behaviour of the cells (reviewed in detail in (65; 85; 93)).

Anchoring junctions in the epithelial tissues fall into three main subcategories: adherens junctions, desmosomes and hemidesmosomes (Figure 1.3). For the adherens junctions and also desmosomes, the cadherins calcium-dependent cell-cell adhesion molecules, link two adjacent cells together; while for hemidesmosomes, the integrins, which are a large family of $\alpha\beta$ heterodimeric transmembrane receptors (43), bind the basal surface of the cells to the basal lamina underneath the cells. The tight and the adherens junctions attach to the actin filaments, while both the desmosomes and the hemidesmosomes interconnect to the keratin intermediate filaments as illustrated in the Figure 1.3 (33; 57).

The gap junctions are constituted of connexins forming transmembrane channels. These channels, that connect the cytoplasm of two neighbouring cells, permit small molecules to be transmitted between two connected cells (7; 14; 29; 82).

Furthermore, cell to cell adhesion is necessary to build coherent epithelial sheets which differ in apical and basolateral polarity (70).

Cell polarity refers to asymmetry in one or more of the characteristics of the cell, as in the epithelial cell, such as in the shape, structure, functions, and in the distributions of proteins. The tripartite junctions: tight junction, adherens junction and the desmosome located in the apical surface, constitute the section known as the apical-junction complex (33).

In the plane, the cells in the epithelial sheets roughly take a polygonal cross section with a different number of sides, as shown in Figure 1.4. Cell shape refers to the cell's number of neighbours (CNN).

1.1.5 Cell division

Cell division plays a central role in the development of multicellular organisms. There are two kinds of reproduction of cells: sexual reproduction and asexual reproduction. The cells, tissues and organs in any multicellular organism come

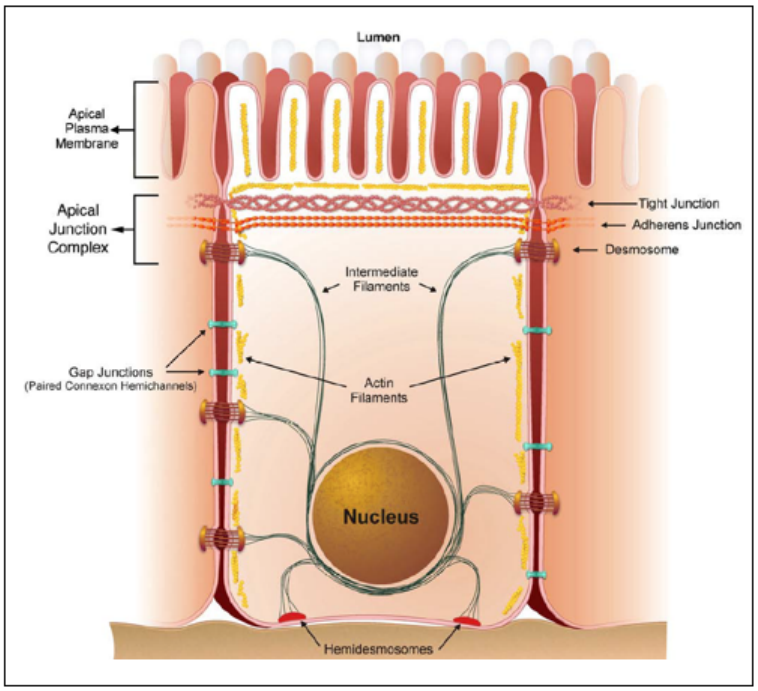

Figure 1.3: Different classes of polarized epithelial cell junctions and their interactions with the elements of two connected cells. The tight and adherens junctions in addition to the desmosomes, that are at the apical part of lateral cell membranes, comprise the apical junction complex. The remainder desmosomes, in addition to gap junction, are found at lateral cell membranes under the apical junction complex. Hemidesmosomes are situated in the basal cell membranes and are linked with the basal lamina. The tight and adherens junctions connect to the actin filaments, while both the desmosomes and the hemidesmosomes connect to the intermediate filaments. The figure is taken from (33).

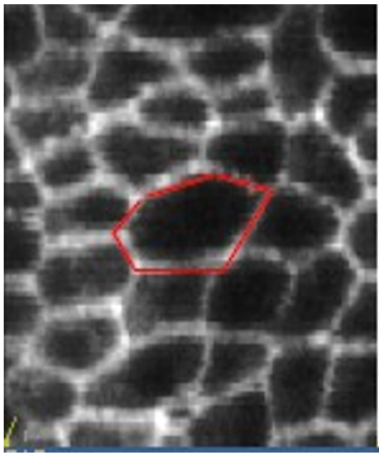

Figure 1.4: View of the apical side of epithelial tissue in vitro (image taken from the chick embryo gastrula): white lines represent borders between cells (courtesy of Professor Kees Weijer, FRSE University of Dundee). Cell borders labelled by a fluorescent marker. For identification purposes, walls of one of the cells are additionally coloured in red, this shows the polygonal shape of the cell.

from one cell obtained in the process of sexual reproduction (5).

A fertilized egg is the first step in the process of the evolution of an organism. It is followed by the second step in which a significant number of cells are produced by cell division, leading to the development of tissues, the differentiation of cells, and finally the organ formation. This thesis focuses on cell division when two genetically identical daughter cells are produced from a typical tissue cell (57).

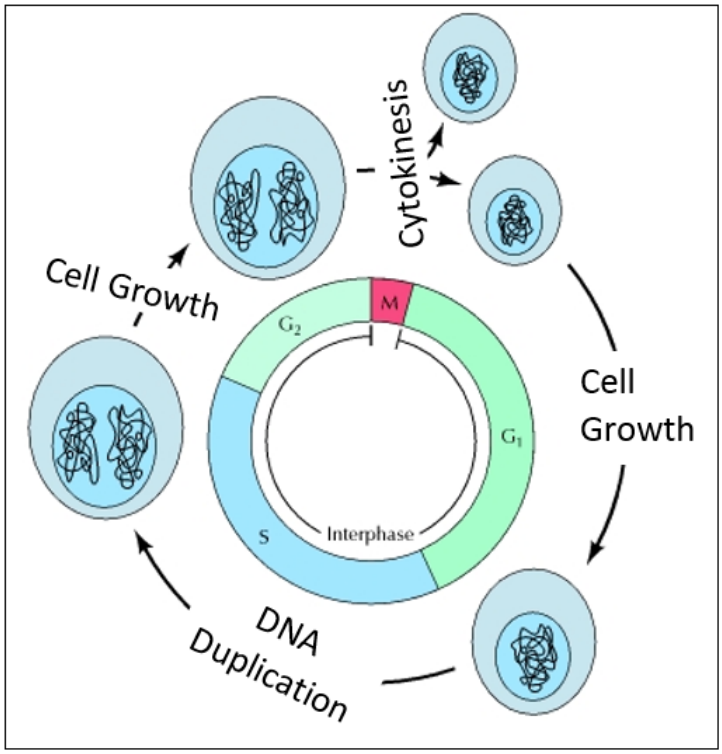

Figure 1.5: Illustration of the phases that the eukaryotic cell undergoing during its cell cycle. The figure is taken from (16).

The cell cycle is the process in which a cell passes through a successive series of events resulting in the duplication of its components and then divides into two. The underlying mechanisms that guide the cell cycle are similar for all eukaryotic cells (6). The eukaryotic cell cycle is comprised of four consecutive phases: gap G1, synthesis S, gap G2 and M. In G1 and G2, the cell grows; DNA is replicated in phase S. Phase M consists of two steps which are the mitosis that guides the division of the nucleus and the cytokinesis that completes the division of the cell into two, as depicted in the Figure 1.5, (6; 34). Moreover, the shape of the cells bears an important role in determining the orientation of the divisional plane.

The experimental observations of the cell-edge distribution have been performed on *Drosophila melanogaster*. The *Drosophila melanogaster*, a fruit fly, is used

as model organism for many studies, including genetic analysis, since the early part of the 20th century as the sample can be easily conserved, and also needs a relatively short time, roughly two weeks, to reproduce, thus rendering it a convenient experimental model (16).

1.2 Mathematical studies of cellular dynamics

Experimental observations are important in determining the components of cells, understanding the functions of these components and examining the relationship between components and their external environment, and also among themselves. However, the massive amount of experimental data on one hand and the complexity of many cellular activities on the other make the use of mathematical models unavoidable. Mathematics provides efficient tools to analyse and comprehend the data, saving the time of experimentalists. There are three main models that have been used to describe the dynamics of tissue development, namely the vertex dynamics model, the Potts model, and a set of so-called cell-centre models (21).

For studies of tissue topology represented by cell-edge distribution, some models, such as the model that has presented by Gibson et al. (25) and the models that have presented by Sandersius et al. (79), hereafter referred to as GPNP model and SCWN models respectively, have been introduced. Later in the chapter, these two models are described in detail.

Mathematical models not only are beneficial to validate the experimental observations but can also be used to simulate processes that cannot be easily implemented in vitro. For example, representing the epithelial cells as polygons enables the researchers to study many features of epithelial tissues, such as the impact of cell movements and cell divisions in a tissue, and to understand the topology and underlying mechanisms that regulate the dynamics of these tissues (22).

In this study, the vertex model is used to examine whether the stretching/shrinking of cells under certain values of parameters of applying forces is exponential. This model is also used to determine the number of cell-edge distribution associated with cell divisions and cellular mixing.

1.2.1 The Potts models

The cellular Potts model is a computational 2D lattice-based model, which was first used by Graner and Glazier to study the development of biological epithelial tissue (31; 27). This model is also called the Glazier-Graner (GGM) model. In this model, the tissue consists of a collection of lattice cells (Figure 1.6). Each cell (associated with the cell index) is considered as a set of grid points on a regular lattice. Movement of a cell indicates that the cell loses or acquires some lattice points. This implies that the grid points may belong to different cells with time. To model the evolution of the tissue, a variation principle approach is applied to minimize the energy of the system neighbour point is randomly chosen to be associated with a considered grid point, followed by determining the change of system energy in the case of the states of the point and its neighbour changing with each other. The change between the state of the grid point and its neighbour is allowed if the change of energy is decreases. On the other hand, the probability of the change is calculated in the case of the change increasing. For the probability, p, Boltzmann factor: $p = e^{-\Delta E/T}$ is used, where T is a parameter representing the temperature of the system. Furthermore, the energy can be determined using the adhesive forces between cells and the pressure force which is associated with the incompressibility of cells:

$$E = E_{adhesive} + E_{pressure} \tag{1.3}$$

1. The cell-to-cell contacts have adhesive energy $J_{k,l}$ ($J_{k,l} = J_{l,k}$), where $J_{k,l}$ represents an interface between adjacent grid points, provided that these points belong to different cells (k and l are the types of these cells).

2. In order to control the volume of a cell (say cell k), $V_k(t)$, a target volume T_k is used. The volume of a cell refers to the number of its grid points. This k cell is given a volume effective energy

$$E_{vol,k} = \alpha(A_k(t) - T_k)^2$$

where α is a positive constant (63).

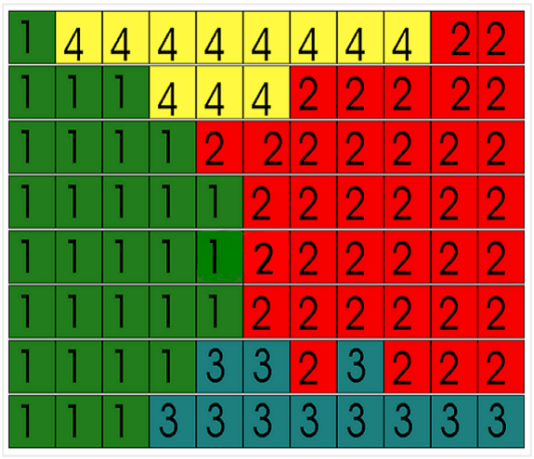

Figure 1.6: Schematic illustration of the Potts model. Squares with the same colour represent one cell

1.2.2 The cell-centre model

The cell-centre model is an off-lattice model which is based on the Voronoi diagram formed from the centre of the cells. This approach originally was developed by Meineke and his co-workers (62) and fully described by van Leeuwen et al. (86). In 2010, the cell-centre model was extended by Osborne et al. (74). In this model, each cell is considered as a discrete object and neighbouring cell centres are linked by linear springs. A Delaunay triangulation and A Voronoi tessellation are used to determine the adjacent cells and the cell shapes, respectively, as depicted in Figure 1.7. The equation of motion, neglecting inertial effects, is given as

$$\eta_i \frac{d\boldsymbol{r}_i}{dt} = \sum_{j \in S_i} k_{ij}(|\boldsymbol{r}_i - \boldsymbol{r}_j| - S_{ij}(t)) \frac{\boldsymbol{r}_j - \boldsymbol{r}_i}{|\boldsymbol{r}_j - \boldsymbol{r}_i|}, \qquad i = 1, ..., N. \tag{1.4}$$

Where $\boldsymbol{r}_i$ is the position of the centroid of cell i, η_i denotes its associated drag coefficient, N is the total number of cells, k_{ij} and $s_{ij}(t)$ are the strength and natural length, respectively, of the spring connecting centres of $i{-}th$ and $j{-}th$ cells. S_i is the collection of all neighbouring cells to cell i and t is time (74).

1.2.3 The vertex dynamics model

Dynamic behaviour of epithelial tissue plays an essential role in a large number of developmental processes, such as growth, disease development and wound closure. Moreover, computational dynamical models are important in studies of cell-cell

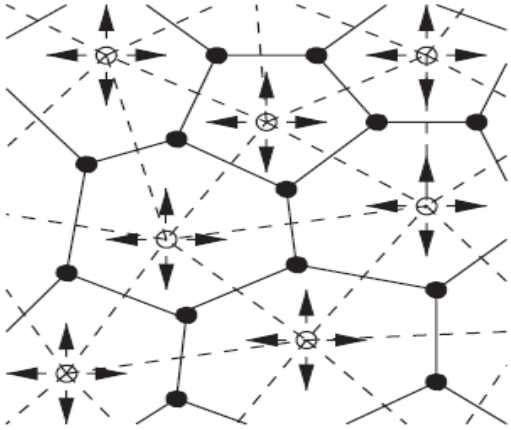

Figure 1.7: Schematic representation of the cell-centre model. The cells are specified from a Voronoi tessellation of the centre of cells. The figure is taken from (74).

interactions (22).

As mentioned previously in this chapter, there are three main approaches that can be used to simulate the development of the epithelial tissue. This study is focused on the use of the vertex dynamics model to study dynamical processes in epithelial tissues as governed by cellular forces which are represented as forces acting upon cellular vertices (20; 44; 68).

In the vertex dynamics model, each cell can be approximated geometrically by a polygon in two-dimensions and a polyhedron in three-dimensions, which is approximately compatible with the experimental observations of the epithelial tissues. In this model, the rules are established to determine how each vertex moves, how the cell divides, and how the cell follows rearrangement (22). Originally, the vertex model was used to investigate the topology of inorganic systems such as grain boundaries (49), soap froth (60) and foams (73) because in all of these structures pressure and surface tension generate dynamics. The vertex model has also been presented to describe whether the different cell division patterns in the pitcher leaves of *Sarracenia purpurea* are adequate to illustrate bifacial growth in the hollow region and protruding growth in the ridge (24). The first appearance of the vertex dynamics model for studying the epithelial monolayer deformations was in 1980 in a publication by Honda and Eguchi (37). In 2004, Brodland (10) presented a thorough review of the vertex dynamics model for biological systems and its comparison to the two other models.

Furthermore, in the three-dimensional vertex model, each cell can be

approximated geometrically by a polyhedral, which has been used to study the dynamic behaviour of developing tissues by many researchers (18; 41; 81). The process of cell intercalation which leads to a formation of an elongated tissue in a cell-monolayer has also been investigated by using the three-dimensional vertex model (39). The vertex dynamics model has also been used to study the processes of wound closure in epithelial tissue (40; 68; 69).

In 2015 Honda and Nagai (38) reviewed the history of both cell models, the cell-centre model and the vertex dynamics model, and explained their applications in detail. They also highlighted that these models are indispensable to the understanding of the technique whereby genes direct biological shapes.

The open source Chaste framework uses a test-driven approach which is a C++ code. It has been widely used in recent studies to simulate the vertex dynamics model owing to its versatility and generality (21; 64; 76).

The vertex dynamics model and cell-centre model are usually deterministic and off-lattice models, while Potts models are lattice-based models and stochastic. The factors which make the vertex model more convenient to study the epithelial monolayer deformations than the other models is (1) the way in which the cells are represented (polygons) which is in agreement with the experimental observations; (2) its ability to incorporate cell rearrangement within an epithelial monolayer in an explicit way; (3) the results that can be obtained via the vertex model simulations can be interpreted biologically more easily than from the simulations obtained by using the other models (22).

1.2.4 The GPNP model

Divisions and rearrangements of cells control the development of tissues. The epithelial cells show diverse polygonal shapes and that feature requires a quantitative method of description. The distribution of the cell edges have been studied mathematically and experimentally for a long time. The first attempt to understand the pattern of the number of cell-edges dates back to the early twentieth century when Lewis studied the geometrical characteristic of the epidermis of cucumber, theoretically and in vitro, and his studies become a basis for later research (54; 55;

56).

Recently, Gibson and his co-workers (25) have introduced a mathematical model, referred to as GPNP model, to understand the cell-edge distribution and to present the universal pattern for this distribution through studying many different species and building histograms for the corresponding distributions of the number of cell edges. Building the histogram for the CNN (cell's numbers of neighbours) is the most effective way to characterize the tissue topology.

The GPNP model is a well known useful model, largely because of its simple assumptions: all cells divide in a synchronous way; the mother cell's nodes are distributed randomly using the binomial distribution between two daughter cells and the absence of cells with less than four edges, which is in agreement with the biological observations, as a small number of cells with this number of edges have been observed experimentally. Also, its behaviour shows a good agreement with the biological data. However, there are some shortcomings in this model which are related to the fact that some model assumptions are not realistic. It is assumed in the GPNP model that all cells divide synchronously but this is not consistent with biological observations (79). Also, although the results of this model are in a good agreement with the biological data, the entire absence of cells that have four edges was observed in the outcomes of the model, which is in contrast to observation of $3\% - 4\%$ of these four-edged cells in vitro (79). Finally, the manner of distributing nodes between daughter cells is not unique; there are multiple algorithms that can be applied (79), as will be seen later in this chapter.

To describe the GPNP model (25; 79), the starting point is the building of two transition matrices, one of which describes the replacement of the mother cell by daughter cells and the other, the effect of cell division on neighbouring cells. Let N represent the number of cells, and T and S are the two transitions matrices. The entries of the matrix T, T_{ij}, refer to the probability of getting a j-sided daughter cell as a result of dividing an i-sided cell. For this, the division of an i-sided mother gives two of its vertices to each of its newly created daughter cells, leaving $i - 4$ edges to be separated randomly, with equal probability, between the two daughter cells according to the binomial distribution.

Additionally, two new nodes are added to each daughter as a result of

constructing a new cell. Hence

$$T_{ij} = \binom{i-4}{j-4} \frac{1}{2^{i-4}}, \qquad 4 \leq j \leq i \tag{1.5}$$

The entry of S, S_{ij}, refer to the probability of obtaining a j-sided cell as a result of an i-sided cell acquiring an extra edge. This transition matrix accounts for the impact of the divided cell on its neighbouring cells. Now, since synchronous division, which is one of the assumptions of this model, forces all cells to divide at each generation, and since there are N of the cells, each of them will acquire an additional edge in the new generation. Thus, the new generation possesses $2N$ cells with $2N$ extra edges. Hence on average, each cell will acquire one edge and according to

$$S_{ij} = \begin{cases} 1 & \text{if } j = i+1 \\ 0 & otherwise. \end{cases} \tag{1.6}$$

By taking $U = TS$, we have

$$U_{ij} = \binom{i-4}{j-5} \frac{1}{2^{i-4}}, \qquad 5 \leq j \leq i+1, \qquad i \geq 4. \tag{1.7}$$

The other values of U are zero. Therefore the distribution of fractions $P = (P_4, P_5, P_6, P_7, P_8, P_9)^T$ of different sided-cells, where $P_i = \frac{N_i}{N}$, $i = 4, ..., 9$ at the generation r can be described as

$$P^{r+1} = U^T P^r = (U^T)^{r+1} P^{(0)},$$

where U^T is the transpose of U and $P^{(0)}$ is an arbitrary column-vector initial condition (for example, $P^{(0)} = (0, 0, 1, 0, 0, 0)^T$, that means the process starts with a 6-sided cell). Since the cells of less than four and more than nine edges are rare in biological data, they are often not taken into account. The histogram of normalization of the results that has been obtained from repeating the processes for many of generations (say 10000) can be given, this was done using Matlab (17a) code which is provided in Appendix A.1, in comparison with the experimental observations as shown in Figure 1.8. The GPNP model exhibits a very good agreement with the experimental data. However, there is one exception related

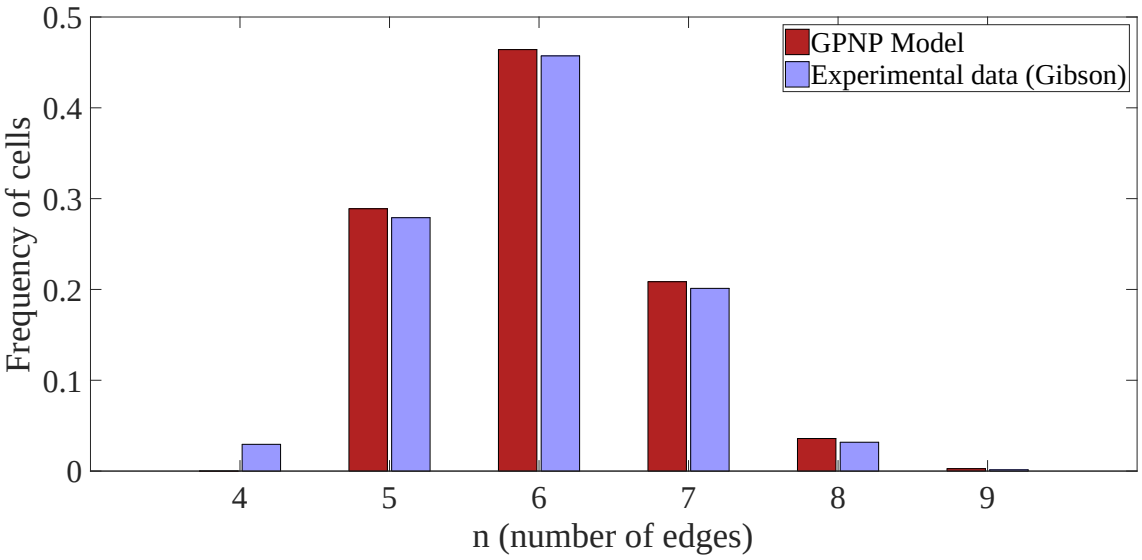

Figure 1.8: Distribution of cells according to the number of edges in experiments (melrose bars) and in GPNP model (FireBrick bars). The figure is produced by the author using data from (25).

to the absence of 4-sided cells, in contrast to the presence of approximately 4% of this kind of cells in the empirical observations. The following models, SCWN models, represents an attempt to improve the GPNP model.

1.2.5 The SCWN models

To tackle the absence of the 4-sided cells as well as the algorithm of the random distributing of edges between the two daughter cells, the three different SCWN models have been constructed by Sandersius and his co-workers (79) via changes in some assumptions of the GPNP model.

Firstly, the SCWN model that allows three-sided cells is considered. Although the 4-sided cells are allowed in the GPNP model, the way in which the distribution of cell edges is calculated compels the absence of this type of cells. This happens because the 3-sided cells are not accepted by a calculating algorithm in the GPNP model, and also because the GPNP model is synchronous, which means that all cells will gain an extra edge in the next generation. For that, in the first model, the GPNP is reformulated to allow the 3-sided cells, which, in turn, enable the 4-sided cells to be constructed, whereas in the transition stage, the 3-sided cells gain an extra edge and form 4-sided cells. Thus the two transition matrices T and U are

reconstructed to undergo this new assumption and are given as

$$T_{ij} = \binom{i-2}{j-3} \frac{1}{2^{i-2}}, \qquad 3 \leq j \leq i+1, \tag{1.8}$$

$$U_{ij} = \binom{i-2}{j-4} \frac{1}{2^{i-2}}, \; 4 \leq j \leq i+2, \qquad i \geq 3. \tag{1.9}$$

In contrast to the GPNP model, this model gives one of the mother cell's edges to each of the daughter cells which each gain another edge as a result of creating the new interface. Also, the other mother edges are distributed with the same probability between the two daughter cells. Consequently, although the 4-sided cells are seen clearly in the histograms for this model's outcomes, the results are not compatible with the experimental observations, for the frequency of 4-sided cells is now approximately 8% in contrast to 4% in the experimental data shown in Figure (1.9).

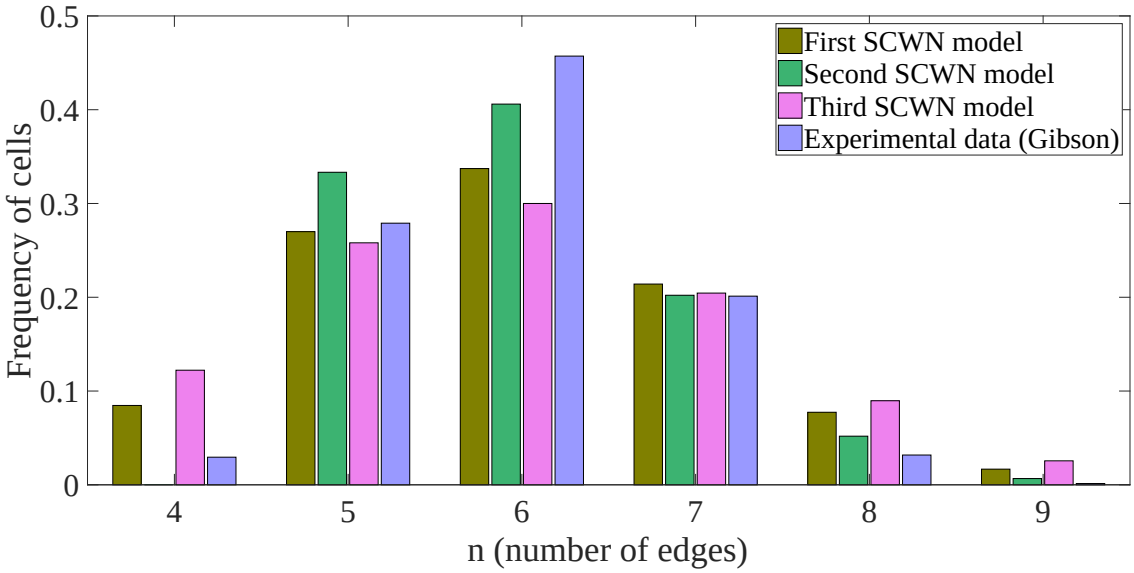

Figure 1.9: Comparison of histograms obtained using the three modifications of SCWN model with experimental data. The first SCWN model (olive histogram), the second SCWN model (green histogram), the third SCWN model (violet histogram) and the experimental data of the *Drosophila* disc epithelium (melrose histograms). The figure is produced by the author using data from (25) and (79) to build a Matlab (17a) codes. The Matlab codes are presented in Appendices A.1 and A.2.

Furthermore, the conditional probabilities in distributing the edges of a mother cell between its two daughter cells in GPNP undergo a subtle bias because the distribution is not unique. To avoid this bias state, the second and the third models

operate on the hypothesis of splitting the nodes randomly, either in uniform or in binomial fashion, between the two daughter cells, then rejecting 4-sided cells in the second SCWN model and rejecting 3-sided cells in the third SCWN model. Hence, the transitions matrices T and U in the second and third SCWN models can be reformulated from the GPNP as

$$T_{ij} = \binom{i}{j-2} \frac{1}{2^i - 2 - 2i}, \qquad 4 \leq j \leq i, \tag{1.10}$$

$$U_{ij} = \binom{i}{j-3} \frac{1}{2^i - 2 - 2i}, \; 5 \leq j \leq i+1, \qquad i \geq 4, \tag{1.11}$$

for the second SCWN model and

$$T_{ij} = \binom{i}{j-2} \frac{1}{2^i - 2}, \qquad 3 \leq j \leq i+1 \tag{1.12}$$

$$U_{ij} = \binom{i}{j-3} \frac{1}{2^i - 2}, \; 4 \leq j \leq i+2, \qquad i \geq 3 \tag{1.13}$$

for the third SCWN model. Similarly, as in the GPNP approach, the distribution of fractions $P = (P_4, P_5, P_6, P_7, P_8, P_9)^T$ of different sided-cells; $P_i = \frac{N_i}{N}, \; i = 4, ..., 9$; at the generation r can be expressed as

$$P^{r+1} = U^T P^r = (U^T)^{r+1} P^{(0)},$$

where U^T refers to the transpose of U and $P^{(0)}$ refers to an arbitrarily chosen column-vector initial condition (for example, $P^{(0)} = (0, 0, 1, 0, 0, 0)^T$) . As evident from Figure 1.9, the histograms obtained using the second and the third SCWN models also failed to be compatible with the biological data.

1.3 Some important previous models and rules

Some of the considerable contributions that have been converted into laws and models and have impacted on studies and the understanding of cell distribution regarding the number of edges are presented briefly in this section.

1.3.1 Lewis' experiments

Cell division has a crucial impact on the dynamics of tissues. While experimental studies of cell division have advanced tremendously during last two centuries, the computational investigation of this phenomena has received attention only recently. The earliest theoretical investigations on cell division topology were undertaken by Lewis (54; 55; 56). He examined the topological effects of cellular division, focusing on the hexagonal cell shape and area. The investigation began with dividing regular hexagonal cells with edges of unit length and studying the expected cell shapes and areas as well as their effects on the other tissue cells, mathematically and experimentally. In (55), the relationship between the cell division and both the shapes and areas of the cucumber's epidermal epithelial tissue cells were presented by Lewis. He described cells of various polygonal shapes and also analysed frequencies of cells with a different number of edges forming during the process of division, as described in Table (1.1). The data on the cell-edge distribution that are presented

i	M_i	L_i	$m_i = \frac{M_i}{1000}$	$l_i = \frac{L_i}{1000}$	$R_i = \frac{l_i}{m_i}$	$\sigma_i = \frac{R_i}{\sum_{i=4}^{9} R_i}$
4	20	0	0.02	0	0	0
5	251	16	0.251	0.016	0.0637	0.0018
6	474	255	0.474	0.255	0.538	0.0149
7	224	478	0.224	0.478	2.1339	0.0589
8	30	224	0.03	0.224	7.4667	0.2062
9	1	26	0.001	0.026	26	0.7182
10	0	1				
Total	1000	1000				

Table 1.1: Data on the frequencies of cells representing polygons with different number of edges and their involvement in cellular division. M_i represents the number of cells with i-sides and L_i represents number of dividing cells with i-sides. The first two columns of the table is taken from (55).

in the fourth column of Table (1.1) is presented as a histogram in Figure 1.8. The seventh column of the table shows the relationship between the number of the edges in a cell and the ability of this cell to divide. It is suggested that the more edges a cell has, the more opportunity it has to divide. This relationship can be approximated by an exponential function, as will be demonstrated later in Chapter 3.

1.3.2 Aboav-Weaire's Law

In 1970 Aboav investigated the way in which grains of the polycrystalline magnesium oxide are arranged (2). In his study, he used a specimen of 3000 grains with diameter average $12\mu m$, He found that the relation between the number of sides, i, of a grain and the average value, m_i, of the sides of adjacent grains is approximately

$$m_i = 5 + \frac{8}{i}. \tag{1.14}$$

Later, in 1974, Weaire (88) introduced the parameter μ_2 which can be expressed as

$$\mu_j = \sum_i (i-6)^j p_i \Rightarrow \mu_2 = \sum_i (i-6)^2 p_i, \tag{1.15}$$

where p_i represents the fraction of grains of i sides, $\mu_2 = 0$ if all the grains are hexagonal and $\mu_2 > 0$ otherwise. Moreover, he also found that

$$\sum_i m_i i p_i = \mu_2 + 36. \tag{1.16}$$

Since the Equation (1.14) is for specific case, m_i is generally expressed in (3) as

$$m_i = \left(6 - a + \frac{b\mu_2}{6}\right) + \frac{6a + (1-b)\mu_2}{i}. \tag{1.17}$$

where a and b are constants. The Equation (1.17) reduced, taking $a = 1$ and $b = 0$, by Weaire using (1.15) to present the following equation

$$m_i = 5 + \frac{6 + \mu_2}{i}. \tag{1.18}$$

However, by taking $a = 1.2$ and $b = 0$, suggested by the empirical studies, the Equation (1.17) is given as

$$m_i = (4.8) + \frac{7.2 + \mu_2}{i}, \tag{1.19}$$

where m_i represents the average number of edges surrounding a i-sided cell. Subsequently, more attention was paid to the law of Aboav-Weaire to formulate equivalent laws and to find accurate values of the parameters. These laws have been

used widely in the physical and biological applications (87; 94).

The Equation 1.19 was confirmed in simulation of the epithelial tissue using vertex dynamics model as shown in Chapter 3.

1.3.3 Kolmogorov's Concept

Kolmogorov (50) modelled the dynamics of distribution of particles according to their sizes in the course of particle fragmentation (industrial stone crushing involved in iron mining). For this, he denoted the whole number of particles and its expectations by $N(t)$ and $\bar{N}(t)$, respectively, and the number of particles of size $\nu \leq r$ (r is a specific size of particles.) and its expectation by $N(r,t)$ and $\bar{N}(r,t)$, respectively (30). He also termed $G(\xi)$ to refer to the mathematical expectation of the number of breaking particles of size $\nu \leq \xi r$, $\xi \in [0,1]$, that were constructed in the time interval $[t, t+1]$ from a mother particle of size r. This approach, based on fundamental assumptions that is the probability of fragmentation of each particle is independent of its size, and of the size of the fragmentation of any other mother particle, and of the initial time $t = 0$ (i.e. it is independent of any prior conditions to fragmentation of that particle). According to these assumptions, Kolmogorov found that

$$\bar{N}(r, t+1) = \int_0^1 \bar{N}\left(\frac{r}{\xi}, t\right) dG(\xi), \tag{1.20}$$

and by taking $x = \ln r$, the cumulative distribution $T(x)$ can be described as

$$T(x,t) = \frac{\bar{N}(e^x, t)}{\bar{N}(t)} = \frac{N(e^x, t)}{N(t)}. \tag{1.21}$$

Now, let $\chi = ln\xi$ and $G(\xi) = G(1)S(\chi)$ where $S(\chi)$ is mathematical expectation for particle of size ξ or less to be broken, therefore the Equation (1.20) can be reformulated as

$$T(x, t+1) = \int_{-\infty}^{0} T(x-\chi, t) dS(\chi), \tag{1.22}$$

Using Lyapunov's Theorem, Kolmogorov concluded that $T(x,t)$ in course of time tends to a Normal distribution and therefore $N(r,t)$ - to a log-normal distribution (30). i.e.

$$T(x,t) \to \frac{1}{\sqrt{2\pi t}B} \int_{-\infty}^{x} e^{-\frac{(\chi - At)^2}{2B^2 t}} d\chi, \tag{1.23}$$

where

$$A = \int_{-\infty}^{0} x dS(x), \qquad B^2 = \int_{-\infty}^{0} (x - A)^2 dS(x).$$

The cell-edge distribution of cell division is fitted as a Log-normal distribution as can be seen in chapter three.

1.4 The vertex dynamics model with Chaste

As mentioned previously in this chapter, the vertex dynamics model has been used efficiently to study numerous essential cellular processes, such as the development of tissues, cell divisions, cell rearrangements, wound healing, and cancer invasions (74). An evolution of the epithelial cell in this model is considered as a result of the motion of its vertices that are subjected to mechanical forces. The velocity of a vertex i can be presented as

$$\eta_i \frac{d\boldsymbol{r}_i}{dt} = \boldsymbol{F}_i, \tag{1.24}$$

where $\boldsymbol{r}_i$ represents the position of the vertex i, $\boldsymbol{F}_i$ represents the sum of all forces acting upon the vertex at time t (35), η_i represents its mobility coefficient. $\boldsymbol{F}_i$ are usually considered to be potential and defined by potential functions (see (20; 37)).

In (37) the researchers attemted to reproduce the honeycomb arrays, which represent the apical side of an epithelial sheet, using computational simulations through the vertex dynamics model. To build a successful model for studying the development of cells, using either the vertex dynamics model or any other model that necessitates the elements associated with the cells, necessarily precludes the intersection, and to fulfil this condition, the topological rearrangements need to be taken into account.

The first and the most distinguished cell rearrangement is the T1-transition, Figure 1.10, which switches the neighbouring cell relationships (89). Each T1 swap, edge rearrangement, results from removing an edge and, in turn, the two non-adjacent cells that contain the end vertices of the removed edge, form a new shared edge. The T1 swap can happen when the length of the removed edge becomes less than a specific threshold distance value. If the removed edge is on the periphery of the tissue and belongs to one cell, then the vertices on its two ends merge. Additionally, the element with four edges, associated with a cell in a simulation, can

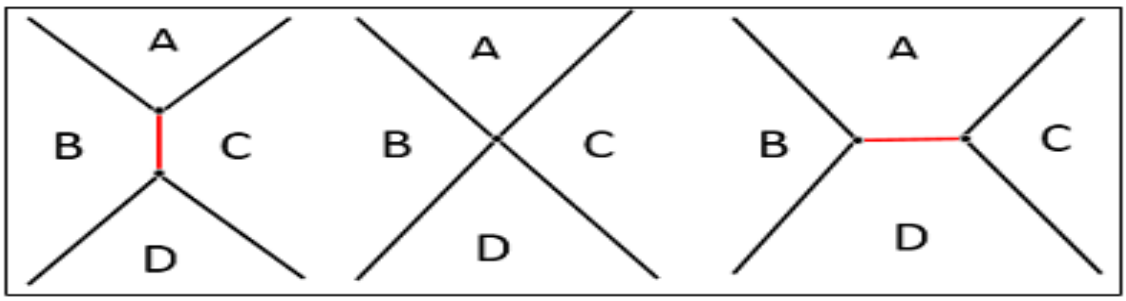

Figure 1.10: Junction rearrangement during T1-transition: the edge between the cells B and C disappears while the new edge between the cells A and D forms.

be converted to a 3-sided element through the T1-transition processes. Moreover, the triangular element, that has three edges, remains in the mesh if its area is bigger than or equal to a threshold area value; otherwise when the target area is small it will be removed from the mesh and its associated cell will be removed from the simulation via a T2-transition. Therefore, T2-transition is the processes of removing the triangular elements and the voids that occur in the mesh. The third topological rearrangement is the T3-transition, or element intersections, that represents the process of merging a vertex of an element in the mesh with an edge belonging to another element. This process has multiple roles in the development of cells, such as wound healing (21; 22; 68). However, this is outside the scope of this thesis.

There are some features that distinguish cells from other materials, such as foams, that have been studied through the vertex dynamics model. Cells can grow, divide and be destroyed. These features have a significant role in the morphogenesis of multicellular organisms, where a cell that is subjected to mitosis divides into two daughter cells of the same size (11). The two new daughter cells are formed by placing two new vertices on the perimeter of a mother cell, which are the ends of the cleavage line that crosses the cell's centroid and incorporates the boundary of the divided cell.

To simulate the evolution of the epithelial sheet using the vertex dynamics model (21), the steps of implementation are to start with the initial position for each vertex in the mesh, $\boldsymbol{r}_i^0$, the time undergoing discretization, such that $t^c = c\Delta t$, where Δt refer to the time step and c refers to the current iteration. The position and the applied net force can be taken as $\boldsymbol{r}_i^c = \boldsymbol{r}_i(t^c)$ and $\boldsymbol{F}_i^c = \boldsymbol{F}_i(t^c)$, respectively. As

long as the simulations are running, some procedures must be executed at each time step. Where the inner progress that occurs in each cell, such as the cell cycle, the cellular processes including the topological rearrangements, such as T1-transition, cell division and cell death, all have to be amended. Finally, one of the numerical methods for solving the differential equations, such as Runge-Kutta or Forward Euler discretization, must be employed to solve the Equation (1.24) for determining new positions of vertices and cells separately and simultaneously. According to the Forward Euler discretization, we have the following equations

$$\boldsymbol{r}_i(t + \Delta t) = \boldsymbol{r}_i(t) + \frac{\Delta t}{\eta_i}\boldsymbol{F}_i, \tag{1.25}$$

where Δt necessarily is chosen as a small value for the stability of the solution. It is evident that imposing cells in epithelial sheets onto a series of edge rearrangements form plastic deformations and may cause local dynamic rearrangements. Hence, some cells show fluid-like behaviour through the intercalation process owing to the edge rearrangement, T1-transition, generating a local contraction and expansion in the direction of the removed edge and the newly created edge respectively.

Moreover, the stochastic process may be applied when dealing with the cell cycle, where the duration of the first phase, G1, is chosen to be a random variable.

1.4.1 The Chaste implementation of the vertex dynamics model

In this thesis, simulations of the vertex dynamics model were implemented using the open-access software Chaste, which takes the object-oriented language C++ (84) as the essential programme for writing its code (64; 76). However, a few new subroutines were developed and added to make it more appropriate for this research (Appendix B).

The Chaste software (21; 64; 76) is built to study and to simulate many complex problems using different mathematical concepts in addition to solving ordinary and partial differential equations. Relating to the biological cells, this framework can deal efficiently with various essential mathematical models such as Potts model, various cell-centred models and the model of interest in this study, which is the vertex

dynamics model, in order to model the most important cellular processes, including cell division, cell rearrangements and adhesion as well as the dynamical behaviour, such as the topological change, diffusion, and shear. The fundamental steps of simulating cellular processes such as cell divisions and topological rearrangements through the software Chaste can be briefly described as follows:

1. The generation of a required number of cells.
2. The use of an appropriate way for connecting the elements in the mesh and its represented simulated cells with each other.
3. The determination of the start time, end time, and the time step of the simulation and loop over each vertex of each element in the mesh to add the magnitude of the net applied force.
4. The addition of the requested functions (forces), where each is relatively a short-code that performs a special task and uses the test class.
5. In the case when cell division is induced, defining the way the division takes place, i.e. whether it is deterministic or stochastic, needs to be determined and the appropriate coding file used, to assign a particular division time for each cell. In this study, and because the vertex dynamics model has been used, the mesh must comprise as many elements as the number of cells, where each cell in the simulation is represented by an element in the mesh.
6. Finally, the running of the simulation.

More details that explain how to deal with the open software Chaste are given in Appendix B.

1.5 Aim of this these

In this thesis, the vertex dynamics model was used for studying the mechanical properties and topology of epithelial tissues. The relaxation of the epithelial cell that subjected to a short-time deformation was studied numerically and mathematically to indicate whether it is elastic or plastic. This thesis also tries to present the

novel mathematical model, using master equations and simulations, for the cell-edge distribution in the case of the cell divisions and cell rearrangement that is represented by T1-transition.

1.6 Remainder of thesis overview

The overview of the remainder of the thesis is given as follows:

Chapter 2 examines the behaviour of a tissue when it is stretched/shrunk and released to indicate whether it is elastic or plastic under certain parameters values. For that, the vertex dynamics model is used that implemented, for simulations, by the open software Chaste. In the case of the tissue being elastic , the relaxation time was found. The relaxation time is the time that needed for the cell to get e-times closer to equilibrium. The examination started with a single cell that is stretched and shrunk vertically 5%, 10% and 15% and the results of all these cases show the elastic behaviour of the stretching/shrinking and the relaxation time are halved in the case of applying the three forces, which are the deformation force, the tension force and the perimeter force, rather than applying only the tension force or the perimeter force alongside the deformation force. The existence of the deformation force is necessary to avoid the collapsing of the tissue or the cell (in the case of taking just a single cell). The results were validated by simulation and also analytically. This study was extended to include more than one cell where cells are shrunk vertically 15% and also to include the case of taking different target lengths where a single cell is stretched vertically 10%. In all these cases the results showed that the behaviour was elastic and the relaxation time was found. Finally, the elasticity in the case of stretching an infinite number of cells (Tissues are composed of many cells. Therefore, considering infinite tissue in the model is justified) analytically was studied and confirmed.

In chapter 3, a novel mathematical model was constituted to reproduce the cell-edge distribution that have been observed in the biological data, which is represented by master equations using the vertex dynamics model, and to overcome the shortcomings of the previous models. In this model, firstly, the basic form is constructed which represents the rate of change of the fractions of the number of edges in the cells over a short period of time. Three ways of dividing cells were

examined: the uniformly oriented divisions, the binomially oriented divisions and the equal split divisions, the latter being, biologically, the most realistic. The equal split results associating with the fact that the probability of cellular division increases exponentially with the number of the cell edges, showing a significant agreement with the experimental observations. A cellular automata model was constructed using the equal split process and the outcomes were compatible with the biological data.

Chapter 4 is focuses on the building of a new code within the open software, Chaste, to simulate the dynamic behaviour of the epithelial tissues that takes into account the cell rearrangements, especially the T1-transitions. It was concluded that there is an approximately exponential relationship between the number of edges that are affected by this process and the probability of this process occurring. This chapter also deals with the construction of a new mathematical model which by associating with the exponential relationship, reproduces one of the topological characteristics in the epithelial tissues, namely the distribution of the number of edges per cell in an epithelial tissue which is undergoing plastic deformation. The computational results which come from the simulation and the mathematical model show that there is a very good agreement with the biological observation, taking into account the population of the tissue and the time duration of running the simulations. An automata model was also made to reproduce the cell-edge distribution undergoing the T1 process. The results were compatible with the experimental data.

A paper based on the results, short version, of chapter three and four was published in arXiv: 1710.08527 and also submitted to the Physical Review Letters journal (1).

In chapter 5, the findings of the research are discussed and some areas for future research raised. The behaviour of a stretched epithelial tissue is discussed as well as the strength and weakness of the existing mathematical models for reproducing the distribution of the number of edges per cell in a tissue undergoing cellular divisions, and how this model is distinguished from the others. The dynamic behaviour of the epithelial tissue undergoing the process of T1-transition is also discussed.

Chapter 2

Mechanical properties of tissue in Chaste implementation of the vertex dynamics model

Abstract

Mechanical properties of biological cells and tissues have recently been under intensive investigation. It has been demonstrated experimentally that cells and epithelial tissues behave as an elastic material in response to short-time deformations and exhibit plasticity if deformed for an extended period of time. To understand physical mechanisms underlying mechanical properties of cells and tissues, numerical simulations were performed in this study, using the vertex dynamics model as implemented by Chaste. It was shown that the virtual cell in the vertex dynamics model relaxes exponentially in time in response to small deformations. Based on the analysis of the dynamics of a single cell, it was found that the elasticity is conditioned by an interplay between forces postulated in the vertex model, namely between the tension and/or perimeter constraint forces from one side and deformation (volume-constraint incompressibility) force on the other. The simulations in this work also showed that the tissue containing many cells remains elastic although its relaxation time (the time that required for the cell to get e-times closer to

equilibrium) increases linearly with its size. The numerical results were confirmed analytically. In particular, an analytical model of a single cell was designed and it was shown that the deformed cell relaxes elastically, provided that the deformation is small (the number of cell edges is not changed). In this study, also the elasticity of relaxation of an infinite number of cells with infinite relaxation time was confirmed analytically.

2.1 Introduction

It is known that deformed cells and tissues act as visco-elastic materials. Elasticity is the capability of a body to recover its initial un-deformed situation after stopping the causes of the deformation where the deformation, in this case, is called elastic and, otherwise, is called plastic (53), (58). In physics, elastic and viscous materials are generally studied separately. Bausch and his co-workers (8) have locally measured the viscoelastic properties of the adherent cell surfaces by designing a magnetic bead microrheometer. They found that, as in Figure 4 in their published paper (8), the relaxation time of a stretched membrane is around 1 s. for a cell of roughly 10 μm. In their experiment the cell is subjected to the force of 2000 pN.

Most biological studies have focused on elastic properties of organs. Elasticity, for example, was investigated in experiments on plant cells (59) and in studies of an extrusion of epithelial cells from their own sheets (51). On microscopic scale, the impact of fundamental protein components of the cytoskeleton, such as the actin filaments, intermediate filaments and microtubules, on the elastic properties of cells were examined by Janmey and co-workers (45). They found that all these components contributed significantly to the elastic properties of cells, although the actin filaments have the largest impact and, therefore, play the most significant role in maintaining cellular shapes. Thus, the deformed epithelial cell produces its own inner force that comes from the rearrangement of the actomyosin networks. This epithelial cell shows an elastic deformation which keeps its integrity. Consequently, the epithelial tissues are often considered as elastic materials in theoretical studies (48; 71). The elasticity is evident under the short time-scale deformations and manifested by the tendency of cells to restore their original shapes. However, cells

that are subjected to an external force for a relatively long time (a few minutes) exhibit liquid-like behaviours and show a plastic deformation (32). In general, viscoelasticity plays a pivotal role in tissue morphogenesis (72). Epithelial tissues are commonly represented by a unicellular sheet with the cell-cell junctions on its apical side forming a polygonal and elastic two-dimensional network (37; 44).

In this study elasticity of the epithelial cell and tissues were examined using the vertex dynamics model. Cells in this model are represented by polygons whose vertices move under the influence of three distinct forces: tension force along the edges, F_i, cell-area constraint force F_d, and cell-perimeter constraint force, F_p. This model had previously been used (20; 68) for numerical studies of tissue dynamics as affected by cellular processes such as cellular division and rearrangement. Here this model was used for analysis of mechanical relaxation of deformed cells.

In the first set of numerical simulations, a single cell was stretched/shrunk, then released to check how it relaxed to an equilibrium state. Consequently, it was observed that the relaxation is exponential with the characteristic time, depending on the balance of the three forces. These numerical results were also confirmed analytically. In the second set of numerical simulations, a virtual tissue comprised of more than one cell was stretched/shrunk and its dynamics analysed after the stretching/shrinking force had been removed. It was noted that if the deformation of the tissue is not large, the relaxation is still elastic with the characteristic time increasing linearly with the number of cells in the tissue. Thirdly, relaxation of a single cell was studied in a modified vertex dynamics model, namely in the model where the tension force F_i involves non-zero target length of cell edges. In this case, the relaxation time for elastic deformations depends on the target length in a quadratic manner if all three forces are applied or a bell-shaped manner in the absence of the perimeter force, F_p. Although the analytical study of the tissue has strong limitations, it was shown analytically that the tissue composed of an infinite number of cells is still elastic but its relaxation time is infinite (Tissues have consisted of many cells. thus, considering infinite tissue in the model is justified).

2.2 Forces in the vertex dynamics model

Cells in the vertex dynamics model are represented by polygons, and cellular dynamics is defined by the motion of cell vertices (20; 68). Furthermore, in this model it is postulated that vertices are massless particles moving under the influence of four forces: friction force, F_{fr}, tension forces, F_i, acting along the cell edges merging at the considered vertex, area constrain (or resistance-to-deformation force), F_d, and perimeter constrain force, F_p. Thus,

$$\boldsymbol{F}_{fr} + \boldsymbol{F}_i + \boldsymbol{F}_d + \boldsymbol{F}_p = \boldsymbol{0} \tag{2.1}$$

The main assumptions concerning these forces in the vertex model are as follows:

- Friction force is proportional to the vortex velocity, $\boldsymbol{F}_{fr} = -\eta \boldsymbol{V}$, where η is the coefficient of friction which in this study is assumed to be 1.
- The other three forces are considered to be conservative and defined by their potentials: $\boldsymbol{F}_d = -\boldsymbol{\nabla} U_d$, $\boldsymbol{F}_i = -\boldsymbol{\nabla} U_i$, and $\boldsymbol{F}_p = -\boldsymbol{\nabla} U_p$.

Thus:

$$\eta \boldsymbol{V}_i = -\boldsymbol{\nabla} U_d - \boldsymbol{\nabla} U_i - \boldsymbol{\nabla} U_p, \tag{2.2}$$

or

$$\eta \frac{d\boldsymbol{r}_i}{dt} = -\boldsymbol{\nabla}(U_i + U_d + U_p), \tag{2.3}$$

where $\boldsymbol{r}_i$ is the position of vertex i and $\boldsymbol{\nabla}$ is the gradient notation.

Each of the three potential forces has a different objective: the tension force, F_i, acts to shrink the edge length as in Figure 2.1(a); similarly, the perimeter force, F_p, acts to shrink the entire perimeter of the cell and, finally, the area-constraint force, F_d, works towards keeping the cell area close to the predefined target area as in Figure 2.1(b).

Tension force does not depend on the size of edges and in order to include the dependency of forces on the edge size, the perimeter force is needed.

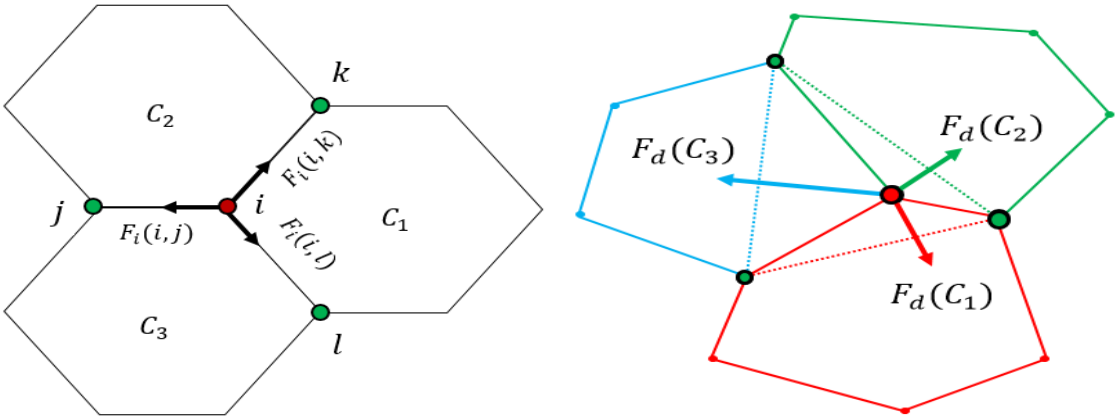

(a) (b)

Figure 2.1: Fragment of virtual tissues modelled by the vertex dynamics model and show the effect of the forces. (a) The effect of the tension forces on a vertex i. (b) The effect of the deformation forces on a vertex i.

2.2.1 The tension force

Potential for the tension force acting along the edge, which connects vertices i and j, is defined as:

$$U_i(i,j) = \sigma \left| \boldsymbol{r}_i - \boldsymbol{r}_j \right| \tag{2.4}$$

where parameter σ refer to the energy per unit length of edge and can be different for the edges located between cells and the edges on the periphery of tissue, $|\boldsymbol{r}_i - \boldsymbol{r}_j|$ represents the Euclidean distance between the vectors $\boldsymbol{r}_i$ and $\boldsymbol{r}_j$. Tension forces act along all edges and, therefore, there are three tension forces acting on the vertex connecting three edges (i.e. vertices i, j, k and l in Figure 2.2), or two for vertices connecting only two edges (i.e. vertices m, n and o in Figure 2.2). Thus, the tension force, $\boldsymbol{F}_i$, acting on the vertex i along the edge (i,j) is defined as

$$\boldsymbol{F}_i(i,j) = -\boldsymbol{\nabla} U_i(i,j) = -\sigma \boldsymbol{\nabla}_i \left| \boldsymbol{r}_i - \boldsymbol{r}_j \right| = -\sigma \frac{\boldsymbol{r}_i - \boldsymbol{r}_j}{\left| \boldsymbol{r}_i - \boldsymbol{r}_j \right|}. \tag{2.5}$$

where $\boldsymbol{\nabla}_i$ is a short notation for $\boldsymbol{\nabla} \boldsymbol{r}_i$.

For that, let $\boldsymbol{r}_i = (x,y)$, and $\boldsymbol{r}_j = (x_1,y_1)$ and hence $\boldsymbol{\nabla_i} \left| \boldsymbol{r}_i - \boldsymbol{r}_j \right| = \boldsymbol{\nabla_i} (\sqrt{(x_1-x)^2 + (y_1-y)^2}) = \frac{(x,y)-(x_1,y_1)}{\sqrt{(x_1-x)^2+(y_1-y)^2}} = \frac{\boldsymbol{r}_i - \boldsymbol{r}_j}{|\boldsymbol{r}_i - \boldsymbol{r}_j|}$ and this force pushes the vertices on the opposite sides of the edge towards each other. It is evident from symmetry that the sum of the tension forces acting along three edges merging at the vertex in tissue formed by equilateral hexagons is zero.

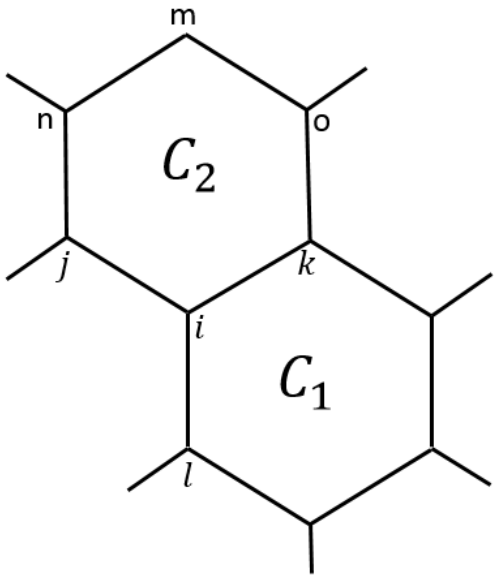

Figure 2.2: Fragment of virtual tissue modelled by the vertex dynamics model

Furthermore, the force $\boldsymbol{F}_i$ can be modified by including the none-zero target length, l, so that the modified force, $\boldsymbol{F}_e$, acts to maintain the target distance (the edge length) between vertices rather than towards the complete collapse of the edge:

$$F_e(i,j) = -\sigma\left(|\boldsymbol{r}_i - \boldsymbol{r}_j| - l\right)\frac{\boldsymbol{r}_i - \boldsymbol{r}_j}{|\boldsymbol{r}_i - \boldsymbol{r}_j|^2}. \tag{2.6}$$

2.2.2 The resistance to the deformation due to incompressibility (deformation force)

Potential associated with incompressibility of a single cell, α, for example C_1 in Figure 2.2, is defined as:

$$U_{d\alpha} = \rho_\alpha (S_\alpha - S_\alpha^\circ)^2, \tag{2.7}$$

where ρ_α is a positive constant and S_α, S_α° are the area and the target area of the cell α respectively. The associated force is given by the gradient:

$$\boldsymbol{F}_d = -\boldsymbol{\nabla} U_{d\alpha} = -2\rho_\alpha (S_\alpha - S_\alpha^\circ)\boldsymbol{\nabla}(S_\alpha - S_\alpha^\circ). \tag{2.8}$$

The vertex located in the middle of the tissue belongs to three cells and therefore is subject to three deformation forces, each given by a gradient of corresponding potential. For example, the vertex i is subjected to the force due to deformation of

cell C_1 in Figure 2.2. The gradient in the area of the cell C_1 can be given as

$$\boldsymbol{\nabla}_i S_{ij} = \boldsymbol{\nabla}_i \frac{1}{2}\boldsymbol{K} \cdot [(\boldsymbol{r}_i - \boldsymbol{r}_k) \times (\boldsymbol{r}_l - \boldsymbol{r}_k)] = \frac{1}{2}[(\boldsymbol{r}_l - \boldsymbol{r}_k) \times \boldsymbol{K}], \tag{2.9}$$

$\boldsymbol{K}$ is a unit vector perpendicular to the surface of the paper and $\boldsymbol{\nabla}(S_\alpha^\circ) \approx 0$.
For the derivation of this formula, let $\boldsymbol{r}_i = (x, y)$, $\boldsymbol{r}_l = (x_1, y_1)$, and $\boldsymbol{r}_k = (x_2, y_2)$. Hence

$$\boldsymbol{\nabla}_i \frac{1}{2}\boldsymbol{K} \cdot [(\boldsymbol{r}_i - \boldsymbol{r}_k) \times (\boldsymbol{r}_l - \boldsymbol{r}_k)] = \boldsymbol{\nabla}_i \frac{1}{2}(0,0,1) \cdot \begin{vmatrix} \boldsymbol{i} & \boldsymbol{j} & \boldsymbol{k} \\ x - x_2 & y - y_2 & 0 \\ x_1 - x_2 & y_1 - y_2 & 0 \end{vmatrix}$$

$= \boldsymbol{\nabla}_i \frac{1}{2}((x - x_2)(y_1 - y_2) - (y - y_2)(x_1 - x_2)) = \frac{1}{2}((y_1 - y_2)\boldsymbol{i} - (x_1 - x_2)\boldsymbol{j}) = \frac{1}{2}[(\boldsymbol{r}_l - \boldsymbol{r}_k) \times \boldsymbol{K}]$
where $\cdot$ and $\times$ refer to the dot product and cross product respectively. This force acts to return the area of a cell to the target area, here the target area was assumed to be 1.

The deformation force depends only on the volume of the cells and has nothing to do with bending or shape of the cells.

2.2.3 The perimeter force

Potential for a perimeter constraint force for the cell α is defined as:

$$U_{p\alpha} = \gamma_\alpha L_\alpha^2, \tag{2.10}$$

where γ_α is the positive constant (representing the coefficient of contractibility) and L_α represents the perimeter of the cell α. The corresponding force is given by the gradient:

$$\boldsymbol{F}_p = -\boldsymbol{\nabla} U_{p\alpha} = -2\gamma_\alpha L_\alpha \boldsymbol{\nabla} L_\alpha, \tag{2.11}$$

where

$$\boldsymbol{\nabla} L_\alpha = \frac{\boldsymbol{r}_i - \boldsymbol{r}_l}{|\boldsymbol{r}_i - \boldsymbol{r}_l|} + \frac{\boldsymbol{r}_i - \boldsymbol{r}_k}{|\boldsymbol{r}_i - \boldsymbol{r}_k|}, \tag{2.12}$$

Again the vertex which belongs to three cells is subject to the three corresponding perimeter constraint forces.

There is no need to use the perimeter force if the tension force is replaced by Fe, but it is decided to retain it in order to compare the model with its previous version. Hence, in the equation of the motion (see Equation(2.3))

$$F_i = -2\sum_{j}^{(i)} \sigma_{il}, \sigma_{ik} \frac{\boldsymbol{r}_i - \boldsymbol{r}_j}{|\boldsymbol{r}_i - \boldsymbol{r}_j|}, \tag{2.13a}$$

$$F_d = -\sum_{j}^{(i)} \rho_{ij}(S_{ij} - S_{ij}^{\circ})[(\boldsymbol{r}_l - \boldsymbol{r}_k) \times \boldsymbol{K}], \tag{2.13b}$$

$$F_p = -\sum_{j}^{(i)} \gamma_{ij} L_{ij} \left(\frac{\boldsymbol{r}_i - \boldsymbol{r}_l}{|\boldsymbol{r}_i - \boldsymbol{r}_l|} + \frac{\boldsymbol{r}_i - \boldsymbol{r}_k}{|\boldsymbol{r}_i - \boldsymbol{r}_k|} \right), \tag{2.13c}$$

The three sums are taken over the most three nearby adjacent vertices which are j, l and k of the vertex i.

It is important here to refer that the lipid bilayer is one of the fundamental component parts of the cell membrane, which is very thin in comparison to the average diameter of the cell. This component can be represented by a planar mathematical surface. Helfrich (36) suggested the following formula to find the curvature energy per unit volume of the closed lipid bilayer:

$$f_c = \frac{\kappa_c}{2}(2H - C_0)^2 + \bar{\kappa}K \tag{2.14}$$

where κ_c and $\bar{\kappa}$ refer to the flexural rigidities (resistance generated by a structure that undergoing bending), C_0 represents the spontaneous curvature, H and K represent the mean and the Gaussian curvature respectively. In this work, the membrane is represented by a straight lines with zero curvature and therefore this formula gives zero energy.

2.3 Simulation of the tissue using Chaste

Imposing the forces on the vertices of the polygons that represent the cells plays a central role in the vertex dynamics model. These forces are the tension force F_i, the deformation force F_d, and the perimeter force F_p. Each of these forces has a different objective. The tension force acts to shrink the edges; the deformation force constrains the area of the cells to the imposed target area (it is not bending).

Finally, the perimeter force acts to return the perimeter of the cells to the target perimeter, which in this part of study is assumed to be zero.

Consequently, collapsing of the tissues is unavoidable in the absence of the deformation force as shown in Figure 2.3, where the images of virtual tissue simulated in the absence of the deformation force are presented. This collapsing of cells results

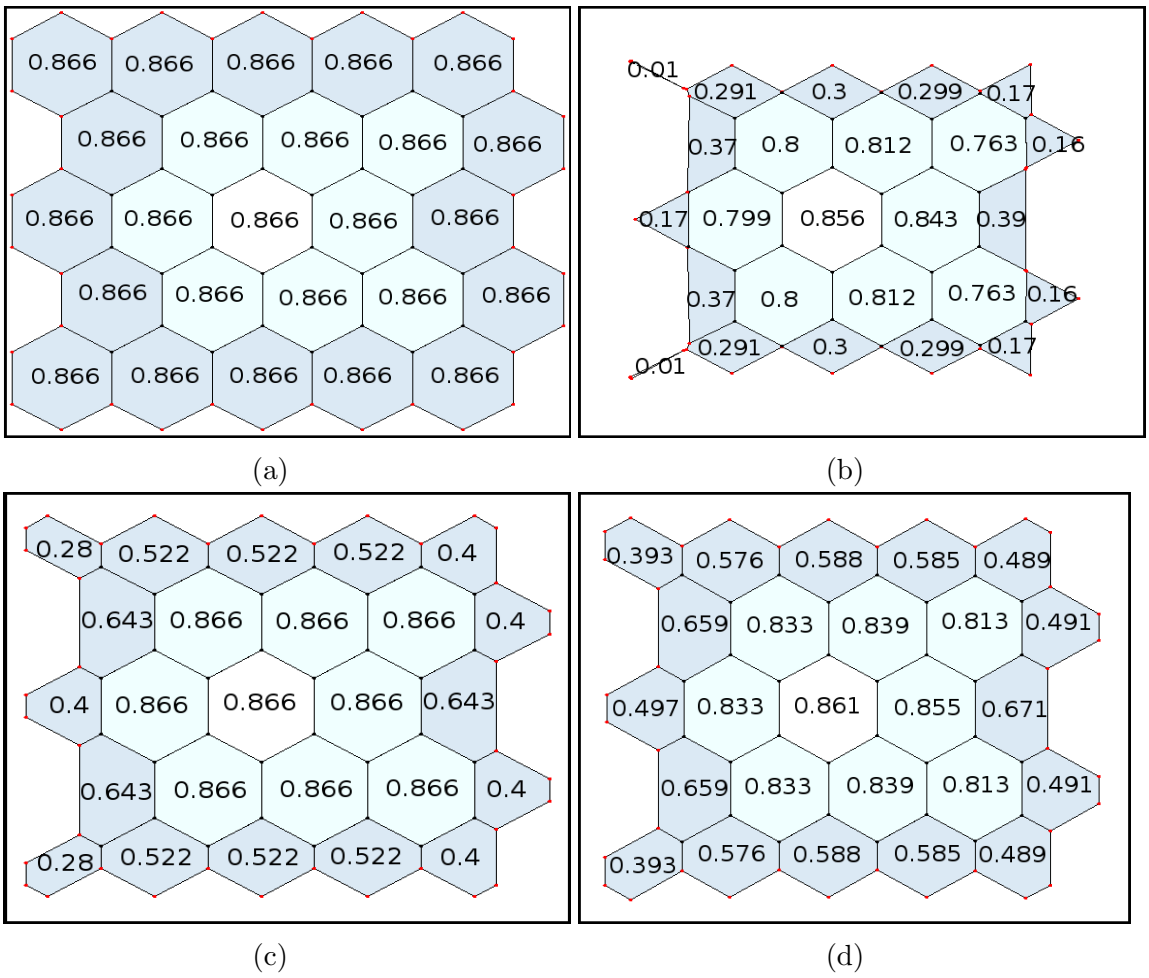

Figure 2.3: Illustration of the tissue collapse in the absence of the deformation force, F_d. Three simulations with different combinations of forces F_i and F_p are shown with the image of the tissue at time $t = 7$ in all three cases. (a) Initial configuration (at time $t = 0$) of the tissue. (b) The tissue at time $t \approx 7$ when only forces F_i and F_p are imposed. (c) The tissue at time $t \approx 7$ when only force F_i is imposed. (d) The tissue at time $t \approx 7$ when only force F_p is imposed.
One can see that the tissue is collapsing in all cases, and the collapse is the fastest on the panel (b), slower on the panel (d) and the slowest on the panel (c). Forces F_i and F_p were simulated with parameters $\sigma = 0.05$ and $\gamma = 0.007$ in all three simulations. The numbers inside the cells represent the area of the cells.

from assuming the target length and target perimeter are zero. The effect of the perimeter force depends on the target perimeter, if the target perimeter is zero then

the perimeter force does not prevent the cell from collapsing.

Figure 2.3 starts with an initial case in which each cell is a regular hexagon with the value of each edge size is allocated as a default by Chaste software to 0.57735, and since the area of the regular hexagon is given by

$$\frac{3\sqrt{3}}{2}.(edge\ length)^2,$$

therefore the area of each cell is 0.866. In this figure, initially, 5×5 cells are taken and three situations are examined in which the forces F_i and F_p, the force F_i, and the force F_p are applied to the vertices. As can be seen in Figure 2.3, the cells collapse in the presence of the two forces faster than when applying one of these forces and also the cells collapse faster in the case of applying the force F_i instead of the force F_P. Figure 2.3c shows that the collapsing of the cells in the case of applying the tension force starts from the outer cells and then proceeds to the next outer cells and so on. In each state, the collapsing of the outer cells does not affect the area and the length of the edges of the inner cells. In addition, the situation in the case of applying the perimeter force is different, where the collapsing affects all cells but where the greater the distance between a cell and the cell located in the centre, the greater the state of collapse of this cell, as in Figure 2.3d. These different effects of the forces are because of the nature of each of these forces on the cells, where the deformation force regulates the area of the cells, the tension force regulates the length of cell edges and the perimeter force deals with the perimeter of the cells.

To maintain the stable tissue, the force F_d is imposed with one or both of the other forces, F_i, F_p. The default values of the parameters enable the construction of standard situations that can be used for the comparison of different cases where the parameters of the forces are changed. To set particular numerical values to these three parameters defining forces in vertex model it was noted that multiplication of all three parameters by the same factor does not change the state of the virtual tissue in the long run. Therefore one of the parameters (i.e. ρ) can be set to one without loss of generality. Furthermore, it was shown that the deformation force should be of the same order as at least one of the two other forces (see Figure 2.3). Thus tension and perimeter forces in default setting are assumed to be neither too

small nor too big. As a measure of the strength of these two forces, their impact on the volume of the cell was considered: a 5% reduction of the volume was considered a reasonable impact of these two forces. Tension force results in a 5% reduction of cell volume when $\sigma = 0.05$ and perimeter force results in a 5% reduction when $\gamma = 0.007$. Therefore the values $\sigma = 0.05$, $\rho = 1$, and $\gamma = 0.007$ were selected as their default values. Hence, applying the forces F_d, F_i and F_p, where the parameters are in their default values, resulted in increasing the area of the cells to reach 10% less than the target area value (Figure 2.4a). Furthermore, applying the forces F_d and F_i or the forces F_d and F_p, where the parameters of these forces in their default values causes an increase in the area of the cells to reach 5% less than the target area value, which is 0.95 (Figure 2.4b).

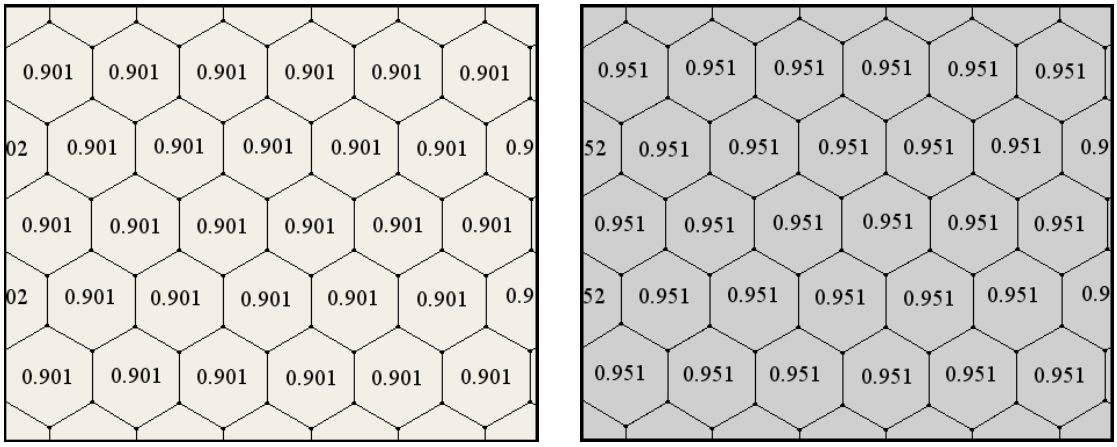

Figure 2.4: Tissues formed by regular hexagonal cells are shown. (a) The area of cells in a stationary tissue, when all three forces, F_d, F_i, and F_p, are imposed, is 0.901. (b) The area of cells in a stationary tissue, when the force F_d with one of the forces F_i, or F_p is imposed, is 0.951. Parameter values: $\rho = 1$, $\gamma = 0.007$ and $\sigma = 0.05$, target area is set to 1 in both cases.

Now, since the presence of the force F_d is necessary to avoid the collapsing of the tissue, the cases of applying the force F_d with one or both of the other two forces were studied. The area of the cells has a target value that relies on the type of the forces that the vertices of the cells in the tissue were subjected to. Furthermore, the time that these cells required to reach this target value depended on the number of the cells in the tissue.

The Figures 2.3 and 2.4 were implemented in the isotropy case, where the cells had been subjected to the forces without any stretching and the tissue was selected

to be N by N cells.

The simulations results showed that the multiplying all parameters of the forces that act on the vertices of cells by a real number r does not result in any changes in the destination area value; rather it results in changes in the time that the cells need to reach that area value (Figure 2.5).

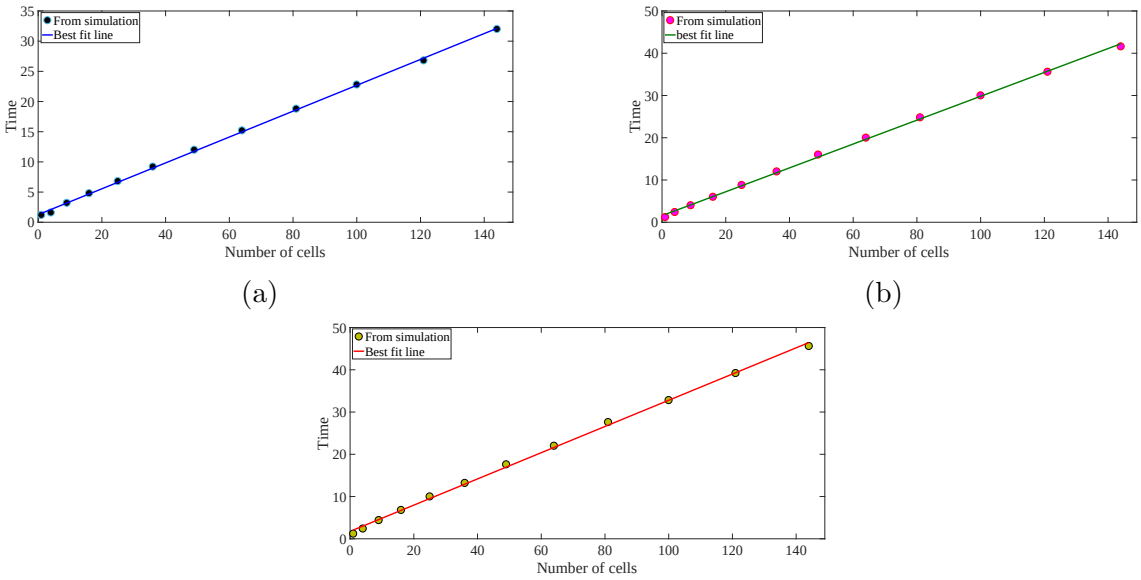

Figure 2.5: The relation between the number of cells and the time that these cells need to reach the destination area. (a) The relation in the case of applying the forces F_d, F_i and F_p and the destination area is 0.9, (b) The relation in the case of applying the forces $F_d$and F_i and the destination area is 0.95, (c) The relation in the case of applying the forces F_d and F_p and the destination area is 0.95, In all this cases r is taken to be 1.

The time can be given as

$$\frac{1}{r}t$$

where, for applying the forces F_d, F_i and F_p (Figure 2.5a), $t = 0.2143Z + 1.2578$.
For applying the forces F_d and F_i (Figure 2.5b), $t = 0.2824Z + 1.5687$,
and for applying the forces F_d and F_p (Figure 2.5c), $t = 0.3102Z + 1.7619$,
where $Z = N^2$ is the number of cells in the tissue and $N = 1, 2, 3, ...$ and t represents the time that the cells need to reach the destination area value when $r = 1$.

However, increasing or decreasing the parameter value of one force, in the case of there existing more than one, and keeping the other(s) at the default value(s) changes the destination area value. For example, in the case of applying the forces F_d with one of the forces F_i or F_p, the destination area value increases and the cells

expand, as a result of multiplying ρ by a constant r and fixing the other parameter at the default value, where r is a real number ($1 < r < 20$). However, the destination area value decrease and the cells shrink, as a result of multiplying $\sigma/\ \gamma$ by a constant r and fixing ρ at the default value, where r is a real number ($1 < r < 20$). The situation will be reversed in the case of multiplying these parameters by $1/r$.

There are symmetrical configurations about $r = 1$ with respect to the values of areas between those relating to multiplying ρ by r and fixing the other parameter, whether it is σ, or γ on one side, and those relating to multiplying σ or γ by $1/r$ and fixing ρ on the other side, as shown in Figure 2.6. This figure also shows that the area value approaches 1 in both cases; versus $r\rho$, with the other parameter fixed and versus $(1/r)\sigma$ or $(1/r)\gamma$, fixing the value of ρ as r approaches 20. However, the area becomes smaller and smaller versus $r\gamma$ and ρ or $(1/r)\rho$ and γ and approaches zero as r approaches 20, the cells collapsing as versus $r\sigma$ and ρ or $(1/r)\rho$ and σ with $r > 8$. A similar behaviour can be observed when applying the forces F_d, F_i, and F_p, where multiplying one parameter by r gives the same area as that can be obtained from multiplying the other two parameters by (1/r) and vice versa, as shown in Figure 2.7.

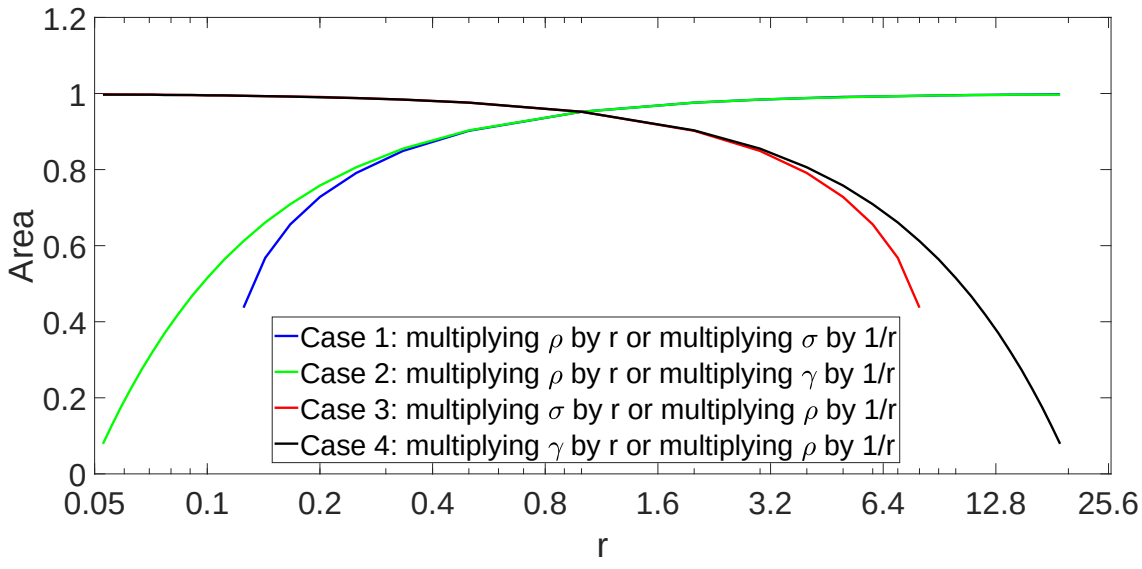

Figure 2.6: Area of cells as a function of model parameters. Only two forces F_d with F_i or F_d with F_p are applied for the default values $\rho = 1$, $\sigma = 0.005$, and $\gamma = 0.007$. Case 1: multiplying ρ by r or multiplying σ by 1/r. Case 2: multiplying ρ by r or multiplying γ by 1/r. Case 3: multiplying σ by r or multiplying ρ by 1/r. Case 4: multiplying γ by r or multiplying ρ by 1/r.

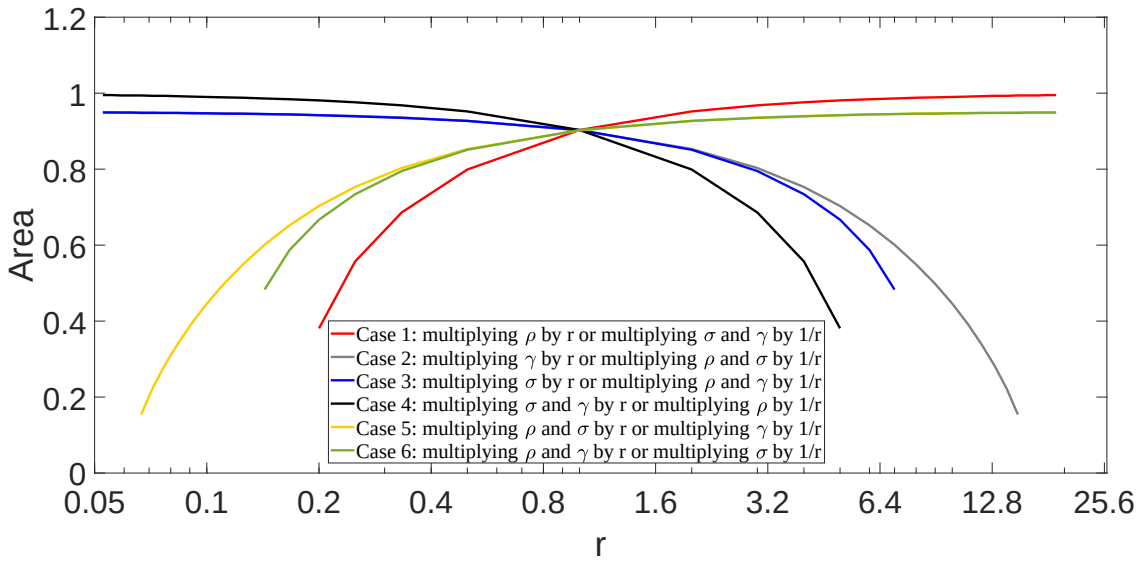

Figure 2.7: Area of cells as a function of model parameters. All three forces F_d, F_i, and F_p are applied. for the default values $\rho = 1$, $\sigma = 0.005$, and $\gamma = 0.007$. All three forces F_d, F_i, and F_p are applied. Case 1: multiplying ρ by r or multiplying σ and γ by 1/r. Case 2: multiplying γ by r or multiplying ρ and σ by 1/r. Case 3: multiplying σ by r or multiplying ρ and γ by 1/r. Case 4: multiplying σ and γ by r or multiplying ρ by 1/r. Case 5: multiplying ρ and σ by r or multiplying γ by 1/r. Case 6: multiplying ρ and γ by r or multiplying σ by 1/r.

Using the vertex dynamics model the behaviour of deformed (stretched) tissue was also examined. The results of corresponding simulations are shown in the Figures 2.8 and 2.9. Tissue deformed to a certain extension completely recovers (elastic deformations (see Figure 2.8) while larger deformation causes certain plasticity when the tissue does not completely recover (see Figure 2.9). These deformations were implemented by subjecting the upper and lower vertices of the upper and lower rows of the cells to an external force of magnitude 1.51 acting, simultaneously, upwards and downwards, respectively. Plasticity occurs as a result of T1-transition events (Figure 1.10) which causes exchange in cell neighbour. Later in Chapter four, T1-transition is described in detail. Moreover, tension force takes into account the adhesion between cells.

An external force was also applied with magnitude 6 to a small group of cells within the tissue to cause migration of this group of cells inside the tissue. The results of these simulations are illustrated in Figure 2.10. It can be seen that cells in contact with moving cells undergo elastic deformations which indicates that the virtual tissue in the vertex dynamics model represents a solid rather than liquid.

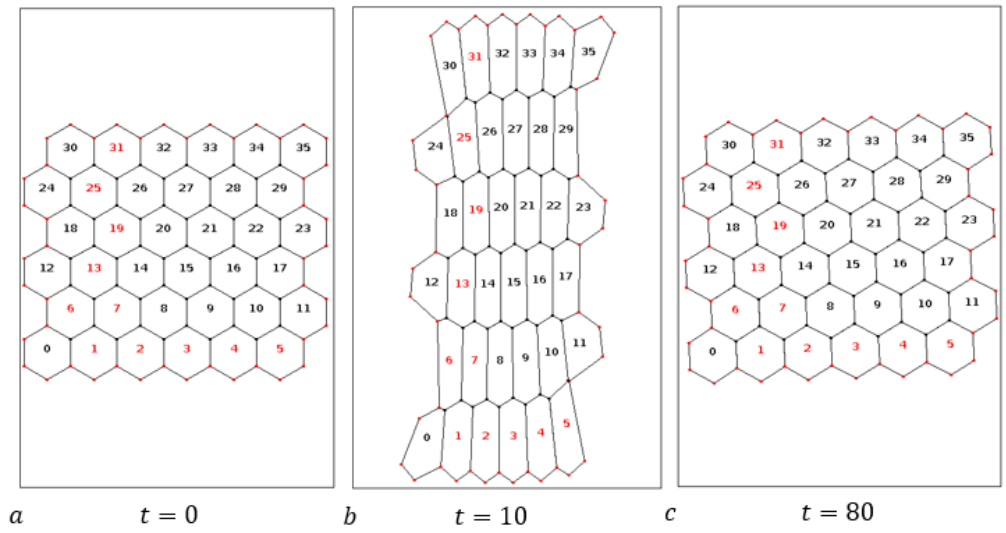

Figure 2.8: Elastic deformation. The tissue undergoes vertical stretching between the time zero and time 10 and is then released. It recovers to the original shape. All three forces are imposed with parameters: $\rho = 10$, $\sigma = 0.5$, and $\gamma = 0.07$. Here, The upper and lower vertices of the upper and lower rows of the cells are subjected to an external force of magnitude 1.51, between the time zero and time 10, acting, simultaneously, upwards and downwards, respectively. There was no T1-transition events occurred.

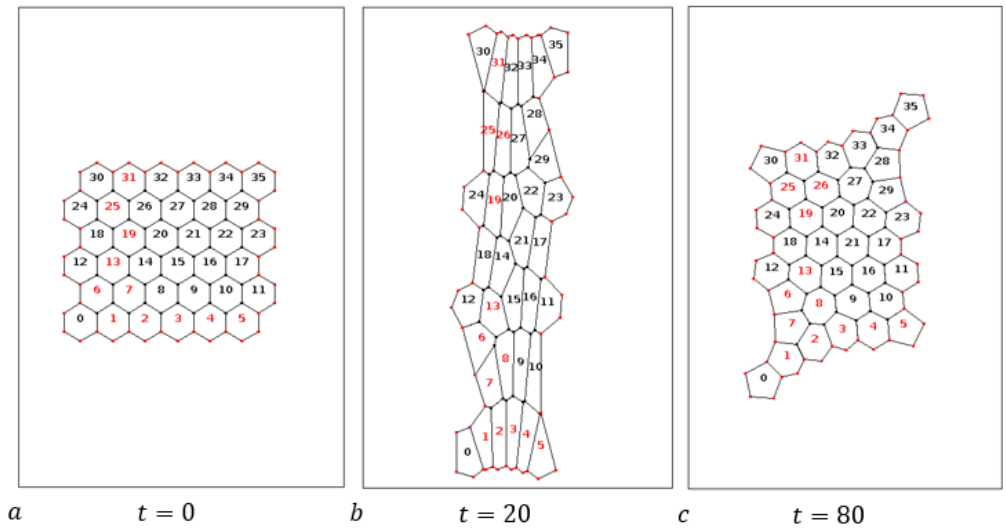

Figure 2.9: Plastic deformation. The tissue undergoes vertical stretching between the time zero and time 20 and is then released. It recovers to a great extent but does not return to the original shape. All three forces are imposed with parameters: $\rho = 10$, $\sigma = 0.5$, and $\gamma = 0.07$. Here, The upper and lower vertices of the upper and lower rows of the cells are subjected to an external force of magnitude 1.51, between the time zero and time 20, acting, simultaneously, upwards and downwards, respectively. Plasticity happens as a result of T1-transition events (Figure 1.10) which causes exchange in cell neighbours.

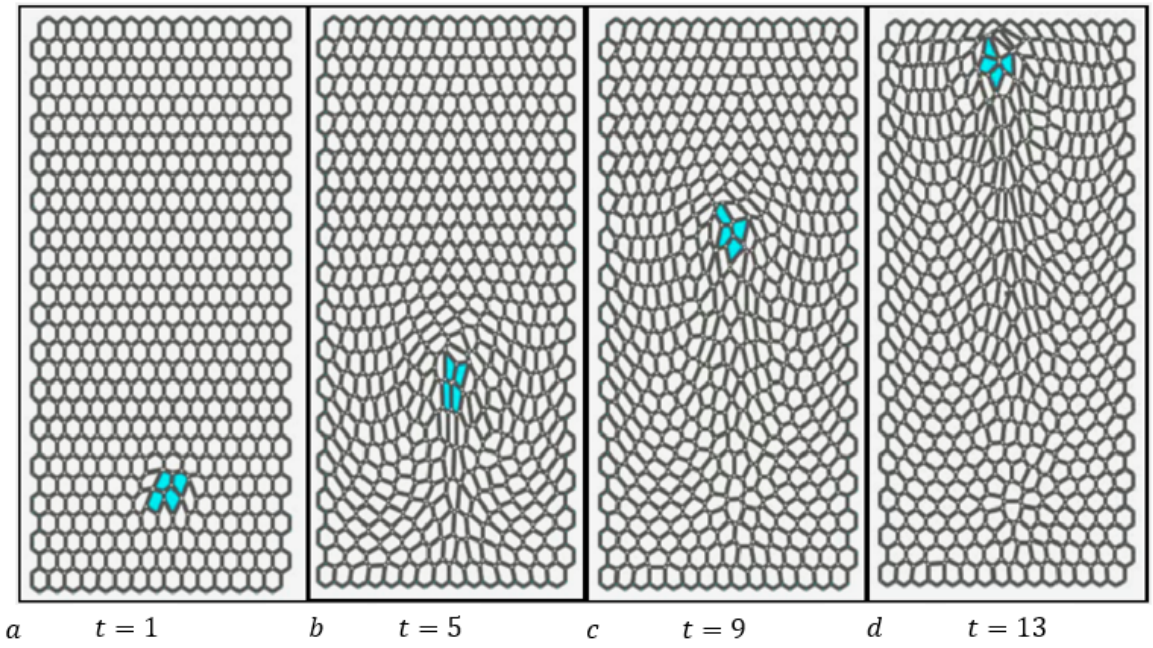

Figure 2.10: Migration of group of cells under the influence of the external force with magnitude 6 applied to the vertices of all four cells comprising the moving group. All three basic forces are imposed in this simulation. Parameter values for the blue cells: $\rho = 50$, $\sigma = 5$, and $\gamma = 20$ and for the other cells: $\rho = 50$, $\sigma = 1$, and $\gamma = 20$.

2.4 Numerical study of relaxation of deformed tissue

The study of the development of the tissues mathematically plays a considerable role in understanding the behaviour of migration and how cells proliferate, rearrange and how cells differentiate. An understanding of these processes may help to deal with deviant behaviour that may lead to many serious diseases such as cancer. In this section the process of relaxation is examined numerically to check whether the relaxation is exponential, and thereby the tissue is elastic, or the relaxation is not exponential. For this, the parameters value were restricted at the default values, whereof $\sigma = 0.05$, $\rho = 1$, and $\gamma = 0.007$, $S_0 = 1$. Moreover, imposing each of F_i, F_p, one at a time, reduces the area of the cells 5%. In this study, the following cases were investigated.

2.4.1 The case of a single cell

In the single cell case the behaviour of the relaxation for each of the situations, namely applying the forces F_d, F_i, and F_p, applying the forces F_d and F_i, and finally applying the forces F_d and F_p, was examined to determine numerically whether it is elastic or not elastic. For this, the computer simulation was carried out using the vertex dynamics model. The numerical results demonstrated that the relaxation is exponential (Figure 2.11) with the relaxation times as in Table 2.1.

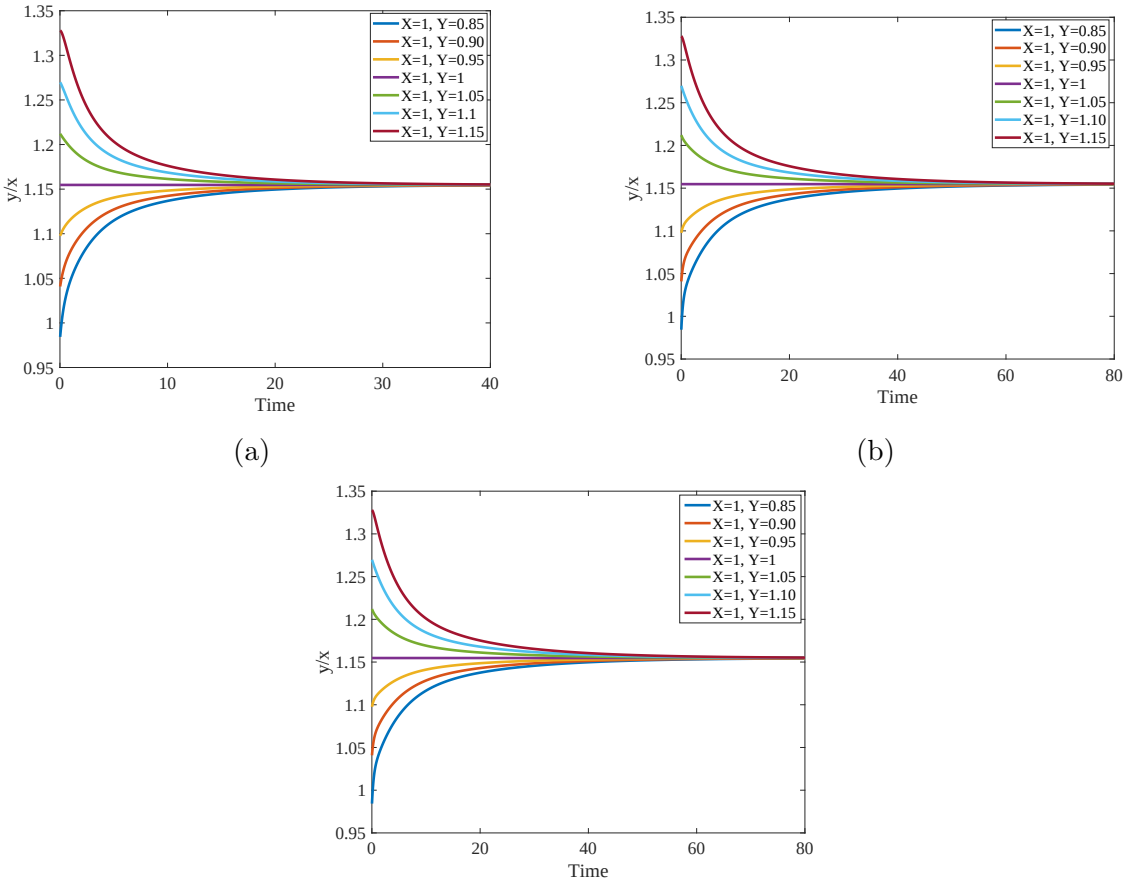

Figure 2.11: The exponential behaviour of the relaxation after stretching/shrinking a single cell in a model with the following forces: (a) F_d, F_i, and F_p; (b) F_d and F_i; (c) F_d and F_p. Model parameters: $\sigma = 0.05$, $\rho = 1$, $\gamma = 0.007$ and $S_0 = 1$. x and y are the length of the cell in the x-axis and y-axis direction, respectively. X and Y are the deformation of the cell in the x-axis and y-axis, respectively.

For example, to find the relaxation time in the case of applying the three forces with $X = 1$ and $Y = 1.15$, it is clear from the Figure 2.12 that the relaxation time $\tau = 1/0.123 = 8.13$. X and Y represent the deformation in the x-axis and y-axis direction respectively. For $Y = 1$ that is mean no deformation and $Y = 1.15$ that is mean that

The value of X and Y	τ for y/x, imposing F_d, F_i, and F_p	τ for y/x, Imposing F_d and F_i	τ for y/x, Imposing F_d and F_p
X=1,Y=0.85	8.2	16.13	15.87
X=1,Y=0.90	8.2	16.13	15.87
X=1,Y=0.95	8.13	16.13	15.87
X=1,Y=1.00	- - -	- - -	- - -
X=1,Y=1.05	8.06	16.13	15.87
X=1,Y=1.10	8.13	16.13	15.87
X=1,Y=1.15	8.13	15.87	15.63

Table 2.1: The relaxation times (τ) for the three situations that are shown in Figure 2.11.

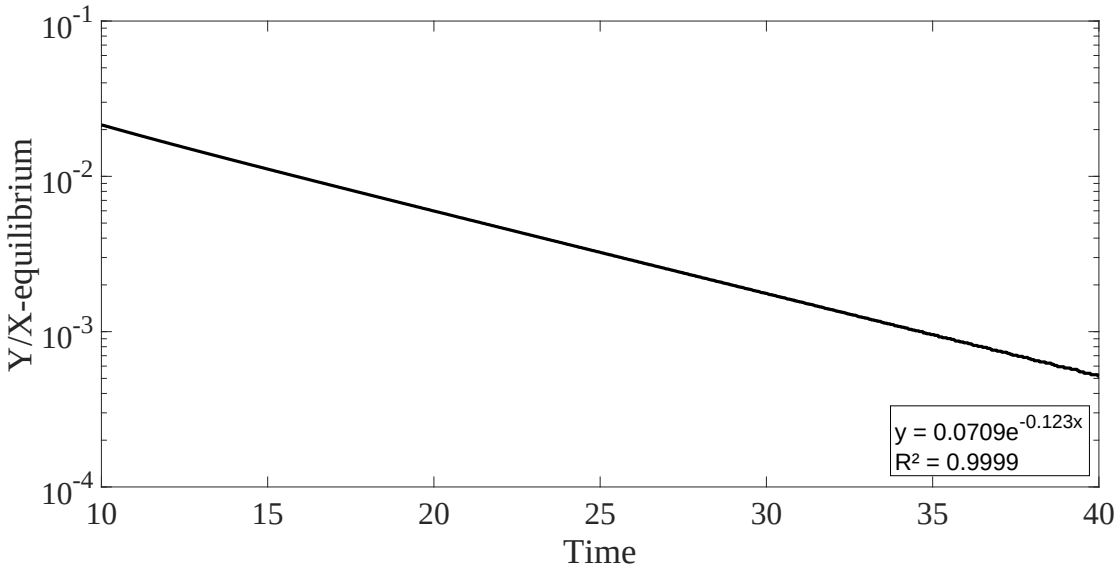

Figure 2.12: The exponential relaxation of a stretched single cell 15% in the y-axix direction after the cell subjected to the forces F_d, F_i and F_p, the parameters were in the default values.

the cell was stretched vertically 15%. The results show that the relaxation time is approximately constant with different values of stretching/shrinking in each of these three situations. One of the interesting observations is that the relaxation time is halved in the case of applying the three forces in comparison with the situation of the absence of either F_i or F_p.

2.4.2 The case of tissue containing $N \times N$ ($N \in Z^+$) cells

In case of $N \times N$ cells, the behaviour of the relaxation after applying the forces F_d, F_i and F_p was investigated to decide numerically whether it is elastic or plastic. For this, the computer simulation was implemented using the vertex dynamics model. The simulations results showed that the relaxation is exponential with the relaxation times, as in the Table 2.3. The results demonstrated that the relaxation time is linearly increased approximately with the increase in the number of cells (Figure 2.13). Table 2.2 shows that the relaxation time is roughly constant in any number of cells with different values of vertical stretching/shrinking. Moreover,

The value of X and Y	The relaxation time, imposing F_d, F_i, and F_p, The number of cells are 2×2	The relaxation time, imposing F_d, F_i, and F_p, The number of cells are 3×3
X=1,Y=0.85	33.33	71.43
X=1,Y=0.90	34.48	71.43
X=1,Y=0.95	34.84	71.43
X=1,Y=1.00	- - -	- - -
X=1,Y=1.05	35.71	66.67
X=1,Y=1.10	34.48	71.43
X=1,Y=1.15	34.48	71.43

Table 2.2: The relaxation times (τ) for the 2×2 and 3×3 number of cells and applying F_d, F_i and F_p.

the exponential behaviour of the relaxation after shrinking more than one cell, applying F_d, F_i and F_p, $X = 1, Y = 0.85$, N-cells, $t = 750, t_s = 0.02$ is given in the Table 2.3.

The number of cells	τ (F_i+F_d+F_p)
1×1	8.20
2×2	33.33
3×3	71.43
4×4	66.67
5×5	83.33
6×6	83.33
7×7	90.91
8×8	100.00
9×9	111.11
10×10	125

Table 2.3: The relaxation times (τ) for the $N \times N$ number of cells and applying F_d, F_i and F_p, where $N = 1, 2, ..., 10$. The parameters at default values.

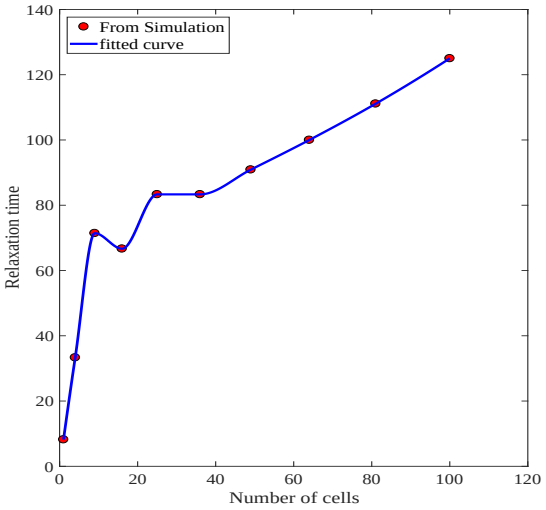

Figure 2.13: The exponential behaviour of the relaxation after shrinking more than one cell with applying F_d, F_i and F_p, $X = 1, Y = 0.85$, $N \times N$-cells, $t = 750, t_s = 0.02$. The parameters at default values.

2.4.3 The case of a single cell and modified model, applying forces F_d, F_p and F_e (F_e instead of F_i)

The force F_e is modified from F_i by taking the edge's target length into account and is defined as in the Equation (2.6).

Here, the behaviour of the relaxation, applying the forces F_d, F_e (definition of F_e is given by the formula (2.6)), and F_p is described to show numerically whether it is elastic or not by taking a single cell and different edge target lengths. The numerical results demonstrated that the relaxation is exponential, Figure 2.14a and the relation between the relaxation times and edge target lengths is quadratic, as depicted in Figure 2.14b. Here, $X = 1$ which is mean no deformation in the x-axis direction and $Y = 1.10$ which is mean the cell was stretched vertically 10%.

2.4.4 Case of a single cell and modified model with applying forces F_d, and F_e (F_e instead of F_i)

In this case, the behaviour of the relaxation, applying the forces F_d, F_e is described to determine numerically whether it is elastic or plastic by taking a single cell and different edge target lengths. The numerical results also showed that the relaxation

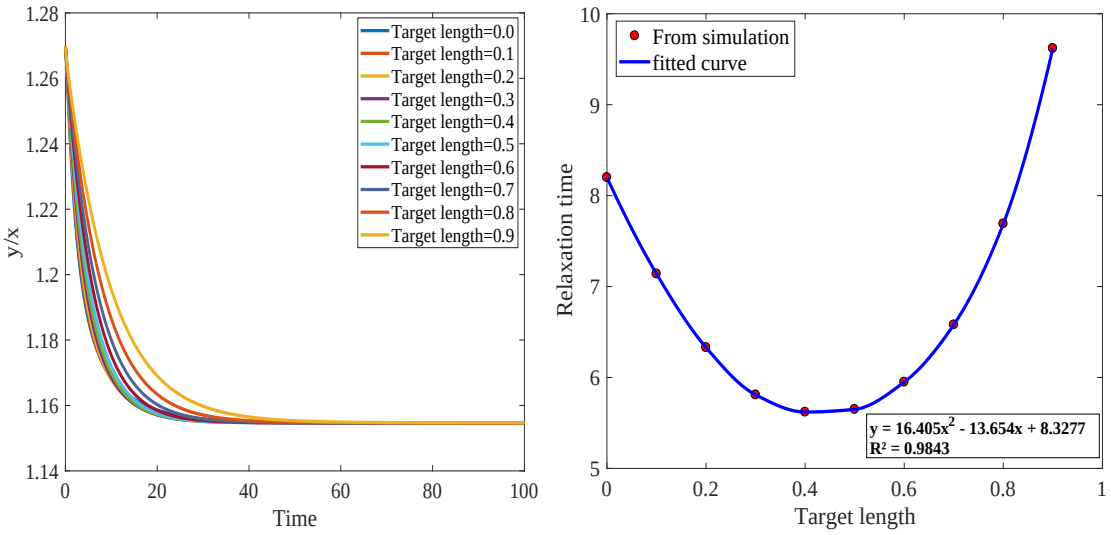

(a) (b)

Figure 2.14: (a) The exponential relaxation for a stretched cell when the forces F_d, F_e and F_p are applied (X=1,Y=1.1 with different edge target length). Here, x and y are the length of the cell in the x-axis and y-axis direction, respectively. (b) The relaxation times (τ) for a stretched single cell when forces F_d, F_e and F_p are applied and for different target values.

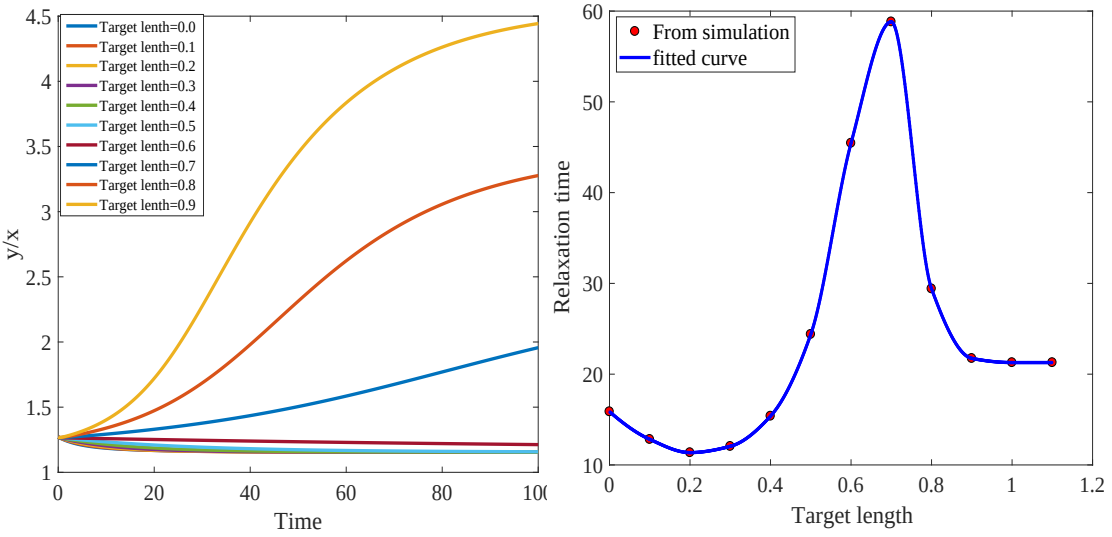

(a) (b)

Figure 2.15: (a) The exponential relaxation for a stretched cell when the forces F_d and F_e are applied (X=1,Y=1.1 with different edge target length). Here, x and y are the length of the cell in the x-axis and y-axis direction, respectively. (b) The relaxation times, applying F_d and F_e (for one cell).

is exponential, Figure 2.15a. The relationship between the relaxation times and edge target lengths is demonstrated in the bell curve shape as given in Figure 2.15b. Here, $X = 1$ and $Y = 1.10$ which is mean the cell wasn't deformed horizontally in the x-axis whereas it was stretched vertically 10%. The relaxation time depends on the target length for the given target area and has a maximum when the target length corresponds to the target area.

2.5 Analysis of the dynamics of a single deformed cell

In this section, the relaxation of a slightly deformed cell is studied analytically. For simplicity, deformations are considered which maintain certain geometric symmetry of the considered cell which is also presumed to have a hexagonal shape, as shown in Figure 2.16. For simplicity, the origin of the coordinate system is placed in the centre of the cell, therefore $x_2 = 0$ (the shape is symmetric). The three parameters a, b and α (2α is the angle $\angle ABC$) are adequate to examine the solutions analytically through finding velocities of vertices as given by the derivatives $\frac{dy_2}{dt}$, $\frac{dx_1}{dt}$, and $\frac{dy_1}{dt}$. Let $\Delta S = S^\circ - S$ where S and $S^\circ = 1$ are the area and the target area of the cell respectively. Therefore the total area of the hexagon is $S = 1 - \Delta S$. For the regular hexagon (i.e. the sum of the forces acting on the vertices =0), $2\alpha = \beta = \frac{2\pi}{3}$, where β is the angle $\angle BAF$). From the symmetrical shape (Figure 2.16), it is clear that

$$x_1 = a\sin(\alpha), \tag{2.15}$$

$$y_2 = a\cos(\alpha) + y_1 \tag{2.16}$$

In general, it can be assumed that $\alpha = \frac{\pi}{3} + \epsilon$ and therefore $\beta = \frac{2\pi}{3} - \epsilon$, $a = a_0 + \delta$, and $b = a_0 + \Delta$ (where ϵ, δ, Δ are small real numbers). By the Equations (2.15) and (2.16) the area of the shape can be given as

$$A = 2x_1(y_2 - y_1) + 2bx_1 = 2a^2\sin(\alpha)\cos(\alpha) + 2ab\sin(\alpha) \tag{2.17}$$

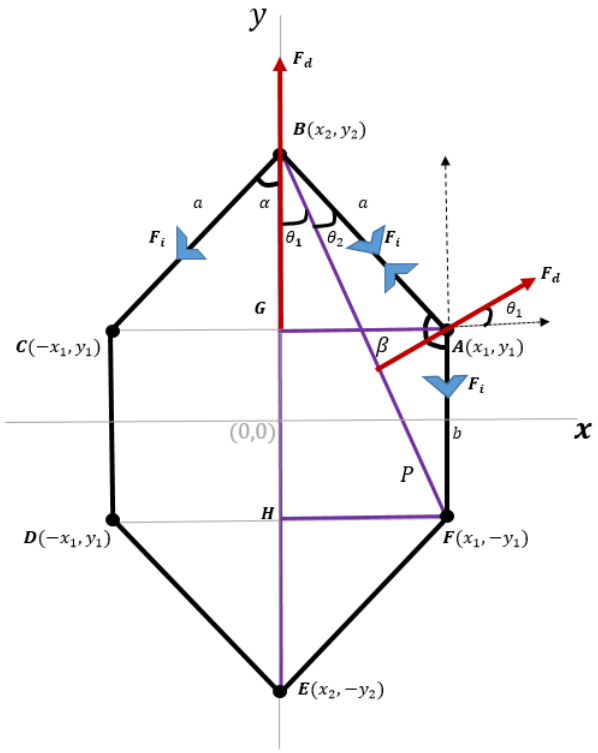

Figure 2.16: The hexagon cell with vertices A, B, C, D, E, and F and edges AB, BC, CD, DE, EF, and FA in which $AB = BC = DE = EF = a$, $AF = CD = b$, and $AC = DF$ (i.e. the cell is symmetric). 2α is $\angle ABC$, θ_1 is $\angle EBF$, and θ_2 is $\angle FBA$.

and by assuming that the area is constant we have

$A = 2(a_0+\delta)^2 \cdot \sin(\frac{\pi}{3}+\epsilon) \cdot \cos(\frac{\pi}{3}+\epsilon) + 2(a_0+\delta) \cdot (a_0+\Delta) \cdot (\sin(\frac{\pi}{3}+\epsilon))$

Using the first order approximation for sine and cosine,

$A = 2(a_0+\delta)^2 \cdot (\sin(\frac{\pi}{3}) + \cos(\frac{\pi}{3})\epsilon) \cdot (\cos(\frac{\pi}{3}) - \sin(\frac{\pi}{3})\epsilon) + 2(a_0+\delta) \cdot (a_0+\Delta) \cdot (\sin(\frac{\pi}{3}) + \cos(\frac{\pi}{3})\epsilon)$

$A = 2(a_0+\delta)^2 \cdot (\frac{\sqrt{3}}{2} + \frac{\epsilon}{2}) \cdot (\frac{1}{2} - \frac{\sqrt{3}}{2}\epsilon) + 2(a_0+\delta) \cdot (a_0+\Delta) \cdot (\frac{\sqrt{3}}{2} + \frac{\epsilon}{2})$

and hence

$A = \frac{3\sqrt{3}}{2}a_0^2 + 2\sqrt{3}a_0\delta + \sqrt{3}a_0\Delta.$

The values of the other terms are relatively very small and hence can be neglected. Since the area of the regular hexagon with side a_0 is $\frac{3\sqrt{3}}{2}a_0^2$ and since the area returns very quickly to the target area, therefore

$$\frac{3\sqrt{3}}{2}a_0^2 + 2\sqrt{3}a_0\delta + \sqrt{3}a_0\Delta = \frac{3\sqrt{3}}{2}a_0^2;$$

$$2\sqrt{3}a_0\delta + \sqrt{3}a_0\Delta = 0$$

hence

$$\Delta = -2\delta. \tag{2.18}$$

The analytical solutions for the three situations in the case of using the forces F_d with one of the forces F_p and F_i or both, using a single cell were examined analytically as follows: since we have a symmetrical hexagon cell, analysing the change of the positions of the two points A and B is adequate to be taken for this study, where the change of the positions of the other points that correspond to these two points is similar (i.e. the points B and E as well as A, C, D and F behave in a similar way). Therefore only $\frac{dy_2}{dt}$, $\frac{dx_1}{dt}$, and $\frac{dy_1}{dt}$ are needed to describe the behaviour of the relaxation. To describe these equations, the expression $\boldsymbol{\psi} = \frac{\boldsymbol{r}_i - \boldsymbol{r}_l}{|\boldsymbol{r}_i - \boldsymbol{r}_l|} + \frac{\boldsymbol{r}_i - \boldsymbol{r}_k}{|\boldsymbol{r}_i - \boldsymbol{r}_k|}$ and $\boldsymbol{\omega} = \frac{1}{2}(\boldsymbol{r}_l - \boldsymbol{r}_k) \times \boldsymbol{K}$ need to be defined using Figure 2.2 and the Equations (2.5), (2.9) and (2.12) , where $\boldsymbol{K}$ is the unit vector $(0, 0, 1)$. Hence for the vertex $\boldsymbol{B}$; $\boldsymbol{r}_i = (0, y_2)$, $\boldsymbol{r}_l = (-x_1, y_1)$ and $\boldsymbol{r}_k = (x_1, y_1)$, while for the vertex $\boldsymbol{A}$; $\boldsymbol{r}_i = (x_1, y_1)$, $\boldsymbol{r}_l = (0, y_2)$ and $\boldsymbol{r}_k = (x_1, -y_1)$ and through Equations (2.15) and (2.16) we have

$$\boldsymbol{\psi_B} = \frac{2(y_2 - y_1)\boldsymbol{j}}{a} = 2\cos\alpha\boldsymbol{j} \tag{2.19}$$

$$\boldsymbol{\psi_A} = \frac{x_1\boldsymbol{i} + (y_1 - y_2)\boldsymbol{j}}{a} + \frac{2y_1\boldsymbol{j}}{b} = \sin\alpha\boldsymbol{i} - \cos\alpha\boldsymbol{j} + \boldsymbol{j} \tag{2.20}$$

and

$$\boldsymbol{\omega_B} = x_1\boldsymbol{j} = a\sin(\alpha)\boldsymbol{j}. \tag{2.21}$$

$$\boldsymbol{\omega_A} = \frac{1}{2}((y_2 + y_1)\boldsymbol{i} + x_1\boldsymbol{j}) = \frac{1}{2}(P\cos(\theta_1)\boldsymbol{i} + P\sin(\theta_1)\boldsymbol{j}) \tag{2.22}$$

where P is denoted in Figure 2.16.

For studying the behaviour of the relaxation of stretching/shrinking a single cell analytically, we have three different cases which are studied also numerically in subsection 2.4.1.

1. **In the case of applying the forces F_d and F_i**, it is necessary to describe the three relationships $\frac{dy_2}{dt}$, $\frac{dy_1}{dt}$, and $\frac{dx_1}{dt}$. From the Equations (2.13a) and (2.13b), using the point $(0, y_2)$, $F_{iy} = -\sigma\boldsymbol{\psi_B}$ and $F_{d_y} = 2\rho\Delta S\boldsymbol{\omega_B}$. Therefore,

the derivative $\frac{dy_2}{dt}$ can be given as

$$\frac{dy_2}{dt} = F_{d_y} + F_{i_y} = 2\rho\Delta S a \sin(\alpha) - 2\sigma\cos(\alpha). \tag{2.23}$$

Moreover, for using the point (x_1, y_1), $F_{i_y} = -\sigma\boldsymbol{\psi}_{\boldsymbol{A}(\boldsymbol{y})}$, $F_{i_x} = -\sigma\boldsymbol{\psi}_{\boldsymbol{A}(\boldsymbol{x})}$, $F_{d_y} = 2\rho\Delta S\boldsymbol{\omega}_{\boldsymbol{A}(\boldsymbol{y})}$, and $F_{d_x} = 2\rho\Delta S\boldsymbol{\omega}_{\boldsymbol{A}(\boldsymbol{x})}$, where the subscripts (x) and (y) indicate that the direction of the force towards the x-axis and y-axis respectively. Hence the derivative $\frac{dy_1}{dt}$ and the derivative $\frac{dx_1}{dt}$ can be given as

$$\frac{dy_1}{dt} = F_{d_y} + F_{i_y} = P\rho\Delta S\sin(\theta_1) + \sigma\cos(\alpha) - \sigma, \tag{2.24}$$

$$\frac{dx_1}{dt} = F_{d_x} + F_{i_x} = P\rho\Delta S\cos(\theta_1) - \sigma\sin(\alpha). \tag{2.25}$$

2. **For applying the forces F_d and F_p**, the three relationships $\frac{dy_2}{dt}$, $\frac{dx_1}{dt}$, and $\frac{dy_1}{dt}$ need to be given. From the Equation (2.13c), and using the point $(0, y_2)$, $F_{p_y} = -12a_0\gamma\boldsymbol{\psi}_{\boldsymbol{B}(\boldsymbol{y})}$. In this case $\frac{dy_2}{dt}$ can be given as

$$\frac{dy_2}{dt} = F_{d_y} + F_{p_y} = 2\rho\Delta S a\sin(\alpha) - 24\gamma a_0\cos(\alpha). \tag{2.26}$$

Moreover, for using the point (x_1, y_1), $F_{p_y} = -12a_0\gamma\boldsymbol{\psi}_{\boldsymbol{A}(\boldsymbol{y})}$ and $F_{p_x} = -12a_0\gamma\boldsymbol{\psi}_{\boldsymbol{A}(\boldsymbol{x})}$. In this case $\frac{dy_1}{dt}$ and $\frac{dx_1}{dt}$ can be presented as

$$\frac{dy_1}{dt} = F_{d_y} + F_{p_y} = P\rho\Delta S\sin(\theta_1) - 12\gamma a_0(1 - \cos(\alpha)), \tag{2.27}$$

$$\frac{dx_1}{dt} = F_{d_x} + F_{p_x} = P\rho\Delta S\cos(\theta_1) - 12\gamma a_0\sin(\alpha). \tag{2.28}$$

3. **For applying the forces F_d, F_i and F_p**, the above two cases can be used to find the $\frac{dy_2}{dt}$, $\frac{dx_1}{dt}$, and $\frac{dy_1}{dt}$ as follows: By merging both the cases above

$$\frac{dy_2}{dt} = F_{d_y} + F_{iy} + F_{p_y} = 2\rho\Delta S a\sin(\alpha) - 2\sigma\cos(\alpha) - 24\gamma a_0\cos(\alpha). \tag{2.29}$$

By taking the point (A) the other two derivatives can be obtained by using

the above corresponding derivatives as given below:

$$\frac{dy_1}{dt} = F_{d_y} + F_{iy} + F_{p_y} = P\rho\Delta S\sin(\theta_1) + \sigma\cos(\alpha) - \sigma - 12\gamma a_0(1-\cos(\alpha)), \quad (2.30)$$

and

$$\frac{dx_1}{dt} = F_{d_x} + F_{ix} + F_{p_x} = P\rho\Delta S\cos(\theta_1) - \sigma\sin(\alpha) - 12\gamma a_0\sin(\alpha). \quad (2.31)$$

The corresponding equations that reflect the behaviour of the relaxation are given as follows:

1. **In the case of applying F_d and F_i**, the equations are given as follows:
   Since $b = 2y_1$ and $b = a_0 + \Delta = a_0 - 2\delta$, then $\frac{db}{dt} = 2\frac{dy_1}{dt}$, therefore

   $$\frac{d(a_0 - 2\delta)}{dt} = 2(P\rho\Delta S\sin(\theta_1) + \sigma\cos(\alpha) - \sigma),$$

   In the triangle $\triangle FBH$ $\sin(\theta_1) = \frac{x_1}{P}$, and according to (2.15) as well as a_0 is constant, these give

   $$-\frac{d\delta}{dt} = \rho\Delta S(a\sin(\alpha)) + \sigma\cos(\alpha) - \sigma,$$

   By replacing the values of a and α ($a = a_0 + \delta$ and $\alpha = \frac{\pi}{3} + \epsilon$) and using the first order approximation, we have

   $$-\frac{d\delta}{dt} = \rho\Delta S\left((a_0 + \delta)\left(\frac{\sqrt{3}}{2} + \frac{1}{2}\epsilon\right)\right) + \sigma\left(\frac{1}{2} - \frac{\sqrt{3}}{2}\epsilon\right) - \sigma,$$

   Consequently,

   $$\frac{d\delta}{dt} = -\frac{\sqrt{3}}{2}\rho\Delta S\delta - \left(\frac{1}{2}\rho\Delta S a_0 - \frac{\sqrt{3}}{2}\sigma\right)\epsilon. \quad (2.32)$$

   The other terms are neglected because their values are relatively very small. Now, in the triangle $\triangle FBH$ $\cos(\theta_1) = \frac{y_2+y_1}{p}$, and according to (2.16) as well

as using the Equation (2.25), and since $b = 2y_1$, therefore

$$\frac{dx_1}{dt} = \rho\Delta S(a\cos\alpha + b) - \sigma\sin(\alpha).$$

Now, since $\alpha = \frac{\pi}{3} + \epsilon$, $a = a_0 + \delta$ and $b = a_0 + \Delta$ and using the first order approximation and the Equation (2.18), we have

$$\frac{dx_1}{dt} = -\frac{\sqrt{3}}{2}a_0\rho\Delta S\epsilon - \frac{1}{2}\sigma\epsilon - \frac{3}{2}\rho\Delta S\delta. \tag{2.33}$$

The terms that have relatively very small values are neglected.
On the other hand, by using (2.15), then $\frac{dx_1}{dt} = \frac{d(a\sin\alpha)}{dt}$, and therefore

$$\frac{dx_1}{dt} = \sin(\alpha)\frac{da}{dt} + a\cos(\alpha)\frac{d\alpha}{dt}$$

Again, using the same procedure in the previous steps, we have

$$\frac{dx_1}{dt} = \left(\frac{\sqrt{3}}{2} + \frac{1}{2}\epsilon\right)\frac{d\delta}{dt} + (a_0 + \delta)\left(\frac{1}{2} - \frac{\sqrt{3}}{2}\epsilon\right)\frac{d\epsilon}{dt}.$$

In consequence,

$$\frac{dx_1}{dt} = \left(-\frac{3}{4}\rho\Delta S\delta - \frac{\sqrt{3}}{4}\rho\Delta S a_0\epsilon + \frac{3}{4}\sigma\epsilon\right) + \left(\frac{1}{2}a_0 + \frac{1}{2}\delta - \frac{\sqrt{3}}{2}a_0\epsilon\right)\frac{d\epsilon}{dt}. \tag{2.34}$$

Hence, by calling the Equations (2.33) and (2.34), we have

$$-\frac{\sqrt{3}}{2}a_0\rho\Delta S\epsilon - \frac{1}{2}\sigma\epsilon - \frac{3}{2}\rho\Delta S\delta = \left(-\frac{3}{4}\rho\Delta S\delta - \frac{\sqrt{3}}{4}\rho\Delta S a_0\epsilon + \frac{3}{4}\sigma\epsilon\right)$$

$$+\left(\frac{1}{2}a_0 + \frac{1}{2}\delta - \frac{\sqrt{3}}{2}a_0\epsilon\right)\frac{d\epsilon}{dt}.$$

and consequently,

$$\frac{d\epsilon}{dt} = -\frac{3}{2a_0}\rho\Delta S\delta - \left(\frac{\sqrt{3}}{2}\rho\Delta S + \frac{5}{2a_0}\sigma\right)\epsilon. \tag{2.35}$$

The terms with relatively small value are neglected.

In a similar way the equations can be found for the other stages,

2. **In the case of applying F_d and F_p**, the equations are given as follows.

$$\frac{d\delta}{dt} = -\frac{\sqrt{3}}{2}\rho\Delta S\delta - (\frac{1}{2}\rho\Delta S a_0 - 6\sqrt{3}\gamma a_0)\epsilon, \tag{2.36}$$

and

$$\frac{d\epsilon}{dt} = -\frac{3}{2a_0}\rho\Delta S\delta - (\frac{\sqrt{3}}{2}\rho\Delta S + 30\gamma)\epsilon. \tag{2.37}$$

3. **In the case of applying F_d and F_i**, the equations are given as

$$\frac{d\delta}{dt} = -\frac{\sqrt{3}}{2}\rho\Delta S\delta - \left(\frac{1}{2}\rho\Delta S a_0 - \frac{\sqrt{3}}{2}\sigma - 6\sqrt{3}\gamma a_0\right)\epsilon, \tag{2.38}$$

and

$$\frac{d\epsilon}{dt} = -\frac{3}{2a_0}\rho\Delta S\delta - \left(\frac{\sqrt{3}}{2}\rho\Delta S + \frac{5}{2a_0}\sigma + 30\gamma\right)\epsilon. \tag{2.39}$$

The eigenvalues and eigenvectors are used to find the solutions using Matlab $17a$ where $AV = \lambda V$, A is a square matrix, λ is eigenvalue of A corresponding to the eigenvector V. The matrices and each of the eigenvalues and their corresponding eigenvectors are given as follows:

1. **In the stages of the imposing forces F_d and F_i**

$$A = \begin{bmatrix} -0.0433 & 0.0282 \\ -0.1240 & -0.2500 \end{bmatrix}, V = \begin{bmatrix} 0.8349 & -0.1482 \\ -0.5504 & 0.9890 \end{bmatrix},$$

$\lambda_1 = -0.0619$ and $\lambda_2 = -0.2314$.

2. **In the stages of the imposing the forces F_d and F_p**

$$A = \begin{bmatrix} -0.0433 & 0.0289 \\ -0.1240 & -0.2533 \end{bmatrix}, V = \begin{bmatrix} 0.8390 & -0.1493 \\ -0.5441 & 0.9888 \end{bmatrix},$$

$\lambda_1 = -0.0620$ and $\lambda_2 = -0.2346$.

3. **In the stages of the imposing the forces F_d, F_i and F_p**

$$A = \begin{bmatrix} -0.0866 & 0.0567 \\ -0.2549 & -0.5090 \end{bmatrix}, V = \begin{bmatrix} 0.8337 & -0.1457 \\ -0.5521 & 0.9893 \end{bmatrix},$$

$\lambda_1 = -0.1241$ and $\lambda_2 = -0.4714$.

Finally the solutions for the equations are found using the values of the eigenvalues and corresponding eigenvectors.

1. **The solutions in the stages of imposing the forces F_d and F_i**, can be given as

$$\begin{bmatrix} \delta \\ \epsilon \end{bmatrix} = c_1 e^{-0.0619t} \begin{bmatrix} 0.8349 \\ -0.5504 \end{bmatrix} + c_2 e^{-0.2314t} \begin{bmatrix} -0.1482 \\ 0.9890 \end{bmatrix}, \text{ where } c_1, c_2 \text{ are}$$

constants.

2. **In the stages of the imposing the forces F_d and F_p**, the solution can be given as

$$\begin{bmatrix} \delta \\ \epsilon \end{bmatrix} = c_1 e^{-0.0620t} \begin{bmatrix} 0.8390 \\ -0.5441 \end{bmatrix} + c_2 e^{-0.2346t} \begin{bmatrix} -0.1493 \\ 0.9888 \end{bmatrix}, \text{ where } c_1, c_2 \text{ are}$$

constants.

3. **In the stages of the imposing the forces F_d, F_i and F_p**, the solution can be given as

$$\begin{bmatrix} \delta \\ \epsilon \end{bmatrix} = c_1 e^{-0.1241t} \begin{bmatrix} 0.833 \\ -0.5521 \end{bmatrix} + c_2 e^{-0.4714t} \begin{bmatrix} -0.1457 \\ 0.9893 \end{bmatrix}, \text{ where } c_1, c_2 \text{ are}$$

constants.

From the solutions the behaviour of elasticity was observed and from the value of the first eigenvalue in each case it is clear that the relaxation in each of the first two situations is $1/0.0619$ (for second is $1/0.0620$) ≈ 16 and the relaxation for the third situation is $1/0.1241 \approx 8$. These values are consistent to a large extent to those obtained numerically in Subsection (2.4.1). If the time unit in simulation

corresponds to 0.1 s then 8 corresponds to 0.8 s and 16 corresponds to 1.6 s which is close to the experimental data (8).

Finally, the values of the area, in these particular parameters values, at the equilibrium state (i.e. $\frac{dy_2}{dt} = \frac{dy_1}{dt} = \frac{dx_1}{dt} = 0$) can be found as follows:
At the equilibrium state $\frac{dy_2}{dt}$=0, $a = a_0$, and $\alpha = \frac{\pi}{3}$. Hence the Equations (2.23, 2.26 and 2.29) can be rearranged, respectively, as follows:

$$2\rho\Delta S a_0 \sin\left(\frac{\pi}{3}\right) - 2\sigma\cos\left(\frac{\pi}{3}\right) = 0, \tag{2.40}$$

$$2\rho\Delta S a_0 \sin\left(\frac{\pi}{3}\right) - 24\gamma a_0\cos\left(\frac{\pi}{3}\right) = 0, \tag{2.41}$$

and

$$2\rho\Delta S a_0 \sin\left(\frac{\pi}{3}\right) - 2\sigma\cos\left(\frac{\pi}{3}\right) - 24\gamma a_0\cos\left(\frac{\pi}{3}\right) = 0. \tag{2.42}$$

Now, since $\sigma = 0.05$, $\rho = 1$, $\gamma = 0.007$, $\Delta S = 1 - S$, and $S = \frac{3\sqrt{3}}{2}a_0^2$ then the Equations (2.40-2.42) can be reorganised, respectively, as:
in the case of applying the forces F_d and F_i,

$$4.5a_0^3 - \sqrt{3}a_0 + 0.05 = 0, \tag{2.43}$$

in the case of applying the forces F_d and F_p

$$4.5a_0^3 - (\sqrt{3} + 0.084)a_0 = 0, \tag{2.44}$$

and in the case of applying the forces F_d, F_i, and F_p

$$4.5a_0^3 - (\sqrt{3} - 0.084)a_0 + 0.05 = 0 \tag{2.45}$$

Then the Equations (2.43-2.45) can be solved, respectively, for the values of a_0 as follows.
In the case of applying the forces F_d and F_i, $a_0 = 0.6054$ and hence the area at the equilibrium is $S = 0.9523$; in the case of applying the forces F_d and F_p, $a_0 = 0.6052$ and therefore the area at the equilibrium is $S = 0.9515$; in the case of applying the forces F_d, F_i, and F_p, $a_0 = 0.5894$ and hence the area at the equilibrium is $S = 0.9025$. It is noted that the other values of a_0 are neglected either because they

are negative, a_0 represents the length of each edge at the equilibrium and should be positive, or because they render the area close or equal to zero. It can be seen that these area values are approximately the same as found in the simulations.

2.6 Analysis of the dynamics of deformed tissue of infinite size

In this section, the examination of the relaxation for slightly deformed cells is presented analytically. For this examination the symmetrical hexagon shape was taken (Figure 2.17). For simplicity, the centre of the zero cell was chosen to be the origin point. The three parameters a, b and α (2α is the angle $\angle ABC$) are adequate to examine the solutions analytically through finding $\frac{dy_2}{dt}$, $\frac{dx_1}{dt}$, and $\frac{dy_1}{dt}$.

The analytical solutions for the situation in the case of using the forces F_d, F_p and F_i using an infinite number of cells were studied analytically as follows:
Since a symmetrical hexagonal cell shape is given, the analysis of the change of position of the two points A and B are adequate for the objective of this study, where the change of position of the other points that correspond to A and B is similar. (i.e. for example, the points C, D, and F behave similarly to A; E, I, and J behave similarly to B). Therefore the only $\frac{dy_2}{dt}$, $\frac{dx_1}{dt}$, and $\frac{dy_1}{dt}$ are sufficient to describe the behaviour of the relaxation.
Describing these equations requires defining these formulae

$$\boldsymbol{\Psi} = \frac{\boldsymbol{r}_i - \boldsymbol{r}_j}{|\boldsymbol{r}_i - \boldsymbol{r}_j|} + \frac{\boldsymbol{r}_i - \boldsymbol{r}_l}{|\boldsymbol{r}_i - \boldsymbol{r}_l|} + \frac{\boldsymbol{r}_i - \boldsymbol{r}_k}{|\boldsymbol{r}_i - \boldsymbol{r}_k|},$$

and

$$\boldsymbol{\Omega} = \frac{1}{2}(\boldsymbol{r}_l - \boldsymbol{r}_k) \times \boldsymbol{K} + \frac{1}{2}(\boldsymbol{r}_k - \boldsymbol{r}_j) \times \boldsymbol{K} + \frac{1}{2}(\boldsymbol{r}_j - \boldsymbol{r}_l) \times \boldsymbol{K} = \boldsymbol{0}.$$

using Figure 2.2 and the Equations (2.5), (2.9) and (2.12) , where $\boldsymbol{K}$ is the unit vector $(0, 0, 1)$. Hence for the vertex $\boldsymbol{B}$; $\boldsymbol{r}_i = (0, y_2)$, $\boldsymbol{r}_j = (0, y_3)$, $\boldsymbol{r}_l = (-x_1, y_1)$ and $\boldsymbol{r}_k = (x_1, y_1)$, while for the vertex $\boldsymbol{A}$; $\boldsymbol{r}_i = (x_1, y_1)$, $\boldsymbol{r}_j = (x_2, y_2)$, $\boldsymbol{r}_l = (0, y_2)$ and $\boldsymbol{r}_k = (x_1, -y_1)$ and through Equations (2.15) and (2.16) we have

$$\boldsymbol{\Psi_B} = \frac{2(y_2 - y_1)\boldsymbol{j}}{a} - \boldsymbol{j} = (2cos\alpha - 1)\boldsymbol{j}, \tag{2.46}$$

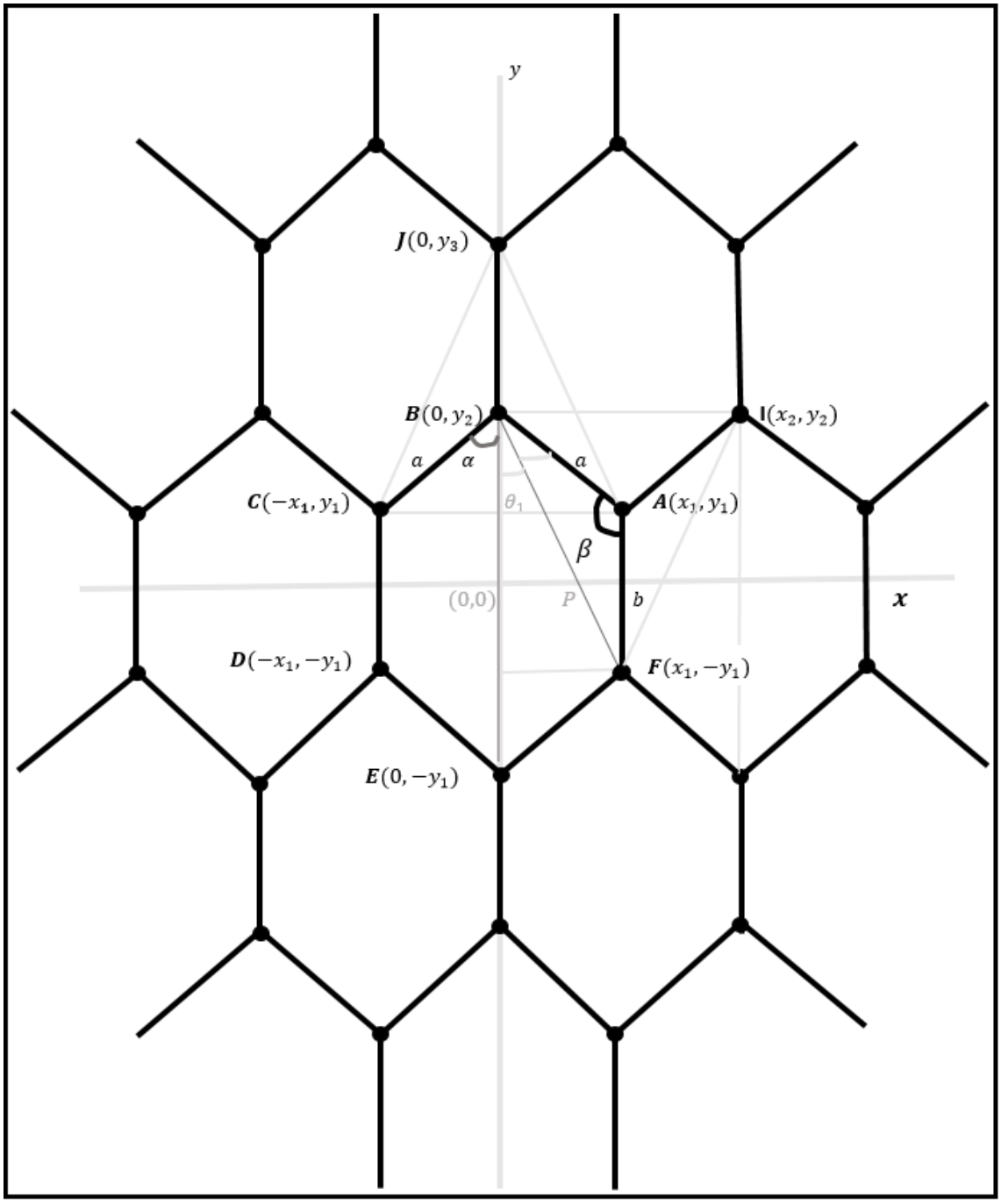

Figure 2.17: A domain of infinite tissue formed by regular hexagonal cells. A particular cell is considered with vertices A, B, C, D, E, F, I, and J and edges AB, BC, CD, DE, EF, FA, AI, and BJ, where $AB = BC = DE = EF = AI = a$, $AF = CD = BJ = b$, and $AC = FD$ (i.e. the shape is symmetric). 2α is $\angle ABC$, θ_1 is $\angle EBF$, and θ_2 is $\angle FBA$.

$$\boldsymbol{\Psi_A} = \frac{2(y_1 - y_2)\boldsymbol{j}}{a} + \frac{2y_1\boldsymbol{j}}{b} = (1 - 2cos\alpha)\boldsymbol{j}, \tag{2.47}$$

and

$$\boldsymbol{\Omega_B} = \boldsymbol{\Omega_A} = \mathbf{0}. \tag{2.48}$$

In this situation, the forces F_d, F_i and F_p are applied and the three relationships $\frac{dy_2}{dt}$, $\frac{dy_1}{dt}$, and $\frac{dx_1}{dt}$ need to be found. From the Equations (2.13a) and (2.13b), and using the point $(0, y_2)$, $F_{iy} = -\sigma\boldsymbol{\Psi_{B(y)}}$ and $F_{d_y} = 0$ and from the Equation (2.13c), $F_{p_y} = -12a_0\gamma\boldsymbol{\Psi_{B(y)}}$. In this case $\frac{dy_2}{dt}$ can be given as

$$\frac{dy_2}{dt} = (\sigma + 24a_0\gamma)(1 - 2cos(\alpha)) \tag{2.49}$$

Moreover, for using the point (x_1, y_1), $F_{i_y} = -\sigma\boldsymbol{\Psi_{A(y)}}$, $F_{i_x} = \mathbf{0}$, $F_{d_y} = -\rho\Delta S\boldsymbol{\Omega_{A(y)}} = \mathbf{0}$, $F_{d_x} = -\rho\Delta S\boldsymbol{\Omega_{A(x)}} = \mathbf{0}$, and $F_{p_y} = -24a_0\gamma\boldsymbol{\Psi_{A(y)}}$ and $F_{p_x} = -24a_0\gamma\boldsymbol{\Psi_{A(x)}} = \mathbf{0}$. In this case $\frac{dx_1}{dt} = 0$ and $\frac{dy_1}{dt}$ can be presented as

$$\frac{dy_1}{dt} = F_{d_y} + F_{iy} + F_{p_y} = (\sigma + 24a_0\gamma)(2cos(\alpha) - 1). \tag{2.50}$$

The equations that represent the behaviour of relaxation can be found as follows:
In the case of applying the forces the equations are given as below.
Since $b = 2y_1$ and $b = a_0 + \Delta = a_0 - 2\delta$, then $\frac{db}{dt} = 2\frac{dy_1}{dt}$, therefore

$$\frac{d(a_0 - 2\delta)}{dt} = 2(\sigma + 24a_0\gamma)(2cos(\alpha) - 1),$$

Since a_0 is constant, therefore by replacing the values of α, $\alpha = \frac{\pi}{3} + \epsilon$, and using the first order approximation, we have

$$-2\frac{d\delta}{dt} = 2(\sigma + 24a_0\gamma)\left(2\left(\frac{1}{2} - \frac{\sqrt{3}}{2}\epsilon\right) - 1\right),$$

Hence,

$$\frac{d\delta}{dt} = \sqrt{3}\sigma\epsilon + 24\sqrt{3}a_0\gamma\epsilon. \tag{2.51}$$

The second and higher order terms are neglected because they are very small.

On the other hand, by using (2.15), then $\frac{dx_1}{dt} = \frac{d(a\sin\alpha)}{dt}$, therefore

$$\frac{dx_1}{dt} = \sin(\alpha)\frac{da}{dt} + a\cos(\alpha)\frac{d\alpha}{dt}$$

By replacing δ and α and using the first order approximation,

$$0 = \left(\frac{\sqrt{3}}{2} + \frac{1}{2}\epsilon\right)\frac{d\delta}{dt} + (a_0 + \delta)\left(\frac{1}{2} - \frac{\sqrt{3}}{2}\epsilon\right)\frac{d\epsilon}{dt}$$

By replacing the value of $\frac{d\delta}{dt}$ using (2.51), then

$$\left(-\frac{3}{2}\sigma\epsilon + 36a_0\gamma\epsilon\right) + \left(\frac{1}{2}a_0 + \frac{1}{2}\delta - \frac{\sqrt{3}}{2}a_0\epsilon\right)\frac{d\epsilon}{dt} = 0. \tag{2.52}$$

In consequence

$$\frac{d\epsilon}{dt} = -\frac{3}{a_0}\sigma\epsilon - 72\gamma\epsilon. \tag{2.53}$$

The relatively small terms value are neglected.

For the solutions, the eigenvalues and eigenvectors are used using Matlab $17a$ where $AV = \lambda V$, A is a square matrix, λ is eigenvalue of A corresponding to the eigenvector V. The matrix and the each of eigenvalues and their corresponding eigenvectors are given as follows:

$$A = \begin{bmatrix} 0 & 0.2583 \\ 0 & -0.7582 \end{bmatrix},\ V = \begin{bmatrix} 1.0000 & -0.3225 \\ 0 & 0.9466 \end{bmatrix},\ \lambda_1 = 0 \text{ and } \lambda_2 = -0.7582$$

Hence, the solutions in the case of the imposing the three forces can be given as

$$\begin{bmatrix} \delta \\ \epsilon \end{bmatrix} = c_1 e^{0t}\begin{bmatrix} 1 \\ 0 \end{bmatrix} + c_2 e^{-0.7582t}\begin{bmatrix} -0.3225 \\ 0.9466 \end{bmatrix}$$

From this solution, it is evident that the relaxation time is infinite.

2.7 Conclusions

In this work the exponential behaviour of the relaxation from these different cases has been confirmed. In the case of one cell and applying the forces after

stretching/shrinking, and then releasing a cell to relax to equilibrium state, it was observed that the relaxation time in the case of applying the three forces decreased in comparison to the case of the absence of the tension force F_i or the perimeter force F_p. This was shown numerically and analytically. In the case of more than one cell, the relaxation adopts exponential behaviour with approximately a linear relationship between the relaxation times and the number of cells only after 36 cells but not before that (Figure 2.13). The case of replacing the tension force F_i with the elastic force F_e was also examined for the behaviour of relaxation. In this case, it was also demonstrated that the relaxation is exponential and the relationship between the relaxation times and the edge target lengths changed from the quadratic behaviour for applying all forces to the bell curve shape in the case of the absence of the perimeter force. Moreover, the relaxation of an infinite number of cells was studied analytically. The results confirmed its elasticity with an infinite relaxation time.

Chapter 3

Mathematical study of epithelial tissue topology

Abstract

Experimental observations reveal the striking identity of topological patterns formed by cells in various epithelial tissues: on apical and basal sides of epithelial tissue cells form polygons, while histograms of cell-edge distribution are practically identical for all inspected tissues. Since tissues form and grow as a result of cellular proliferation, it is reasonable to assume that the events associated with cellular divisions underpin the topology of an entire tissue. A few mathematical models have been reported which derive tissue topology from cellular division patterns (25; 79). However, none of them has succeeded in reproducing experimental observations. Here, two new models are reported, continuous (represented by master equations) and cellular automata, both successfully reproducing experimental and numerical observations and overcoming the shortcomings of previous models. In particular, based on simulations which were performed in this study using the vertex model, it was concluded that the probability of cellular division increases exponentially with the number of cell edges. This assumption turned out to be critical for successful reproduction of experimental data.

3.1 Introduction

With recent advances in biology, particularly with a deeper understanding of cellular processes, it has become possible to tackle new and challenging problems related to the properties of tissues. Epithelial tissues are commonly represented by unicellular layers and have a quite distinctive topology (75). Cell borders, as seen from the tissue surface, form segments of straight lines and cells are represented by polygons (78). The number of cell edges (which is equivalent to the number of their neighbouring cells) commonly varies between 4 and 9, inclusively. Triangular cells, as well as cells with ten or more edges, are encountered very rarely (25).

Histograms showing cellular fractions of polygons having a certain number of edges are widely used in the literature (25; 79). Those histograms have been observed to present a common, almost identical, pattern for the cell-edge distribution (CEDHs) in epithelial tissues of different biological organisms (such as cucumber epidermis (54; 55), *Drosophila*, *Xenopus*, *Hydra*, *Arabidopsis* (25)). The distribution of frequency of cells in respect to their number of edges is asymmetric (see Figure 3.1c), with a maximum value of 6-sided polygons, indicating that the majority of cells in a tissue are hexagonal (45%). Pentagonal and heptagonal cells are observed less frequently in proportions of 25% and 20% respectively while 4 and 8-sided cells are rarely observed with a frequency of less than 5% each.

Figure 3.1c shows CEDHs obtained in three different experiments as follows: Lewis's experimental data (LED) that were observed by Lewis in 1928, Gibson's experimental data (GED) that were monitored by Gibson and his co-worker in 2006, and LaPorta-Zapperi experimental data (LZED) obtained in the University of Milan in work carried out in cooperation with the group in the University of Liverpool (Abdullah and Vasiev) in 2017. The histograms show that there is compatibility between the results. Also in Figure 3.1c, it can be seen that log-normal fits and this observation extends its universality to other objects, for example, to the distribution of sizes of crushed stones in iron mines (50). This universal pattern of histograms gives a significant reference for building a reliable mathematical model. The model in this study was built to primarily provide a mathematical model which is compatible with these experimental observations. CEDH bears a significant role in the understanding of the mechanical approach of the development of the

epithelial tissues and in turn helps to the study and understanding of the other cellular processes, such as adhesion, cell rearrangement and motility.

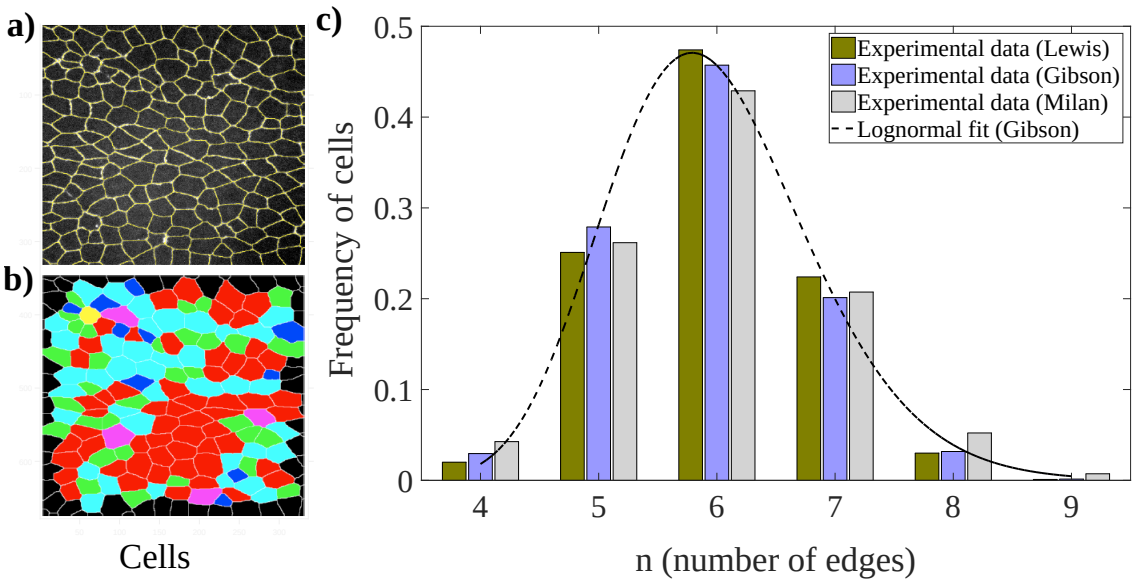

Figure 3.1: a) A segmented image of the tissue formed by a *Drosophila* pupa (9). b) The same image as in (a) is coloured according to the number of edges in each cell (blue:4 ,green:5, red:6, cyan:7, yellow:8), which is belong to LZED. c) The corresponding histogram was averaged over three different experiments and different time steps. The histogram is compared with the earlier results reported in the literature (25; 55).

The polygonal cells that compose an epithelial tissue are portrayed in a two-dimensional surface and are connected to each other by sharing each of their edges with a distinct neighbouring cell. During a single process of division, a cell from the tissue (the mother cell) divides into two new cells (the daughter cells) and each of its two neighbours increases their number of vertices (and therefore their number of edges) by one. The selection of the two affected neighbours is specified by the orientation of a division line that splits the mother cell into two daughter cells. In this concept, the division line crosses two edges of a mother cell rather than any of its vertices. Consequently, in the course of tissue growth, the number of cells as well as their number of edges, changes over time. However, the CEDH stabilizes at an equilibrium pattern shown in Figure 3.1c.

A number of mathematical models have been developed to explain the formation of the observed CEDHs. A model introduced by Gibson et al. (25) (referred to as the GPNP model), considers the cellular proliferation as the only process that

contributes to the topology of epithelial tissue. According to the GPNP model, cells are polygons with four or more sides (i.e. the complete absence of 3-sided cells is assumed) and are divided synchronously in discrete generations, while spatial correlations between the sidedness of neighbouring cells are neglected. The orientation of the division line in each mother cell is chosen randomly. The algorithm of the division process in the GPNP model places two vertices of an i-sided mother cell on one side of the division line, two other vertices on the other side of the division line, and distributes the remaining $i-4$ vertices randomly (following the binomial distribution) between the two sides. These assumptions allow calculations of the probability of an i-sided cell to become j-sided at the next generation, taking into account the change in the sidedness due to the division of the cell and the gain of sides from dividing neighbouring cells. The GPNP model fairly reproduces the histograms obtained experimentally with the only exception that the population of 4-sided cells becomes extinct during proliferation in this model and therefore is not observed in the histograms.

Sandersius et al (79) attempted to revisit the GPNP Markov chain model by considering more biologically realistic assumptions. In their first modification to GPNP model, they considered that 3-sided cells exist in the tissue and they found that under this conjecture, the steady state frequency of 4-sided polygons is 8%. However, despite the fact that this modification predicts a non-zero population of 4-sided cells, in contrast to the original GPNP model, this percentage is two times higher than the actual fraction observed in experimental data. In addition, they analysed the histograms derived by the modified model considering asynchronous divisions and assuming that the split of mother-cell vertices among two daughter cells is given by a uniform random binomial (which was considered in GPNP model) distribution. However, histograms obtained under these assumptions do not reproduce the histogram obtained in experiments and therefore it was concluded that correlations between sidedness of neighbouring cells should play a role in the formation of CEDH in growing tissue. They confirmed their conclusions by showing a good agreement between experimental observations and simulations implemented by a computational sub-cellular element model (79).

One of the core assumptions of all the above models is that the probability of cell

division does not depend on the number of its edges. Recently, it has been shown experimentally that this is not true. Figure 3.2 illustrates that cells with more edges divide more frequently and this relationship can be expressed in an exponential form. The plot in this figure presents the frequency of division as a function of the number of edges of the dividing cell, where the line represents the best exponential fit ($e^{n/\tau}$, $n = 4, 5, ..., 9$) to data with $\tau = 1.7$. This experimental observation reflects the fact that the cells with more edges generally have a larger surface area compared to the cells with a smaller number of edges. This experimental fact has been confirmed, in numerical simulations using the dynamic vertex model. These simulations will be discussed in detail later in this chapter.

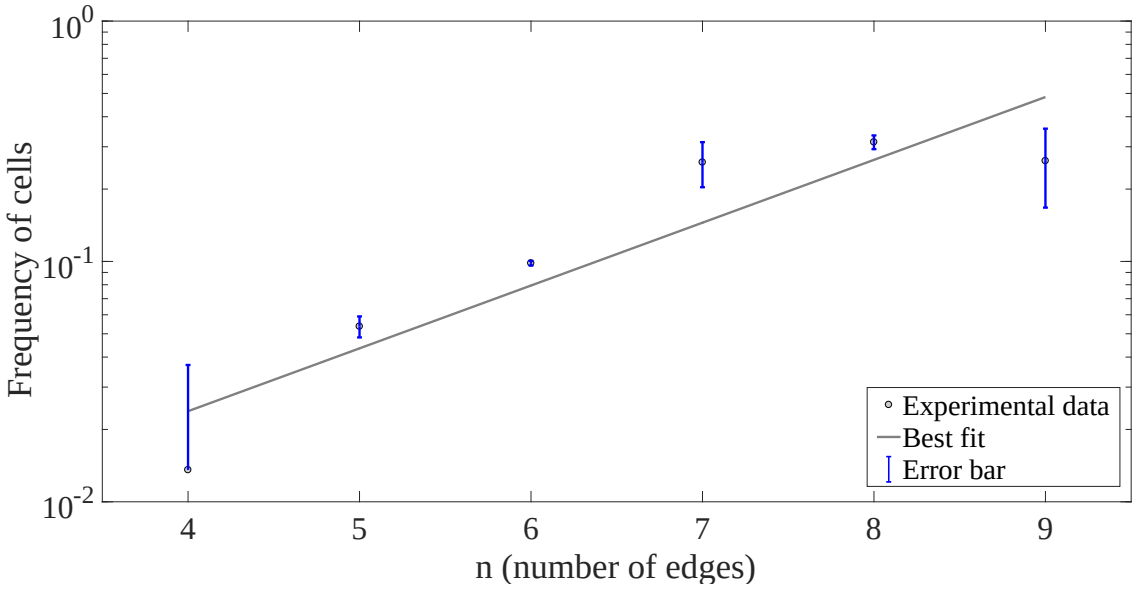

Figure 3.2: Frequency of cellular divisions as depending on the number of edges of dividing cell. The presented data has been extracted from experiments reported in (9). Error bars represent standard deviation and best fit exponential function is shown.

In this study a new mathematical model is proposed which is represented by master equations that describe the evolution of CEDH in growing epithelial tissue. The model is used to assess different cell-division scenarios and associated probability mass functions (such as uniform, binomial or equal split) giving a different distribution of mother-cell vertices between daughter cells. The model is used to produce CEDHs which are then compared with the CEDH obtained in experiments on *Drosophila*. The first version of the model where it was assumed that all cells divide with the same probability (linear model) produced CEDHs which are

considerably different from those obtained in experiments.

In this work, numerical simulations were performed on the vertex dynamics model using the open-access software Chaste (21; 22; 64) to generate CEDH for the virtual tissue. CEDHs obtained in simulations are remarkably similar to the CEDHs from experiments. Particularly, the simulations in this study showed that there might be an exponential increase in the frequency of cellular division with the number of edges of the dividing cell. Such dependence naturally arises from the fact that cells divide only when they reach a certain age and the number of edges of long-living cell tends to increase due to the division of their neighbours. This relationship is used to reformulate the analytical model and to reproduce histograms using the modified model. It was found that the CEDHs in the modified model, had significantly improved and become comparable with the experimental data. In particular, CEDH obtained using the equal split scenario appeared to be in the best agreement with experimentally observed CEDH, while the CEDHs for other scenarios also improved.

Finally, also in this research, a cellular automata model of growing epithelial tissue was developed. CEDHs obtained for a virtual tissue described by this model confirmed results obtained in the framework of the continuous model: CEDHs for the equal split scenario with the incorporated exponential increase of the frequency of cellular division on the sidedness of the dividing cell reproduced the CEDHs fairly well in experiments and in the analytical model under the same assumptions.

3.2 Numerical simulation using the vertex dynamics model

In this section CEDH obtained in numerical simulations of growing tissue using the dynamics vertex model (38) is reported. This model is commonly used for modelling epithelial tissues (20; 22). In this model, each cell is represented by a polygon whose shape can change due to the forces acting upon its vertices. Simulations of the growing tissue were performed using the open-access software Chaste (64), implementing formation of a tissue from a single cell in the course of successive divisions. Cell division in Chaste can be set in various ways. An algorithm when

cell division is set in a random manner was chosen for this study so that the ages of dividing cells are uniformly distributed within the interval $[T_M, T_M + T_R]$, where T_M is a cell age when cells are allowed to divide and T_R randomises the division process (typically $T_M = 2$ and $T_R = 2$). All cells undergo division when they aged between two and four (simulation unit time). The probability of division is uniform function and the Gillespie algorithm is implemented in the vertex dynamics model.Thus, in the simulations, the process of cellular division is fully specified and the number of edges of every single cell (and the number of edges of its neighbours) is easily determined.

3.2.1 CEDH for growing tissue in numerical simulations

To find CEDH in the modelled growing tissue six simulations were performed in this study (since the dispersion for six simulations was not large, there was no reason to make more simulations). Each of these simulations started with one cell (at $t = 0$ as initial condition). In the course of the simulation, cells proliferated and at the time the simulation stopped there were more than 4,000 cells. The simulations data are summarised in the matrix M shown below:

$$M = \begin{bmatrix} 122 & 1625 & 2905 & 1284 & 158 & 8 \\ 111 & 1445 & 2603 & 1132 & 137 & 7 \\ 79 & 1149 & 2176 & 926 & 79 & 1 \\ 70 & 1152 & 2011 & 898 & 86 & 4 \\ 100 & 1347 & 2430 & 1094 & 104 & 3 \\ 110 & 1428 & 2593 & 1165 & 115 & 6 \end{bmatrix}, \quad m = \begin{bmatrix} 6102 \\ 5435 \\ 4410 \\ 4221 \\ 5078 \\ 5417 \end{bmatrix}$$

Entries in the matrix $[M_{ij}]$ represent the number of cells with $j + 3$ number of edges (that is, the number of edges varies between 4, when $j = 1$, and 9, when $j = 6$) at the end of i's simulation. Vector m gives the total number of cells at the end of each simulation, $m_i = \sum_{j=1}^{6} M_{ij}$.

The CEDH obtained from these simulations and shown in Figure 3.3 represents the CEDH for the averaged data for all simulations. To find fractions of cells having

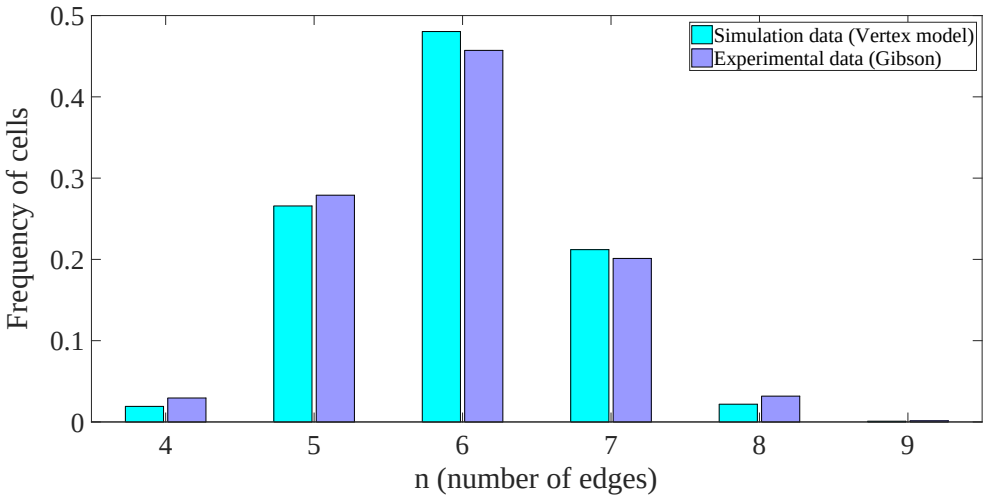

Figure 3.3: CEDH from simulations on vertex model (cyan histograms) as compared with the CEDH obtained experimentally (25) (melrose histograms). Parameter values used in the vertex model simulations: $\rho = 220$, $\sigma = 10$, $\gamma = 10$, $T_M = 2$ and $T_R = 2$.

different number of edges the vector F was used, where F found from the equation

$$F_i = \frac{\sum_{j=1}^{6} M_{ji}}{\sum_{i=1}^{6} m_i}.$$

Hence,

$$F = \Big[0.0192, 0.2658, 0.4803, 0.2120, 0.0218, 0.0009\Big],$$

and components of this (normalised) vector presented as bars forming simulated CEDH in Figure 3.3. As is evident from this figure, the CEDH for growing virtual tissue is remarkably similar to the CEDH obtained experimentally.

If there is no cell division the tissue in the vertex dynamics model is frozen and the histogram of cell-edge distribution is not changing. In order to analyse the dynamic of the histogram, cell division was introduced and while cell grows the histogram evolves and stabilizes when the number of cells over 1000. However, in this study, the simulation was extended to 5000 cells to be sure the stationary histogram is obtained.

3.2.2 Verification of Aboav's Law in numerical simulations

As presented in Chapter 1, Aboav's law defines the relationship between the number of edges of neighbouring cells. In this study, this relationship was calculated for a

virtual tissue formed in the course of one of our numerical simulations for a tissue comprised of 6,102 cells. The results of these calculations are presented in Table 3.1: values of E_{ij} where i and j change from 4 to 9 give the number of j-sided cells neighbouring i-sided cells.

E_{ij}	4	5	6	7	8	9
4	0	11	109	129	34	5
5	19	867	3504	2579	469	27
6	132	3596	8377	4365	585	33
7	146	2644	4396	1613	155	6
8	34	474	586	155	14	1
9	5	27	33	6	1	0

Table 3.1: Numbers of j-sided cells neighbouring i-sided cell (where $i, j = 4, ..., 9$) found in the numerical simulation.

The data presented in the Table 3.1 can be reshaped according to the formula

$$R_{ij} = \frac{E_{ij}}{\sum_{k=4}^{9} E_{ik}},$$

where i, j= $4, ..., 9$ which would now give the fraction of the j-sided cells neighbouring i-sided cells. For example, the cells with 7-sides represent the majority (around 45%) of cells neighbouring 4-sided cells, while the 6-sided comprise only 38%. Similarly, 6- and 5-sided cells represent the majority of cells neighbouring 9-sided cells, forming approximately 46% and 38% of the total number of neighbours respectively. These results are represented by bar plots in Figure 3.4. Aboav's law states that the average number of edges for all cells neighbouring i-sided cell decreases linearly with i. To check this for the numerical simulation in this study, corresponding averages were calculated according to the formula:

$$A_i = \frac{\sum_{j=4}^{9} E_{ij} \times j}{\sum_{j=4}^{9} E_{ij}},$$

where $i = 4, ..., 9$. Calculated numbers can be presented as a vector:

$$A = \Big[6.6979, 6.3608, 6.1038, 5.8890, 5.7184, 5.5972\Big].$$

The plot of these numbers versus i is shown in Figure 3.5 indicates that the simulations confirm Aboav's law: the average number of edges for neighbouring

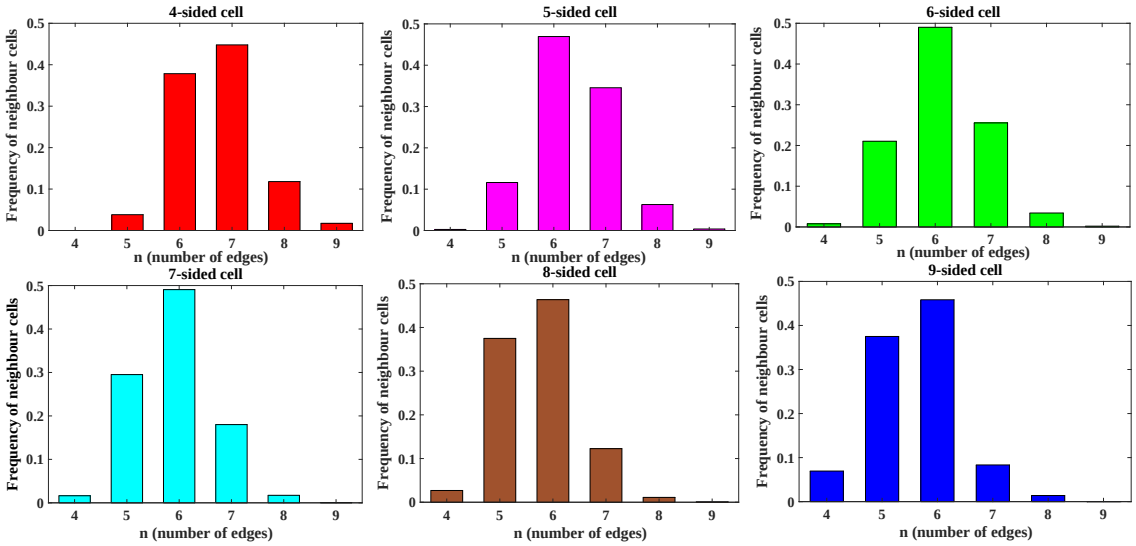

Figure 3.4: Bar charts showing fractions of j-sided cells neighbouring i-sided cells where $i = 4, ..., 9$ (each panel corresponds to one of these i values).

cells indeed decreases linearly with the number of edges of the considered cell.
By eye, the exponential fit looks similar to the linear fit (Figure 3.5), therefore it is not considered.

The data presented in the Table 3.1 can be reshaped according to the formula:

$$R^*_{ij} = R_{ji}$$

which would now give the fraction of the j-sided cells neighbouring i-sided cells. For example, the cells with 6 sides represent around 38%, 47%, 49%, 49%, 46%, and 46% of neighbouring cells to $4, 5, 6, 7, 8, 9$-sided cells respectively. The data represented by R^*_{ij} are presented as bar charts in Figure 3.6. It can be seen that cells with more edges are more frequently met as neighbours of cells with smaller number of edges, and vice versa.
It is noted that the values that can be calculated using the Equation (1.19), vector m which represents the average number of edges surrounding a cell, are approximately the same as in the vector A.

$$m = \Big[6.7680, 6.3744, 6.1120, 5.9246, 5.7840, 5.6747\Big] .$$

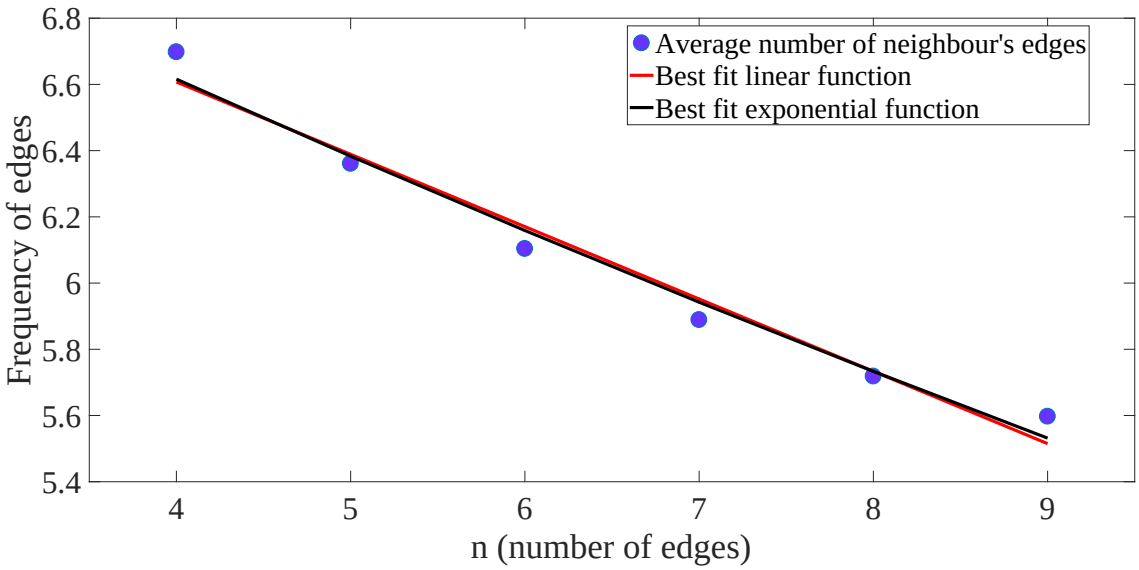

Figure 3.5: Aboav relationship for the virtual tissue obtained in numerical simulation using the vertex model: average number of edges for cells neighbouring i-sided cell linearly decreases with an increase of i.

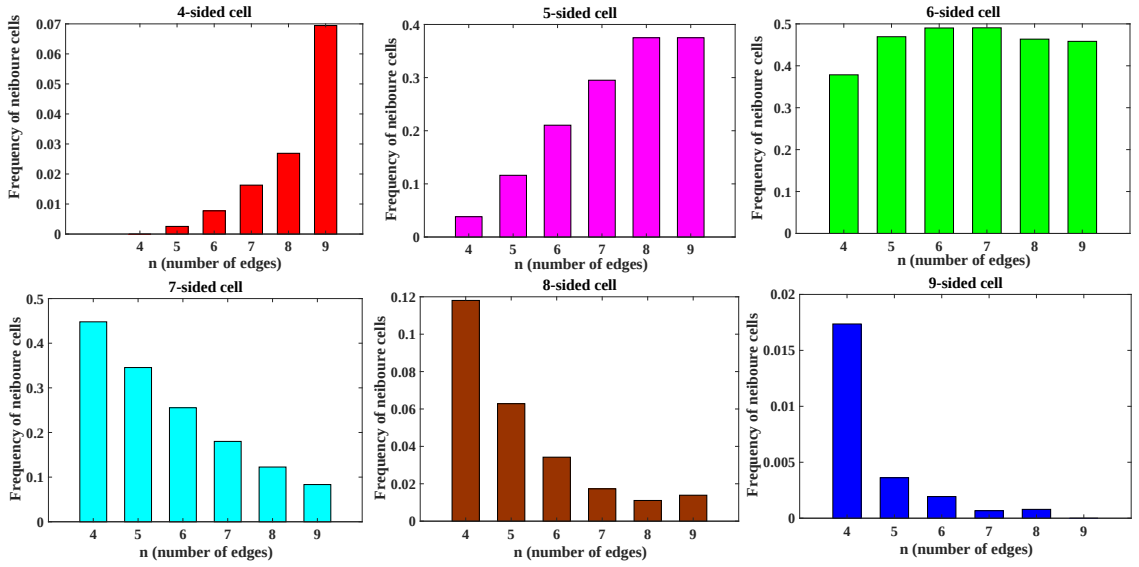

Figure 3.6: Frequencies of j-sided cells (bars) neighbouring i-sides cells (panels).

3.2.3 Dependence of the frequency of cellular division on the number of edges of dividing cell

As seen earlier, the experimental observations indicate that cells having more edges divide more frequently than the cells that have a smaller number of edges. This phenomenon was examined in this study for virtual tissues obtained in six numerical simulations which were used to find CEDH (see above). Similarly to the matrix M introduced for constructing CEDH, matrix L was shaped so that its entries $[L_{ij}]$ give the total number of j-sided cells divided during the i's-simulation.

$$L = \begin{bmatrix} 6 & 286 & 1916 & 3082 & 747 & 62 \\ 8 & 299 & 1779 & 2578 & 713 & 57 \\ 7 & 219 & 1452 & 2138 & 549 & 43 \\ 3 & 233 & 1394 & 2079 & 484 & 26 \\ 9 & 277 & 1662 & 2428 & 649 & 51 \\ 7 & 272 & 1777 & 2594 & 708 & 58 \end{bmatrix}.$$

Using matrices M and L matrix R can be constructed with $R_{ij} = \frac{L_{ij}}{M_{ij}}$ which gives the number of divisions of j-sided cells per one j-sided cell

$$R = \begin{bmatrix} 0.0492 & 0.176 & 0.6596 & 2.4003 & 4.7278 & 7.75 \\ 0.0721 & 0.2069 & 0.6834 & 2.2774 & 5.2044 & 8.1429 \\ 0.0886 & 0.1906 & 0.6673 & 2.3089 & 6.9494 & 43 \\ 0.0429 & 0.2023 & 0.6932 & 2.3151 & 5.6279 & 6.5 \\ 0.09 & 0.2056 & 0.684 & 2.2194 & 6.2404 & 17 \\ 0.0636 & 0.1905 & 0.6853 & 2.2266 & 6.1565 & 9.6667 \end{bmatrix}.$$

Finally, after averaging entries in each column and normalising the obtained set of numbers so that their sum is equal to one, the vector σ is found as

$$\sigma = \Big[0.0028, 0.008, 0.0278, 0.0939, 0.2385, 0.629\Big],$$

with entries σ_i giving the division frequencies of i-sided cells. Plot of σ_i versus i is shown in Figure 3.7. It can be seen that once again the exponential increase in the probability of division versus the number of edges of the dividing cell is present,

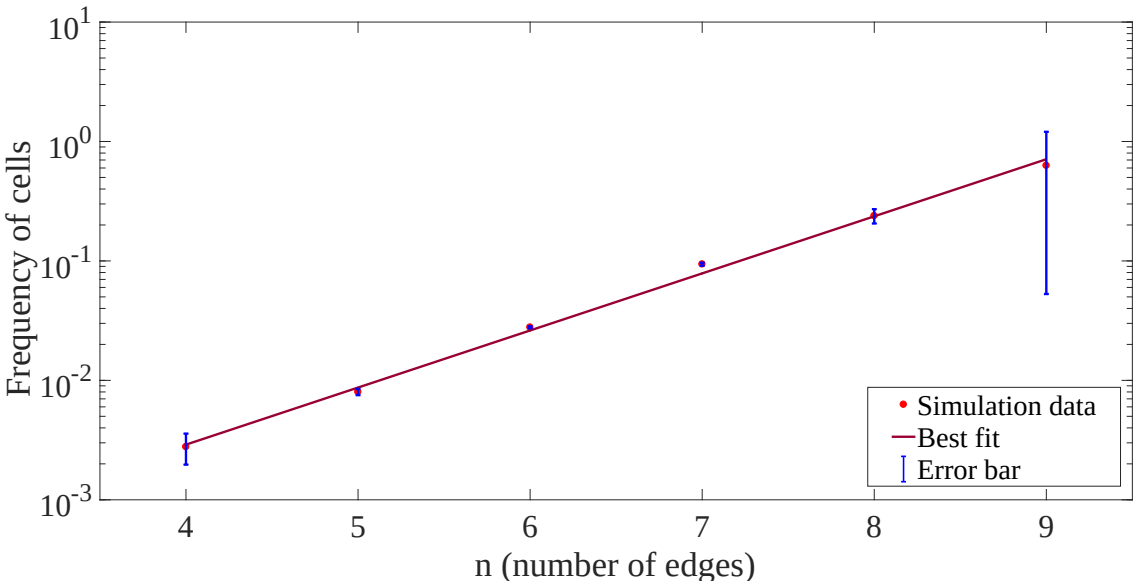

Figure 3.7: Correlation between the frequency of cell division and the number of edges i of mother cell in numerical simulations on the vertex model. Error bars represent standard deviation and best fit exponential function is shown.

as observed in experiments (see Figure 3.2). The exponential fit ($e^{t/\tau}$) to the data shown in Figure 3.7 is the best for the value of the parameter $\tau = 0.91$.

The most important observation that can be figured out is, as the Sigma′s values give the proportional relationship between the number of edges in a cell and the opportunity of this cell to be divided faster than the other cells , the Aboave relationship illustrates that the cells with the same number of edges i have neighbours with an average number of edges and this average decrease with increasing i and this provides the opportunity to the cells with the small number of edges to grow and become bigger pertaining to the size. Consequently, these two relationships play the central role in the continuing the process of the division that the epithelial tissues are required.

3.3 Analytical model describing the evolution of CEDH in epithelial tissue

In this section, a system of master equations is introduced which describes the evolution of cellular fractions in growing epithelial tissue. The principal assumption is that cellular division is a reasonably rare event so that cell-shape

changes associated with any two cellular divisions do not interfere with each other. Furthermore, it is assumed here that there are no 3-sided cells, which leads to the assumption that a cleavage line crosses two non-adjacent edges of a mother cell (this assures that none of the daughter cells is 3-sided, neither is formation of cells with more than nine neighbours considered, as those are not commonly observed in experiments (25)). The order of cell vertices plays a fundamental role in determining the orientation of a division line.

It is assumed that the proliferation is the only process involved in the evolution of CEDH. It is noted (see Figure 3.8) that each cell division results in the formation of two daughter cells with their number of edges totalling to $i + 4$ where i is the number of edges of the mother cell. In addition, two neighbours of the dividing cell each acquire an extra edge. Note that as a result of single cell division, there appears one extra cell and six extra edges, leading, in the long run, to an average six edges per cell, making an average cell to be hexagonal.

The total number of cells at time t is denoted by $N(t)$, the number of i-sided cells

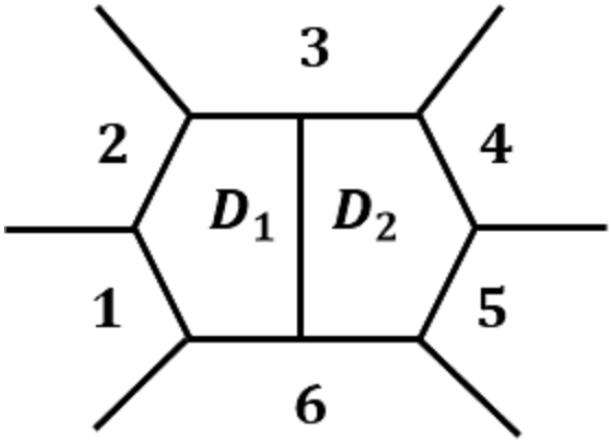

Figure 3.8: Division of hexagonal cell into two identical daughter cells.

by $N_i(t)$ and the fraction of i-sided cells in the population by $p_i(t) = N_i(t)/N(t)$. The rate of change in the fraction of i-sided cells is given by

$$\frac{d}{dt}\left(\frac{N_i}{N}\right) = \frac{dN_i N - N_i dN}{N^2 dt} = \frac{dN}{Ndt}\left(\frac{dN_i}{dN} - \frac{N_i}{N}\right),$$

which can be written as

$$\dot{p_i} = \alpha\left(M_i + K_i - p_i\right), \tag{3.1}$$

where $\alpha = \frac{dN}{Ndt}$ is the cells' proliferation rate and the expression in brackets defines

the probability for an i-sided cell to appear/disappear in a single proliferation event. $\frac{dN_i}{dN} = M_i + K_i$ is split into two terms, where M_i determines the changes due to removal of i-sided mother cells and the addition of i-sided daughter cells while K_i accounts for the changes in the number of edges of neighboring cells after each division. The term K_i is easy to estimate, assuming that the fraction of i-sided cells in the neighborhood of any dividing cell is equal to their total fraction (i.e. there is no correlation between sidedness of neighbouring cells). Then:

$$K_i = -2p_i + 2p_{i-1}, \tag{3.2}$$

where the first term defines the decrease in the fraction of i-sided cells if either or both affected neighbours were i-sided before the division and become $i+1$-sided after the division; and the second term counts the cells that were $i-1$-sided before the division and become i-sided. If the number of edges is allowed to vary from four to nine, then Equation (3.2) holds for $5 < i < 8$, while for the boundary cases $K_4 = -2p_4$ and $K_9 = 2p_8$.

3.3.1 Three scenarios of cellular division

To assess the component M_i in Equation (3.1) different scenarios of cellular division will be considered in this study. In the first scenario, the division line crosses any two non-adjacent edges of the mother cell with equal probability. This scenario is referred to as 'uniformly oriented divisions'. This case is shown schematically in the upper panel of Figure 3.9 where the black dashed and red solid lines represent the possible division lines all occurring with the same probability which is equal to $1/(i-3)$ where i is the number of edges of the mother cell. This also gives the frequencies of possible pairs of daughter cells which are shown in the lower panel of Figure (3.9). Thus, for example, the frequency of acquiring a 4-sided daughter cell from a hexagonal, heptagonal, or octagonal mother cell is $2:3$, $2:4$ and $2:5$ respectively. The general form of M_i under this scenario is given by:

$$M_i = 2\sum_{j=i}^{9} \frac{1}{j-3} p_j^* - p_i^*, \tag{3.3}$$

where p_j^* is the probability that a mother cell, in a randomly chosen division, is i-sided.

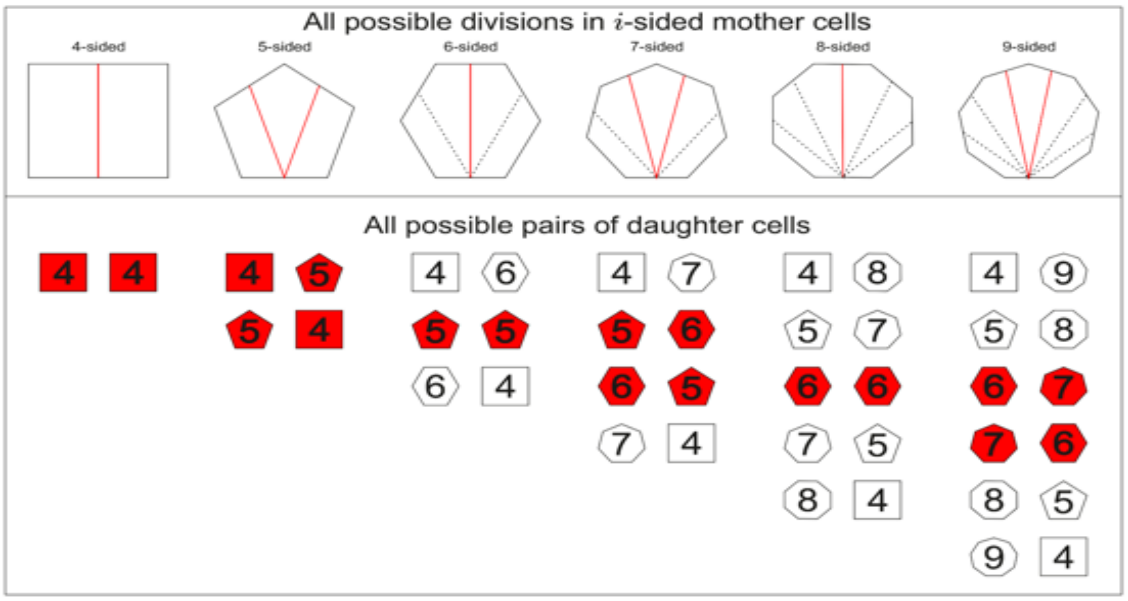

Figure 3.9: Possible division scenarios of i-sided mother cells and corresponding sidedness of daughter cells. The red lines in the upper panel and the red coloured pairs of daughter cells at the lower panel correspond to the 'equal split' scenario.

In an alternative scenario, the probabilities for different orientations of a division line is non-uniform and given by a binomial probability. In this case the division line that connects two edges that are furthest away from each other (red solid lines in upper panel of Figure 3.9) appears more frequently than a division line that connects edges which are closest to each other (black dashed lines in upper panel of Figure 3.9). In this case, the pairs of daughters that are shown by red in the lower panel of Figure 3.9 are observed more frequently than the uncoloured pairs. The M_i under this scenario, referred to as 'binomially oriented divisions', is given by

$$M_i = 2\sum_{j=i}^{9} \binom{j-4}{i-4} \frac{1}{2^{(j-4)}} p_j^* - p_i^*, \tag{3.4}$$

In the third scenario the division line connects only two opposing edges of the mother cell, so that the daughter cells either have an equal number of edges (the mother cell has an even number of edges) or these numbers differ by one (mother cell with odd number of edges). Allowed divisions are illustrated in red in the upper panel of Figure 3.9 and possible pairs of daughter cells in red in the lower panel of Figure 3.9.

It is clear that i-sided daughter cells can only appear after the division of $(2i-3)$, $(2i-4)$ or $(2i-5)$-sided cells. Then, the term M_i can be represented as:

$$M_i = \begin{cases} 2p^*_{2i-4} + p^*_{2i-3} - p^*_i & \text{if } i = 4 \\ p^*_{2i-5} + 2p^*_{2i-4} + p^*_{2i-3} - p^*_i & \text{if } 4 < i < 7 \\ p^*_{2i-5} - p^*_i & \text{if } i = 7 \\ -p^*_i & \text{if } i > 7. \end{cases} \tag{3.5}$$

3.3.2 Linear model

If, following (25), it is assumed that all cells divide with equal probability, i.e. $p^*_i = p_i$, then for each of the considered above scenarios there will be a system of linear equations (Equations (3.1-3.3) for the first scenario, (3.1, 3.2, 3.4) - for the second and (3.1, 3.2, 3.5) - for the third), satisfying the condition $\sum_{i=4}^{9} \dot{p}_i = 0$ and describing the evolution of CEDH. Matrices defining the system in each of these three cases are as follows:

$$\text{Uniform distribution: } \begin{bmatrix} \dot{p_4} \\ \dot{p_5} \\ \dot{p_6} \\ \dot{p_7} \\ \dot{p_8} \\ \dot{p_9} \end{bmatrix} = \begin{bmatrix} -2 & 1 & \frac{2}{3} & \frac{2}{4} & \frac{2}{5} & \frac{2}{6} \\ 2 & -3 & \frac{2}{3} & \frac{2}{4} & \frac{2}{5} & \frac{2}{6} \\ 0 & 2 & -\frac{10}{3} & \frac{2}{4} & \frac{2}{5} & \frac{2}{6} \\ 0 & 0 & 2 & -\frac{14}{4} & \frac{2}{5} & \frac{2}{6} \\ 0 & 0 & 0 & 2 & -\frac{18}{5} & \frac{2}{6} \\ 0 & 0 & 0 & 0 & 2 & -\frac{10}{6} \end{bmatrix} \begin{bmatrix} p_4 \\ p_5 \\ p_6 \\ p_7 \\ p_8 \\ p_9 \end{bmatrix},$$

$$\text{Binomial distribution: } \begin{bmatrix} \dot{p_4} \\ \dot{p_5} \\ \dot{p_6} \\ \dot{p_7} \\ \dot{p_8} \\ \dot{p_9} \end{bmatrix} = \begin{bmatrix} -2 & 1 & \frac{2}{4} & \frac{2}{8} & \frac{2}{16} & \frac{2}{32} \\ 2 & -3 & 1 & \frac{6}{8} & \frac{8}{16} & \frac{10}{32} \\ 0 & 2 & -\frac{14}{4} & \frac{6}{8} & \frac{12}{16} & \frac{20}{32} \\ 0 & 0 & 2 & -\frac{30}{8} & \frac{8}{16} & \frac{20}{32} \\ 0 & 0 & 0 & 2 & -\frac{62}{16} & \frac{10}{32} \\ 0 & 0 & 0 & 0 & 2 & -\frac{62}{32} \end{bmatrix} \begin{bmatrix} p_4 \\ p_5 \\ p_6 \\ p_7 \\ p_8 \\ p_9 \end{bmatrix},$$

$$\text{Equal split: } \begin{bmatrix} \dot{p_4} \\ \dot{p_5} \\ \dot{p_6} \\ \dot{p_7} \\ \dot{p_8} \\ \dot{p_9} \end{bmatrix} = \begin{bmatrix} -2 & 1 & 0 & 0 & 0 & 0 \\ 2 & -3 & 2 & 1 & 0 & 0 \\ 0 & 2 & -4 & 1 & 2 & 1 \\ 0 & 0 & 2 & -4 & 0 & 1 \\ 0 & 0 & 0 & 2 & -4 & 0 \\ 0 & 0 & 0 & 0 & 2 & -2 \end{bmatrix} \begin{bmatrix} p_4 \\ p_5 \\ p_6 \\ p_7 \\ p_8 \\ p_9 \end{bmatrix}.$$

Solutions of these systems are given by a superposition of exponents defined by eigensolution of the corresponding matrices.

The characteristic equation for the first matrix, corresponding to the uniform distribution for the orientation of the cell-division line:

$$\lambda^6 + \frac{171\lambda^5}{10} + \frac{5146\lambda^4}{45} + \frac{33391\lambda^3}{90} + \frac{25954\lambda^2}{45} + 336\lambda = 0 \tag{3.6}$$

The characteristic equation for the binomial distribution:

$$\lambda^6 + \frac{289\lambda^5}{16} + \frac{16251\lambda^4}{128} + \frac{219597\lambda^3}{512} + \frac{699143\lambda^2}{1024} + \frac{405253\lambda}{1024} = 0 \tag{3.7}$$

Finally, the characteristic equation fo the equal split scenario:

$$\lambda^6 + 19\lambda^5 + 140\lambda^4 + 490\lambda^3 + 792\lambda^2 + 456\lambda = 0 \tag{3.8}$$

Eigenvalues (or roots of characteristic Equations (3.6, 3.7, 3.8)) are found (using Matlab) to be as following:

$$\lambda_{UO} = \begin{bmatrix} 0 \\ -4.1672 + 0.2184i \\ -4.1672 - 0.2184i \\ -4 \\ -3.3067 \\ -1.4588 \end{bmatrix}, \lambda_{BO} = \begin{bmatrix} 0 \\ -4.4692 + 0.7864i \\ -4.4692 - 0.7864i \\ -4.7573 \\ -3.0362 \\ -1.3305 \end{bmatrix}, \lambda_{ES} = \begin{bmatrix} 0 \\ -5.1573 + 1.3052i \\ -5.1573 - 1.3052i \\ -4.7321 \\ -2.6854 \\ -1.2679 \end{bmatrix}.$$

where λ_{UO}, λ_{BO} and λ_{ES} refer to the matrices of eigenvectors of the uniformly oriented cell-division, Binomially oriented cell-division and Equal split cell-division, respectively.

Therefore, the matrix of eigenvectors corresponding to λ_{UO} along columns is

$$EVe_{UO} = \begin{bmatrix} -0.5725 & -0.0095 - 0.0024i & -0.0095 + 0.0024i & 0.0108 & -0.0517 & -0.3404 \\ -0.5725 & -0.0095 - 0.0024i & -0.0095 + 0.0024i & 0.0217 & -0.0517 & -0.3404 \\ -0.4294 & -0.0235 - 0.0350i & -0.0235 + 0.0350i & 0.0325 & 0.0229 & -0.2064 \\ -0.2863 & -0.1169 + 0.0933i & -0.1169 - 0.0933i & 0.0433 & 0.2159 & -0.0469 \\ -0.1789 & 0.7725 & 0.7725 & -0.7579 & 0.6172 & 0.0879 \\ -0.2147 & -0.6132 - 0.0536i & -0.6132 + 0.0536i & 0.6496 & -0.7527 & 0.8460 \end{bmatrix},$$

The matrix of eigenvectors corresponding to λ_{BO} along columns can be given as

$$EVe_{BO} = \begin{bmatrix} 0.4816 & 0.0078 - 0.0124i & 0.0078 + 0.0124i & -0.0139 & 0.2218 & -0.5354 \\ 0.6092 & -0.0313 + 0.0477i & -0.0313 - 0.0477i & 0.0906 & -0.0267 & -0.4279 \\ 0.4852 & 0.0937 + 0.1156i & 0.0937 - 0.1156i & -0.1076 & -0.2452 & -0.0747 \\ 0.3125 & 0.1363 - 0.3162i & 0.1363 + 0.3162i & 0.2575 & -0.3028 & 0.1556 \\ 0.1759 & -0.7385 & -0.7385 & -0.7797 & -0.4302 & 0.2054 \\ 0.1816 & 0.5321 + 0.1653i & 0.5321 - 0.1653i & 0.5530 & 0.7831 & 0.6770 \end{bmatrix},$$

And the matrix of eigenvectors corresponding to λ_{ES} along columns can be given as

$$EVe_{ES} = \begin{bmatrix} 0.3409 & 0.0395 - 0.0372i & 0.0395 + 0.0372i & -0.1506 & -0.6264 & 0.4546 \\ 0.6818 & -0.0763 + 0.1690i & -0.0763 - 0.1690i & 0.4113 & -0.4585 & -0.3116 \\ 0.5303 & 0.1103 - 0.3954i & 0.1103 + 0.3954i & -0.3244 & 0.0969 & -0.4291 \\ 0.3030 & -0.3556 + 0.4010i & -0.3556 - 0.4010i & 0.2375 & 0.2647 & -0.1491 \\ 0.1515 & 0.6145 & 0.6145 & -0.6488 & 0.1938 & -0.2269 \\ 0.1515 & -0.3324 - 0.1374i & -0.3324 + 0.1374i & 0.4750 & 0.5295 & 0.6621 \end{bmatrix}.$$

It can be seen that for each of the three models all eigenvalues except for one have negative real part, none have positive real part and one has zero real part. Thus, solutions of these systems will converge to the stationary solution defined by the eigenvector corresponding to zero eigenvalue. As the sum of all fractions in the CEDH is equal to one, the stationary solution will correspond to this eigenvalue, normalized in a way that the sum of all its components is equal to one. The normalized eigenvector corresponding to the eigenvalue $\lambda = 0$ for the three scenarios are

$$NEVCZ_{UO} = \begin{bmatrix} 0.2540 \\ 0.2540 \\ 0.1905 \\ 0.1270 \\ 0.0794 \\ 0.0952 \end{bmatrix} ; \quad NEVCZ_{BO} = \begin{bmatrix} 0.2144 \\ 0.2712 \\ 0.2160 \\ 0.1391 \\ 0.0783 \\ 0.0809 \end{bmatrix} ; \quad NEVCZ_{ES} = \begin{bmatrix} 0.1579 \\ 0.3158 \\ 0.2456 \\ 0.1404 \\ 0.0702 \\ 0.0702 \end{bmatrix}.$$

The stationary solutions of all three linear systems as given by these three normalised

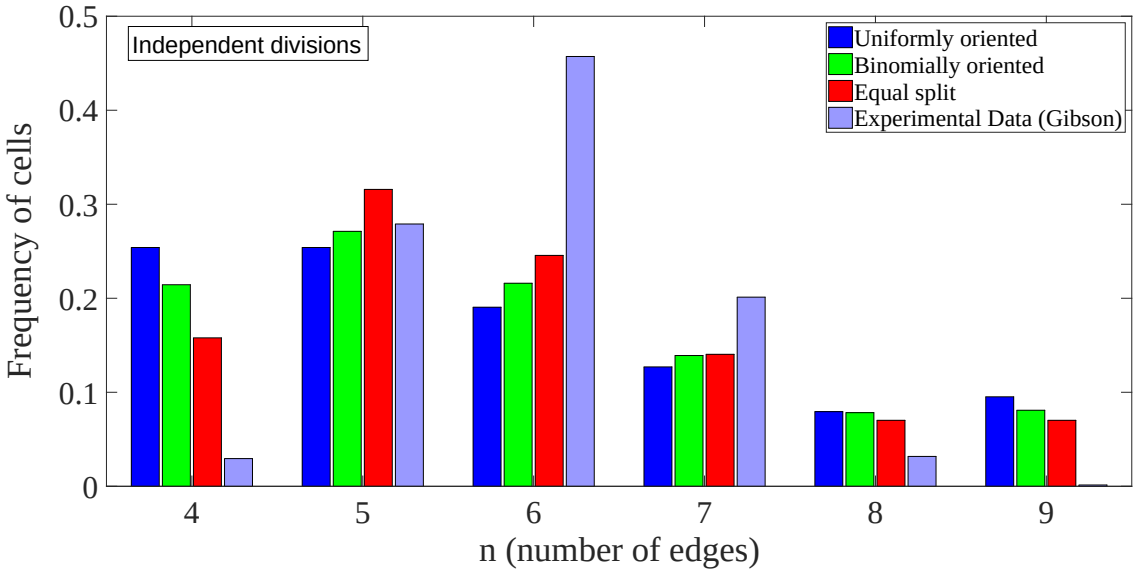

Figure 3.10: CEDHs obtained in three versions (differing on probabilities of different division scenarios) of linear model as compared with the experimental CEDH. The Matlab codes are presented in Appendix A.3.

eigenvectors represent modelled CEDHs so that the fractions of i-sided cells are given by the associated components of eigenvectors. These modelled CEDHs are shown in Figure 3.10 which also includes the CEDH from experiments. As seen from this figure, the modelled CEDHs do not reproduce the experimental observations in a satisfactory manner; the differences between the experimental results and the modelled histograms are clearly seen. For example, the cellular fraction of hexagonal cells is around 45% in the experimental observations while it does not exceed 25% for all three modelled scenarios.

3.3.3 Nonlinear model

The assumption that the frequency of cellular division is independent of the sidedness of dividing cell is not supported by experiments (55). Besides, in this study, it was

shown numerically using the dynamics vertex model that the division probability increases exponentially with the number of edges of the dividing cell (see Figure 3.7). A model was thus modified assuming that in Equations (3.3, 3.4, and 3.5) the values of p_i^* are found using the results of the numerical simulations as given by σ_i and shown in Figures 3.2 and 3.7. p_i^* is the fraction of $i-$sided mother cell and the relationship between p_i^* and p_i was found numerically in the vertex dynamics model and expressed by

$$p_i^* = \frac{\sigma_i p_i}{\sum_i \sigma_i p_i}, \tag{3.9}$$

and this term renders the models non-linear. Solutions of these non-linear models

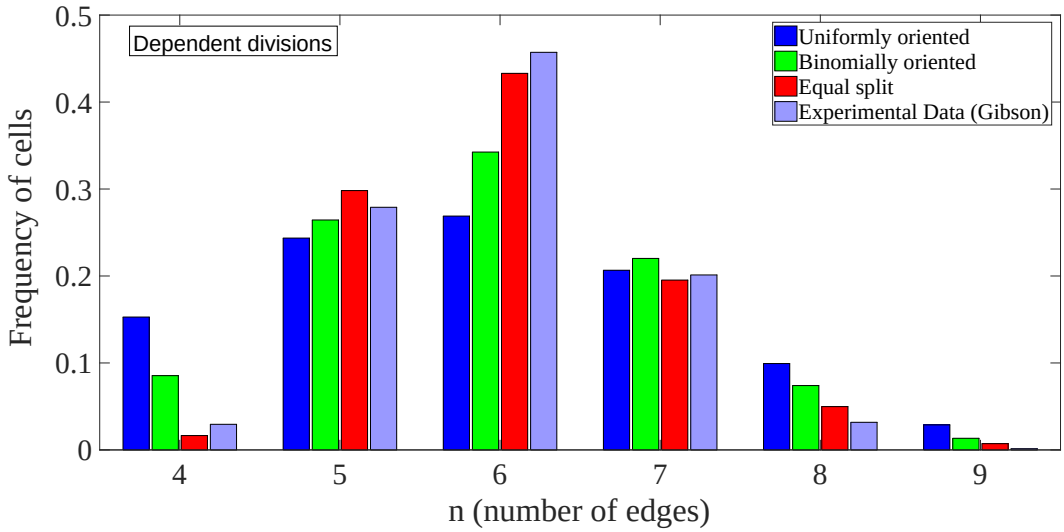

Figure 3.11: CEDHs obtained in the versions of analytical model with included dependence of the frequency of cellular division on the sidedness of dividing cell (as suggested by Figure 3.7). The model becomes non-linear and solutions are found numerically using Matlab codes. The Matlab codes are given in Appendix A.3

cannot be found analytically but can be evaluated numerically. A code was written in Matlab to find solutions for all three versions of the model. It was found that the solutions converge in all cases and show the obtained stationary solutions in Figure 3.11. As seen from this figure, the modelled CEDHs in the case of non-linear models are far closer to the experimentally observed CEDH. The best fit is given by the Equal split model: in fact, the steady-state solution for this model is in excellent agreement with the experimental observations and also with simulation results (Figure 3.12). The histograms obtained in the cases of the two other cell-division scenarios were also improved and now appear comparable with the experimental

data, especially in the case of the binomial distribution.

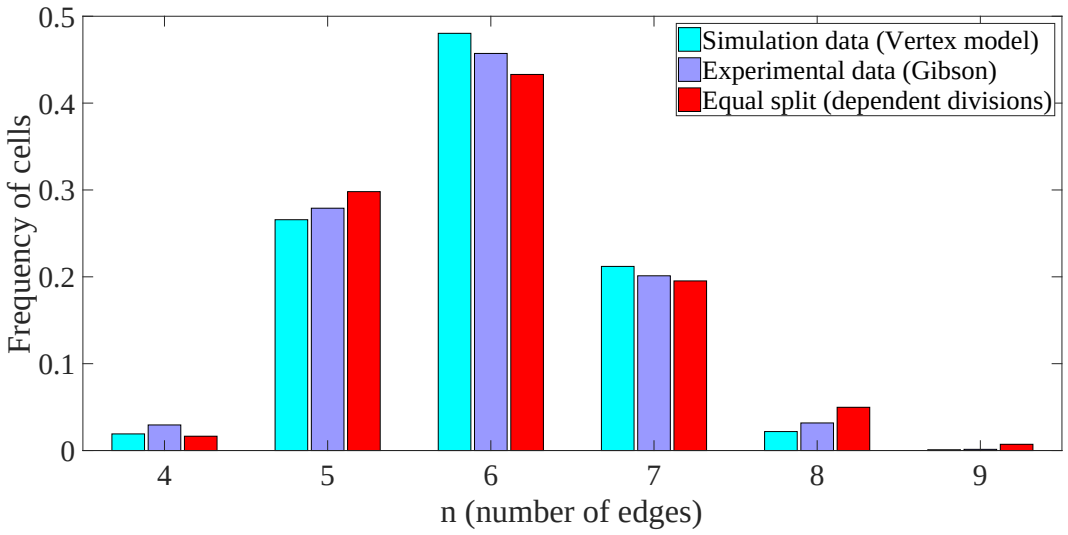

Figure 3.12: CEDHs obtained in the versions of analytical model with included dependence of the frequency of cellular division on the sidedness of dividing cell in comparison with the CEDHs that obtained by experimental observations and by simulation results.

3.4 Cellular automata model

To verify the finding which was obtained using the analytical model (as represented by the master equations) and using the dynamic vertex model (as implemented by Chaste), yet another model was designed. This is a cellular automata model where the tissue growth and the associated evolution of CEDH are given by a set of automata rules. In this model, a number of cells represented by polygons were considered so that each cell is associated with an integer number between 4 and 9 representing their number of edges.

To begin with, a small set (can be one) of numbers between 4 and 9 was randomly chosen representing a cell in the virtual tissue. At each time step, a single cell-division event was implemented in the following manner: A number was selected randomly from the existing set and replaced by two other numbers calculated according to the scenario that the original number corresponds to the number of edges of the mother cell and two new numbers to the number of edges of two daughter cells according to the Equal split scenario as in Figure 3.9. Furthermore, at the same time step, two other cells were chosen randomly from the population

to be considered as the neighbours of the divided cell for adding an extra edge to each one. To avoid a formation of 10-sided cells, a constraint was put that 9-sided cells were not permitted to be selected as a neighbour of the dividing cell. The cell-division process was repeated many times and the forming CEDH was examined. Calculations were stopped when CEDH stabilised at an equilibrium distribution (it took a few thousand divisions).

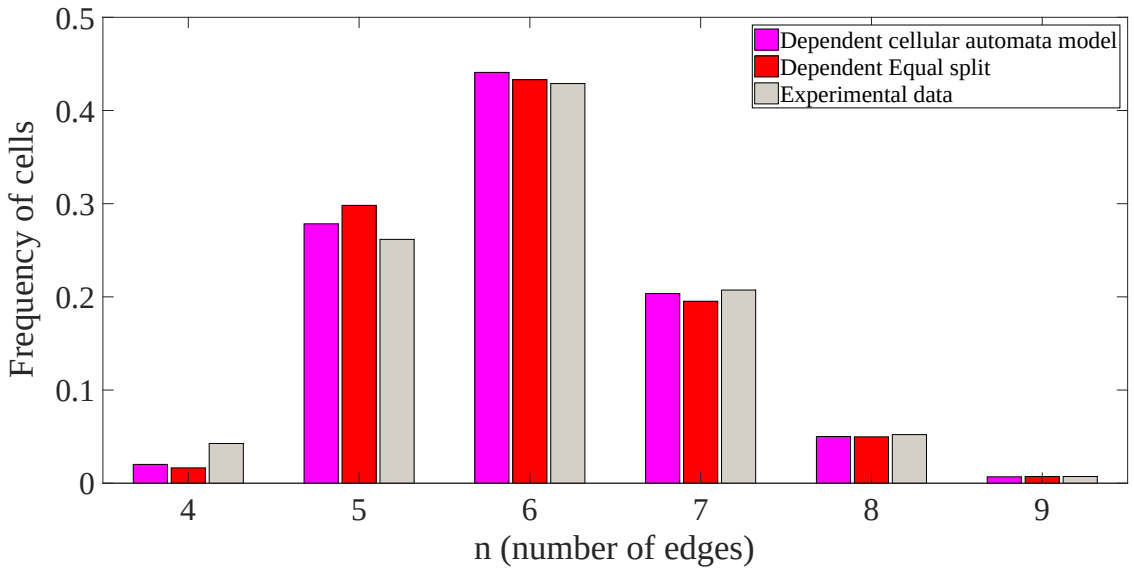

Figure 3.13: Histograms of theoretical cell-edge distribution. The histograms (magenta bars) were derived using a code for an automata model based on the equal split process in comparison to the dependent equal split (red bars) and LZED (light gray bars). The Matlab code is presented in Appendix A.4.

Simulations using the cellular automata model were implemented through the Matlab programming language. The simulations typically started with 100 cells of random sidedness and run for 100,000 iterations. At each iteration step a randomly chosen cell divided. To incorporate dependence of the frequency of cellular division on the number of edges of a dividing cell, the division with a probability given by the exponent $4 \times 10^{-5} e^{(1.1004i)}$, $i = 4, ..., 9$ was allowed that had been estimated on the basis of numerical simulations (see Figure 3.7). As noted earlier, the cell division events followed an equal split scenario. That is, if the mother cell has an even number of edges i, then each of the daughters will have $(i+4)/2$ of edges. However, if the mother cell has an odd number of edges i, then one of the daughters will have $(i+5)/2$ edges and the other daughter will have $(i+3)/2$ edges.The cell division event necessitated a random selection of two other cells whose sidedness is less than

9 (to represent the neighbours of the dividing cell), adding an extra edge to each of them. At the end of each iteration, one mother cell disappears, two daughter cells appear and two other cells receive an extra edge. Finally, the number of cells having a certain number of edges can be extracted at each iteration step and presented as the CEDH. The CEDH for the virtual tissue obtained in the cellular automata converges (in course of iterations) to the shape shown in Figure 3.13. It can be seen that the CEDH obtained using the cellular automata model reproduces experimental CEDH fairly well, and this indicates that (1) all the important processes affecting CEDH, such as Equal split division and the exponential relationship between the number of edges in a cell and probability of this cell to be divide, were captured and (2) confirm the results which were obtained using continuous and vertex models.

3.5 Conclusion

In this chapter, the formation of epithelial tissue topology as reflected by CEDH has been analysed. This analysis was performed using a few distinct models.

The vertex dynamics model for obtaining CEDHs in numerical simulations of virtual tissue was used. It has been noted that CEDH for virtual tissue has reproduced experimental observations remarkably well (Figure 3.3).

Then continuous analytical model was introduced, given by master equations, to analyse the impact of elementary processes associated with cell proliferation on the formation of CEDH. It was found in this study that in order to obtain CEDHs comparable with the experimental observations it should be taken into account that probability of cellular division increases exponentially with the number of edges of the dividing cell. In addition, it should be presumed that cells are commonly divided into roughly equal daughter cells (which was called "Equal split scenario").

Finally, The cellular automata model was introduced in this work and again used to produce virtual tissue and find the associated CEDH. Again, in order to obtain CEDH comparable with experimental observations, automata rules were set incorporating an exponential increase in the frequency of cellular division with the sidedness of dividing cell and the equal split scenario.

Solutions of the proposed analytical model have been found under the three

different scenarios of cellular division. Simulations using the computational models were analysed in the form of cell-edge distribution histograms and compared with the histogram obtained from actual experimental observations. The numerical simulations of virtual tissue were normally performed with $N = 1$ cells for vertex model and $N = 100$ cells for cellular automata model at time $t = 0$ and $p_i = 1/6$ for each $i = 4, \ldots, 9$ (equal initial proportions). Simulations showed that CEDH for virtual tissue converge to the form shown by cyan histograms that illustrate an agreement with EDG, as shown in Figure 3.3 for the vertex model and magenta histograms that are compatible with EDM, as given in Figure 3.13 for the virtual population model respectively.

An interesting observation derived from the simulations of the vertex model is that at the early stages of the simulation's time frame, the proliferation in epithelial tissue is synchronous, in contrast to the later stages where the process is asynchronous and only a small number of cells is divided in each window of time. Also, a more interesting observation is that the cells with a greater number of edges are divided more frequently than the cells with a smaller number of edges. The observed relationship between the number of edges in a cell and the frequency of division is shown in Figure 3.7, where an exponential trend line describes precisely this relationship for cells of 4 to 9 sides. The probability of division was almost equal to 1 for 9-sided cells.

The linear continuous model represented by master equations (under the assumption that cells divide with a probability that does not depend on their sidedness) was used for producing CEDHs. Under all three scenarios of cellular division, the histograms exhibit a right skewed distribution with a maximum value at 5 edges (blue, green and red histograms in Figure 3.10) which significantly differs from experimental CEDH (melrose histogram in Figure 3.10). This situation is not only true if the number of edges of the cells falls between 4 to 9 but also if the number of edges of the cells falls between 4 to 8, 9, 10, and 11 (see Figure 3.14). On the other hand, taking into account the exponential relationship between the frequency of division and the cell sidedness, a disagreement between the model's outcomes and the experimental observations for the cases of uniformly or binomially oriented divisions was observed here (blue and green histograms in Figure 3.11 respectively) but a precise agreement

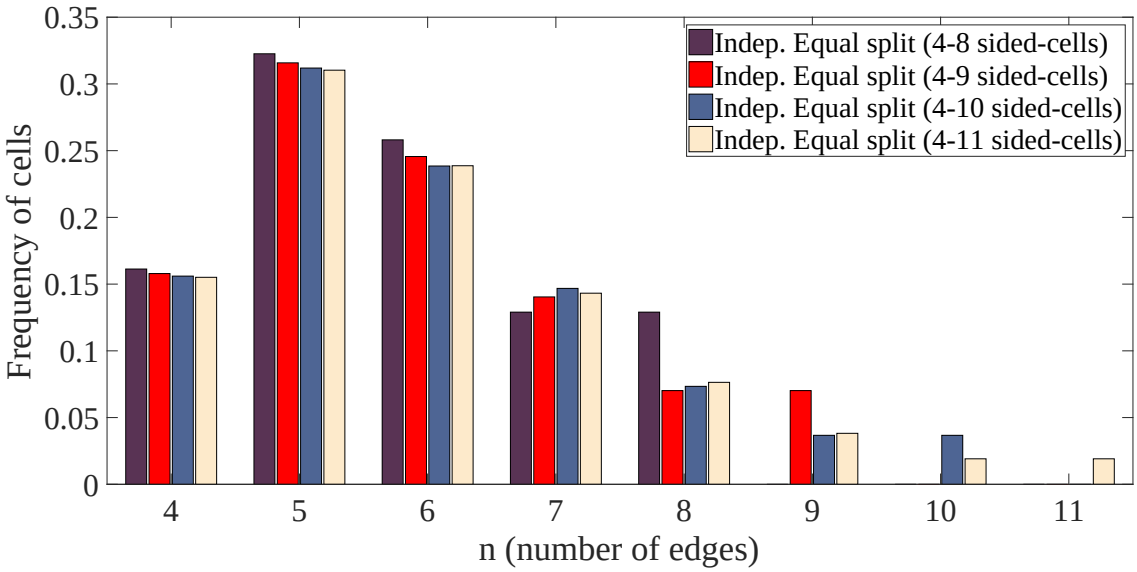

Figure 3.14: CEDHs obtained for the cells with 4 to 8, 9, 10 and 11 edges.

was observed for the case of equal split divisions (by comparing the red and the melrose histograms in Figure 3.11).

Modelling the evolution of cellular fractions could provide explanations for the mechanisms of the proliferation process and the development of epithelial tissues. Most of the previously reported models consider cells as polygons and analyse different dynamics acting either on their sides or on their vertices. In this study, new models are proposed which are based on a set of assumptions that can potentially explain why two remarkable previously reported models, the GPNP and the SCWN, have not entirely succeeded to reproduce the observed cell-edge distribution patterns. The most critical assumptions in the model in this study are (i) the unique order of cells vertices, which is important to determine the orientation of a division line, (ii) the relationship between the cell sidedness and the frequency of divisions, (iii) the absence of triangular and cells with more than 9 sides, and (iv) the asynchrony of divisions during the proliferation process. Instead of the discrete generations considered in GPNP and SCWN models, a continuous time is assumed in this model where a number of cells is divided in each small time interval. The proposed mathematical model expresses the rate of change of the fractions of i-sided cells over time and is assessed for three different scenarios of divisions, namely the uniformly oriented divisions, the binomially oriented divisions and the equal split divisions. Moreover, the results from the simulations of the computational vertex

model indicate an exponential relationship between the number of sides in a certain cell and the ability of the cell to divide.

Also, the results of simulations using the cellular automata model suggest that the scenario of equal split divisions can be the dominant action, as it attains a good correspondence between the computational and the experimental cell-edge distribution (Figure 3.3). These two observations are confirmed through the mathematical model, as only in the case of considering these two assumptions a good agreement is observed between the theoretical and the experimental histograms (red and melrose histograms in Figure 3.11). Moreover, unless using the exponential relationship, the CEDH of the cellular automata model cannot agree with the experimental data (see Figure 3.15).

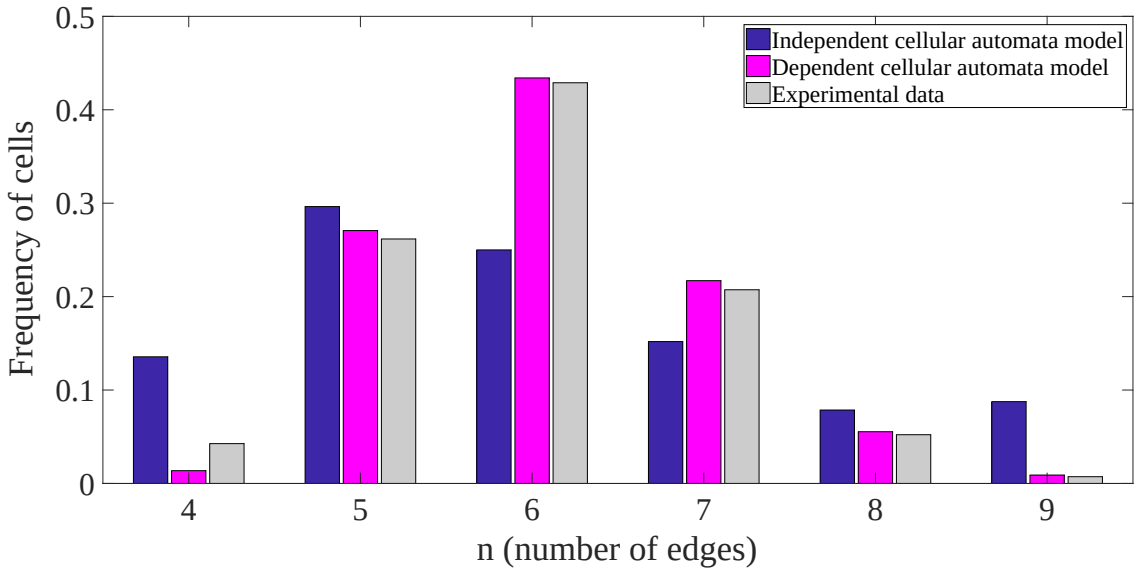

Figure 3.15: CEDHs of the dependent (using exponential relationship) and independent automata models in comparison to the experimental observations.

In conclusion it is noted that the proposed mathematical models successfully reproduced experimental CEDH and therefore can be used to explain the dynamics and mechanisms of cellular divisions. The models in this research indicate the effect of the cell's sidedness to its ability to proliferate and the effect of the order of cell's vertices to the orientation of the cleavage line. This can help with the understanding of the geometric features of epithelial tissues and its development and can be further used for assessing the role of other processes which occur in epithelia such as T1 transitions between neighbouring cells.

Chapter 4

Modelling cellular mixing in epithelial tissue

Abstract

Rearrangement of cells, commonly described in terms of T1-transitions, plays just as fundamental a role as cellular proliferation in shaping developing tissues. This chapter presents a modification of the vertex dynamics model which allows dynamic changes in cell shapes and cellular mixing in the virtual tissue. It was found that the tissue topology (as represented by cell-edge distribution histograms) in the so-modelled dynamic tissue has the same form as in the growing tissue (which was considered in the previous chapter). An analytical model was developed, (represented by master equations), as well as a cellular automata model, to reproduce and explain this observation. In particular, using the vertex dynamics model, it was found that the probability that a cell gains/loses edges in the course of T1-transitions increases/decreases with the number of its edges. Incorporating this observation into the analytical model is crucial for the histogram of the cell-edge distribution to be compatible with that observed in experiments and simulations.

4.1 Introduction

This chapter presents the modification of the vertex dynamics model (within the open-access software Chaste) which allows simulation of dynamic tissue, that is the tissue where cells undergo shape changes, resulting in cell mixing in the virtual tissue. This dynamic is particularly based on so-called T1-transitions. T1-transition is one of the three processes that constitute the manner of cell rearrangement in the vertex dynamics model. The cells that undergo T1-transition switch their vertices with their neighbours and a sequenced repetition of this process in the same direction generates intercalation and hence forms a plastic deformation. In this study, the vertex dynamics model was used to research this phenomenon. The process of T1-transition that occurs in many different materials such as bubbles of foam, biological cells and drops of emulsions has received much attention (17; 20; 61; 83; 89).

In the vertex dynamics model, as noted earlier, each cell can be associated with a two-dimensional polygon with a finite number of vertices and edges. These vertices adhere to rules that dominate the mechanisms which regulate the mechanical properties of epithelial cells. In the model in this study, each vertex was subjected to three different forces that determine the position of this vertex and, in turn, control the behaviour of the cell in terms of the contraction and expansion, the area and the perimeter. The tension force controls the length of edges through the value of its parameter, σ. The length of an edge becomes shorter, longer, or remains unchanged if the value of the parameter is positive, negative or zero respectively. The deformation force controls the area of the cells via the value of its parameter, ρ, where this force endeavours to return the area of the cells to the target area. The area of a cell becomes bigger, smaller or remains unchanged if the value of the parameter ρ is negative, positive or zero respectively. The perimeter force controls the perimeter of the cells via the value of its parameter, γ. This force attempts to return the perimeter of the cells to the target perimeter. The perimeter of a cell becomes shorter, longer or remains unchanged if the value of the parameter γ is positive, negative or zero, respectively.

To run a dynamical simulation, a computer code was built by modifying the tension force through manipulating the value of the parameter σ in order to

gain T1-transition by shortening or elongating the length of the edges, where a T1-transition can occur in consequence of the length of an edge shrinking to a certain tiny value. In a virtual tissue simulated by this modification of the vertex dynamics model, cells permanently undergo changes in their shapes and T1-transitions.

In the previous chapter, it was assumed that the CEDH is affected only by cellular proliferation while the number of edges in growing daughter cells does not change, unless affected by dividing neighbouring cells. Epithelial cells can, however, show dynamical changes in their shapes, manifested by T1-transitions (68), when one edge disappears (bringing together two distant cells) while another appears (separating two neighbouring cells) (see Figure 1.10). The effect of T1-transitions on CEDH in simulations was studied using the modified version of the vertex dynamics model. Cells in the simulation were not allowed to proliferate but forced to dynamically change and undergo T1-transitions. It was noted that T1-transitions change neither the number of cells nor the total number of cell edges so that the outcome of these simulations strongly depends on the initial state of the modelled tissue. Here a tissue composed of a considerable amount of cells with six edges per cell on average is considered, corresponding to the experimental case (55). These simulations show that when starting with a tissue containing a large number (1600 in our simulations) of hexagonal cells, the CEDH evolves towards a stationary shape, matching the experimental results. In addition, these simulations were used to find the relationship between the number of edges in the cells and the probability of these cells undergoing the $T1$-process.

In this work, an analytical model was built to study the evolution of the CEDH in the dynamic tissue. The histogram of the outcomes of this model is in a very good agreement with results of the simulations and experiments relating to cell divisions. Finally, to further confirm the results a cellular automata model was built for a tissue where cells undergo T1-transitions. The evolution of this tissue was simulated using Matlab. The results of these simulations confirmed the form of CEDH obtained using the analytical model and therefore enhanced the conclusions reached in this study.

4.2 Feedback mechanism in the definition of tension force allows dynamic changes in tissue

This dynamic approach builds on the idea of elongation and contraction that enforce cell elongation in a certain direction as a result of a sequence of T1-transitions. As mentioned earlier in this chapter, this model depends on manipulating the value of the tension force parameter, σ, that attempts to regulate the length of the edges in a tissue. In each time step, different edges might have different σ's value. The steps can be summarised as follows:

First, looping over the vertices, nodes, of the polygons that geometrically represent the cells in the cell population, these polygons can be called elements. All vertices are given zero force as initial values. All edges in the cell population have the same given σ (tension force parameter) value and these values change according to some rules, explained below, in contrast to the values of the other two parameters γ and ρ which are constant throughout the running of the simulations. To each vertex a constant vector is added, where each component represents the value of one of the forces that act on the vertices. After selecting a certain vertex (see figure 2.1), the elements that contain the vertex of interest, which here can be referred to as the local vertex, are looped over. The two vertices are then determined, the previous and next vertex, which are the vertices that come before and after the local vertex, respectively. These three vertices construct two edges, one of them referred to as the previous edge, which has the two ends vertices, which are the previous vertex and the local vertex. The other edge is referred to as the next edge which has the two ends vertices, the local vertex and the next vertex, where each of these two edges has a certain length and a certain σ value that must be determined in the simulation. The lengths of these edges are compared with their values in the previous time step correspondingly to find the difference between them. According to the differences between the current length of an edge and its previous length, referred to as the change in the length, the edge acquires a new σ value, where the change in the length determines the σ value of the current edge as follows:

- If the change in the length is greater than zero, then the value of the σ for the current edge is equal to its previous value + expansion feedback.

- If the change in the length is less than zero, then the value of the σ for the current edge is equal to its previous value - contraction feedback.
- If the change in the length is zero, then the value of the current edge is equal to its previous value.

Where this mechanism is applied to both the next edge and the previous edge and the expansion feedback and the contraction feedback are given constant values, these values must be chosen carefully to take into account the occurring of the process of T1-transition, and also to avoid the death of the cells. Hence the dynamic force can be defined as

$$F_{dynamic} = \sigma_{pc} * gradient_{pc} + \sigma_{nc} * gradient_{nc} \tag{4.1}$$

where σ_{pc} and σ_{nc} are the values of the previous and next edge, respectively, $gradient_{pc}$ and $gradient_{nc}$ are the values of the gradient of the previous and next edges, respectively as explained in Chapter 2.

This process is applied to all the vertices simultaneously. In the simulation in this study, the value of the parameters was chosen to be $\rho = 20$ with target area one, $\gamma = 10$; the initial value of σ was 2 between cell to cell and 250 between cells and their boundary. Each of the expansion feedback and the contraction feedback were taken to be 1.15. Figure 4.1 indicates the variation in the positions of the cells and their components, their vertices and edges, as well as the number of these components in each cell as a result of applying the forces that guide the cell rearrangement via the processes of T1-transition during the running of the simulation.

Figure 4.1a represents the initial state ($t = 0$) before applying the forces, where each cell has the same area with six vertices and six edges that have the same length. Figures 4.1b and 4.1d illustrate the situation after applying the forces (at time $t = 5$, and $t = 20$). As a consequence, a series of T1-transition events occur that lead to the area of some cells being changed and to the number of vertices for some cells to increase and for the others to decrease. However, the most significant observation is that some cells lose one or more of their neighbours and even the death of some cells may occur. For example, in the Figure 4.1b and as a result of processes of T1-transition, each of the cells 5, 10, 14 and 15 is no longer on the boundary, in

comparison to the initial state. T1-transition events resulted in removing the edge between the two cells 16 and 21 and adding an edge between the two cells 15 and 22; similarly it resulted in removing the edge between the two cells 15 and 20 and adding an edge between the two cells 10 and 21. In Figure 4.1c other T1-transition events can be observed in comparison to the Figure 4.1b. T1-transition events resulted in removing the edge between the two cells 10 and 21, 15 and 16 as well as 17 and 22 and adding an edge between the two cells 15 and 20, 11 and 22 as well as 16 and 23, respectively. In addition, Figure 4.1d shows that the T1-process may result in the death of some cells, as happened here with the cell 5, this cell was removed from the mesh because it has only three edges.

4.3 Cell-edge distribution in simulations of dynamic tissue undergoing cellular mixing

Topological change can happen in the system as a result of the switching process, i.e. when the two vertices that are connected by an edge change their connection with their neighbours owing to the edge coming close within an infinitesimal length, as can be shown in the Figure 1.10, (68). The T1-process is one of the most important approaches that plays a pivotal role in the rearrangement of the cells and plays a crucial role, alongside the division of the cells, in the consistency and controlling of the topological change, and consequently in the dynamic behaviour of the epithelial tissues.

T1 with T2 and T3 form the three deformation processes that guide the rearrangement of the cells. In this study, the focus was the T1-process rather than the other two processes because this process is the clearest and most prominent in the experimental observations. It is clear from the Figure 1.10 that the two neighbouring cells, B and C, are no longer neighbours as a result of the T1-process occurring through losing the shared edge that they, in turn, enabling the two cells, A and D, to be neighbouring cells by acquiring a shared edge. Therefore, this kind of action forms the dynamical process of the tissues. In this study, the cells that have more than three edges and that have less than ten edges were investigated, this being compatible with the experimental observations.

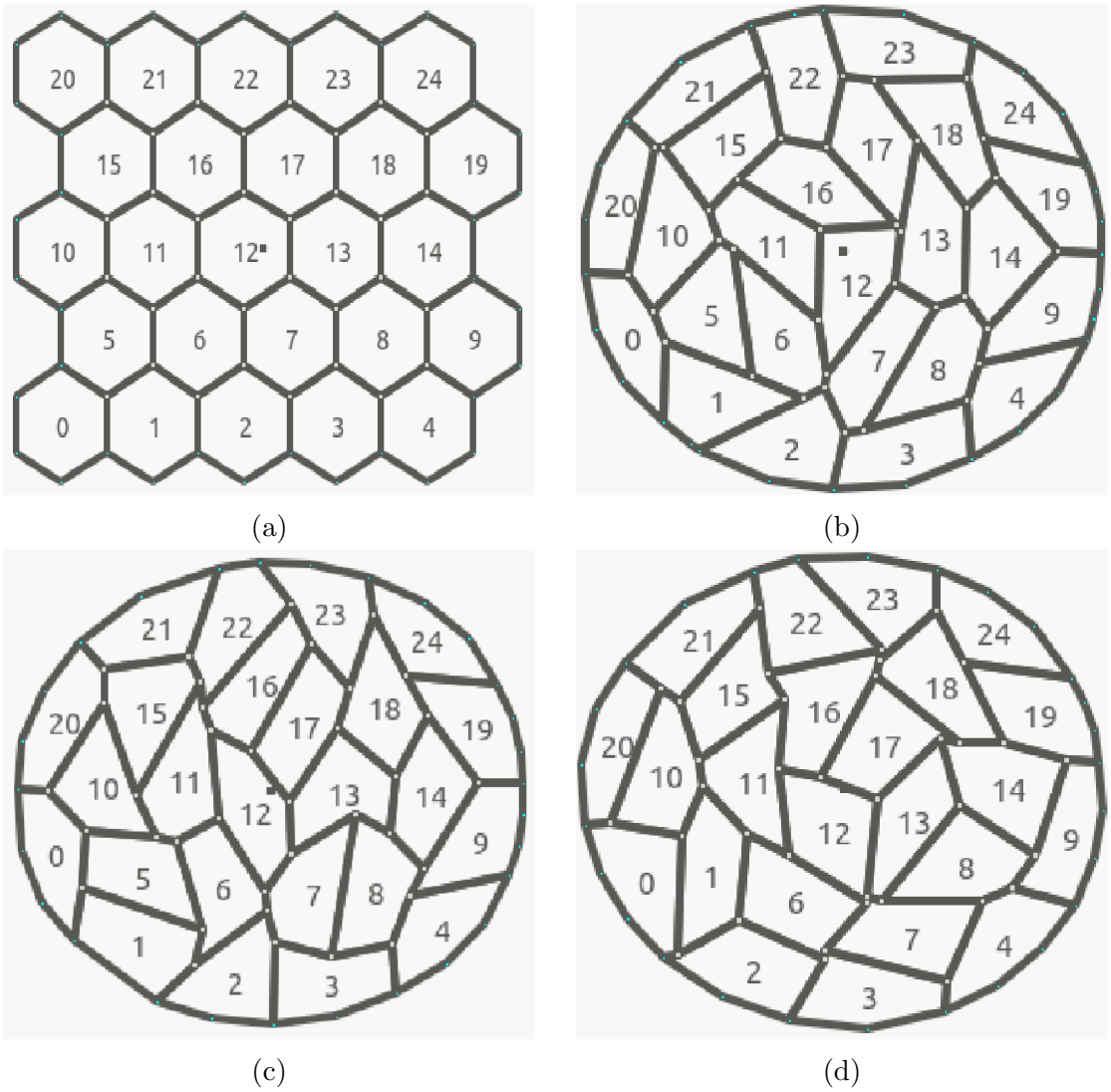

Figure 4.1: The cells undergo topological changes as a result of T1-transitions which change the area and the number of vertices (and edges) of cells. (a) The initial state of the tissue (time $t = 0$), where each cell is a hexagon with the same area and the edges have the same length. (b) The tissue at time $t = 5$. The vertices of the cells were subjected to the forces that generated the T1-transition events and caused changes to the area, the number of vertices and some cells lost some of their neighbours. (c) The tissue at time $t = 10$. Other T1-transition events occurred such as the shared edge between the two cells 17 and 22 in (b) was removed and an edge was added between the two cells 16 and 23. (d) The tissue at time $t = 20$. More T1-transition occurred and one of these events resulted in the death of the cell 5. Death means cell has three or less edges.

A simulation was run with 40×40 cells that underwent the $T1$-process, using the vertex dynamics model, where the vertices of the cells underwent deformation, tension, and with the perimeter forces having the parameters value $\rho = 20$, $\sigma = 1$ between cells, $\sigma = 125$ on the boundary and $\gamma = 10$. The time step was put on 0.501, the time starting from 0 and running to 200 with the target area of 1. The histograms of the cell-edge distribution that were taken from 76.152 to 199.899 have a significant stable agreement with the biological observations, as can be illustrated in Figure 4.2.

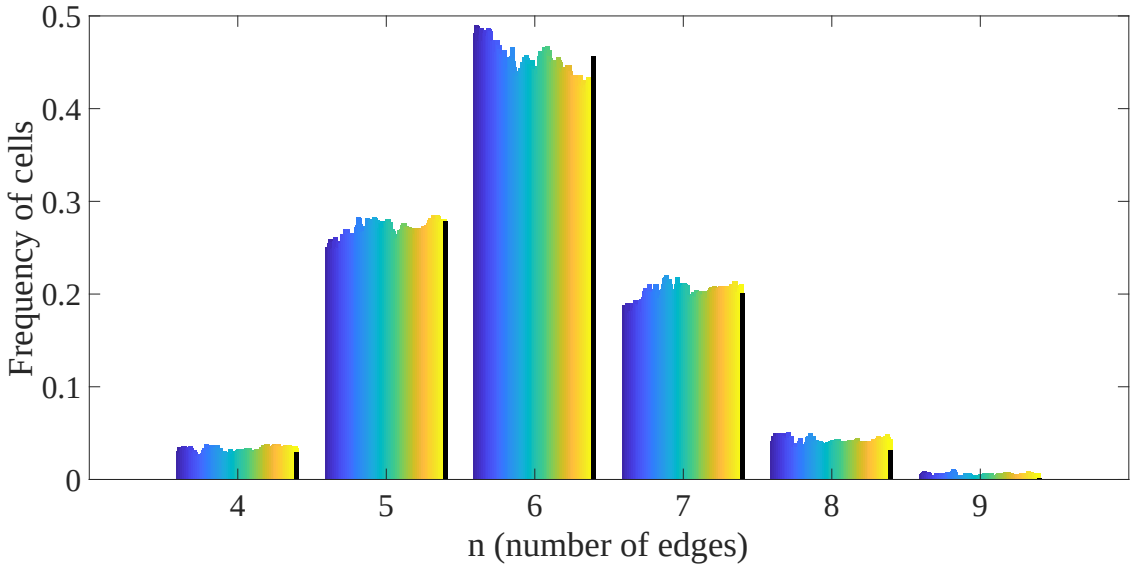

Figure 4.2: Comparison of cell-edge distribution obtained in experiments (black bars) and simulations (at different times, from blue, t=76, to yellow, t=200).

One of the most significant results that were observed by simulation is the relationship between the occurring of a T1-transition event and the number of edges in the cells affected by this transition. This can be described as

$$a_i^+ = \sum_{j=1}^{248} \frac{C_{ij}^+}{N_{ij}} \qquad a_i^- = \sum_{j=1}^{248} \frac{C_{ij}^-}{N_{ij}}, \tag{4.2}$$

where C_{ij}^+ (C_{ij}^-) is the number of cells with i-sides that gain (lose) an edge and become cells with $(i+1)$-sides ($(i-1)$-sides) in the time $76.152 + (j-1) * 0.501$ and N_{ij} represents the number of cells with i-sides in that time, where the simulation was run till the simulation time became 199.899 with the time step 0.501. The result, after normalising, can be depicted as in Figure 4.3.

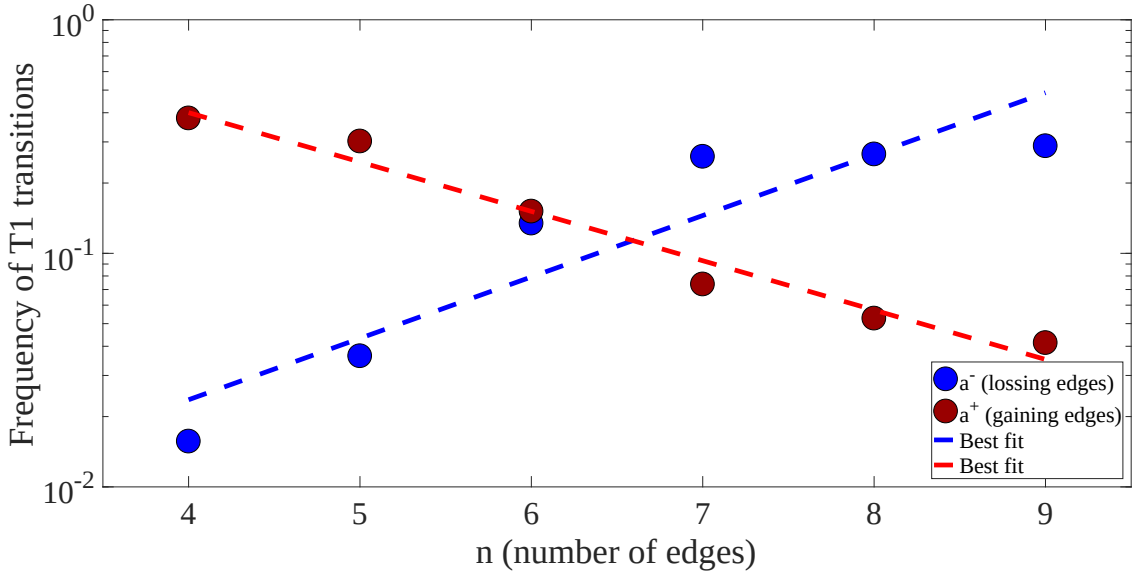

Figure 4.3: Frequency of n-sided cells gaining (a_n^+) and loosing (a_n^-) an edge in the course of T1-transitions as obtained from numerical simulations using the vertex model. Best fit means best fitting exponential function.

4.4 Analytical model for cell-edge distribution in tissue with cellular mixing

4.4.1 Master equations

In this model, a system of master equations was built to demonstrate the development of cellular fractions in the process of rearranging cells. The order of the vertices plays an important role because this model is based on the vertex model and the T1-process uses a mechanism that depends on changing the positions of the vertices. Irreversible deformations take place as a result of the processes of T1 occurring, where the epithelial tissues undergo elongation in the direction of the two neighbouring cells that shared an edge and that were lost, whereas the tissues confront shrinking in the orientation of the two cells that participate in a newly generated edge. Hence, the T1 processes represent the main factor of plasticity in the epithelial tissues. Here, only the cells with four to nine edges were taken into account and the cells beyond that neglected, as this is more compatible with experimental observations (25). The process of T1 in this model happens asynchronously (e.g. a small number of individual T1-processes occur in a small given time interval). Nevertheless, the T1-process is the only process that is involved in the development

of epithelium.

In this study, to construct a master equation, the total number of cells was denoted as $N(t)$ at time t; $N_i(t)$ denoted to the number of i-sided cells, whereas $p_i(t) = N_i(t)/N(t)$ represents the fraction of i-sided cells in the population. The rate of change of fraction of p_i with time can be given as

$$\frac{dp_i}{dt} = \frac{p_i(t+dt) - p_i(t)}{dt} = \frac{\frac{N_i+dN_i}{N} - \frac{N_i}{N}}{dt} = \frac{dN_i}{Ndt} \tag{4.3}$$

The Equation (4.3) was used to reproduce the cell-edge distribution in the epithelial tissues, analytically, in the case of applying the process of T1 that drives the rearrangement of cells. The master equation describing the dynamics of CEDH in a tissue without cell division can be written as:

$$\dot{p_i} = \alpha F_i, \tag{4.4}$$

where (similarly to Equation (3.1)) α defines the rate at which T1-transitions take place and F_i defines the probability of appearance/disappearance of i-sided cell in a single T1-transition event.

Linear model

The mathematical model of master equations with the assumption that cells can undergo the $T1$ topological change without depending on its sidedness was used for the illustration of histograms of the cellular fractions. Each individual T1 event causes the vanishing of one edge and the creation of a new one. Thus the two cells that have the vanishing edge lose their neighbour relationship and the two cells that have one end of the vanishing edge and share in the newly created edge gain an additional edge. Hence F_i can be constructed as

$$F_i = \begin{cases} -2p_i + 2p_{i+1} & \text{if } i = 4 \\ 2p_{i-1} - 4p_i + 2p_{i+1} & \text{if } i = 5, ..., 8 \\ 2p_{i-1} - 2p_i & \text{if } i = 9 \end{cases} \tag{4.5}$$

where p_i represents the probability for i-sided cell to lose or gain an edge in the case of a random T1-transition event, where all cells are assumed to have the same probability to undergo a T1-transition. Equations (4.4) and (4.5) define a linear system whose solution converges to the eigenvector corresponding to its zero-eigenvalue, which can be seen in the next subsection. The histogram differs significantly from the distribution of experimental data as shown in Figure 4.4, where the percentage acquiring a cell with any number of sides is equal. The

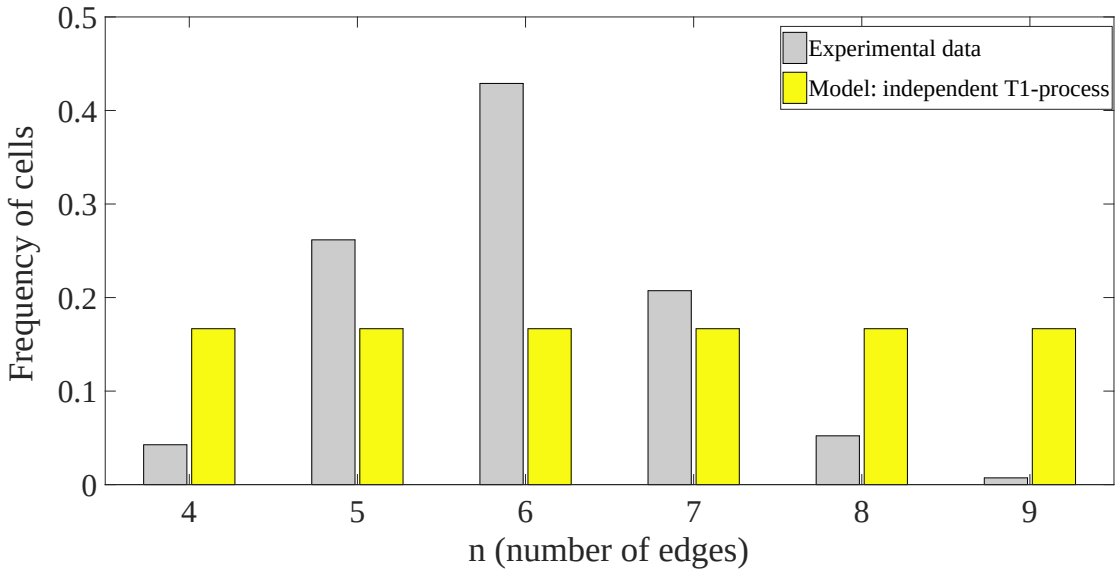

Figure 4.4: Cell-edge distribution predicted by the linear model is uniform (yellow bars) and is not comparable with experimental data, LZED, (grey bars).

results obtained from this linear model depends on the assumption that the same probability exists for all cells to undergo the T1 process, which is not supported by the simulations results. The results that were observed by the simulations show that there is a relationship between the number of edges in a cell and the probability of that cell undergoing the T1-transition event, as discussed later in this chapter. Moreover, the histograms of the cell-edge distribution obtained by simulation results are in good agreement with the experimental observations related to the cell divisions, as shown in Figure 4.2.

4.4.2 Eigen-solution for the linear model

The eigenvalue and eigenvectors were used here to confirm the results of the linear models. Through finding the eigenvalues of these systems, it was demonstrated

that all except one zero eigenvalue are negative and the solution converges to the eigenvector that corresponds to the zero-eigenvalue, which can be described as follows.

The matrix that defines the linear model is

$$A_{T1} = \begin{bmatrix} -2 & 2 & 0 & 0 & 0 & 0 \\ 2 & -4 & 2 & 0 & 0 & 0 \\ 0 & 2 & -4 & 2 & 0 & 0 \\ 0 & 0 & 2 & -4 & 2 & 0 \\ 0 & 0 & 0 & 2 & -4 & 2 \\ 0 & 0 & 0 & 0 & 2 & -2 \end{bmatrix}$$

The characteristic equation for this matrix which is the expansion of the equation $\det(A - \lambda I) = 0$, Therefore

$$\lambda^6 + 20\lambda^5 + 144\lambda^4 + 448\lambda^3 + 560\lambda^2 + 192\lambda = 0 \tag{4.6}$$

The vector of eigenvalues λ that provide the solution of the characteristic equation

$$\lambda_{T1} = \Big[-7.4641, -6.0000, -4.0000, -2.0000, -0.5359, 0\Big]$$

gives the solution of the Equations (4.6), using Matlab 17a, for finding the vales of λ. The corresponding eigenvectors are

$$EVe_{T1} = \begin{bmatrix} 0.1494 & 0.2887 & 0.4082 & -0.5000 & 0.5577 & 0.4082 \\ -0.4082 & -0.5774 & -0.4082 & -0.0000 & 0.4082 & 0.4082 \\ 0.5577 & 0.2887 & -0.4082 & 0.5000 & 0.1494 & 0.4082 \\ -0.5577 & 0.2887 & 0.4082 & 0.5000 & -0.1494 & 0.4082 \\ 0.4082 & -0.5774 & 0.4082 & 0.0000 & -0.4082 & 0.4082 \\ -0.1494 & 0.2887 & -0.4082 & -0.5000 & -0.5577 & 0.4082 \end{bmatrix}$$

Furthermore, the normalization of the eigenvector corresponding to the zero eigenvalue is

$$NEVCZ_{T1} = \Big[0.1667, 0.1667, 0.1667, 0.1667, 0.1667, 0.1667\Big]$$

which has the same values that were obtained by solving the linear model,
if it is assumed that all cells have the same probability of undergoing T1-transition. In this case, the Equations (4.3-4.5) define a linear system whose solution converges

to the eigenvector corresponding to its zero-eigenvalue. It can be shown analytically as well as numerically (by solving the system 4.3-4.5) that all components of this eigenvector are equal, resulting in uniform CEDH (see Figure 4.4). This solution obviously does not match experimental data.

4.4.3 Nonlinear model

As noted above, if it is assumed that any existing edge can undergo $T1$-transition with the same probability, the conclusion is that cells with more edges should loose edges more frequently. Frequencies at which cells with different sidedness gain or loose edges found from simulations using the vertex model are shown in Figure 4.3. It is evident that the probability that the cell gains/ loses an edge decreases/increases with the number of its edges. Thus in the reconstructed Equation (4.5), the probabilities for i-sided cells to gain/lose edge is adjusted according to the simulation data. Thus F_i can be rewritten as

$$F_i = \begin{cases} -2p_i^+ + 2p_{i+1}^- & \text{if } i = 4 \\ 2p_{i-1}^+ - 2p_i^- - 2p_i^+ + 2p_{i+1}^- & \text{if } i = 5, ..., 8 \\ 2p_{i-1}^+ - 2p_i^- & \text{if } i = 9 \end{cases} \tag{4.7}$$

where p_i^- and p_i^+ are probabilities for i-sided cell to lose or gain an edge. Here we have

$$p_i^+ \to \frac{a_i^+ p_i}{\Sigma a_i^+ p_i} \qquad p_i^- \to \frac{a_i^- p_i}{\Sigma a_i^- p_i}, \tag{4.8}$$

where the values of a_i^+ and a_i^- can be represented as in the equations in (4.2). The histogram representing the stationary solution of this model is in agreement with experimental data, Figure 5.1.

4.4.4 Cellular automata model for the dynamics of cell-edge distribution in the course of cell mixing

To enhance understanding of the impact of T1-transitions on the tissue topology, a cellular automata model, very similar to the one described in Chapter 3 was developed. The histogram in Figure 4.6 shows a virtual model in which each step

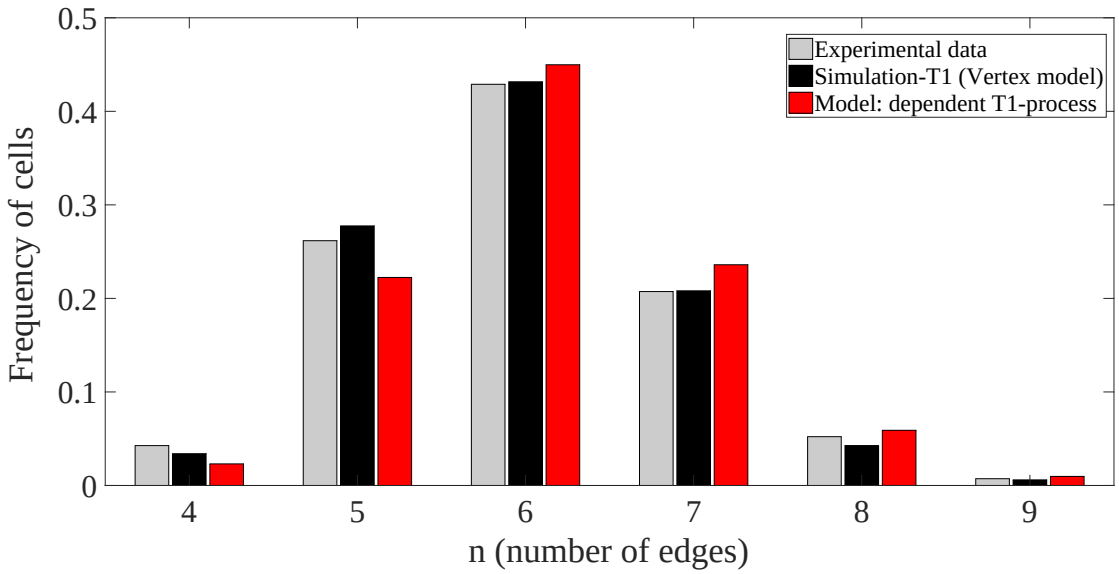

Figure 4.5: Cell-edge distribution in nonlinear model (red bars) as compared with the experimental observations (grey bars) and simulations (black bars). The Matlab codes are given in Appendix A.5

began by two cells chosen randomly to undergo the $T1$ process (avoiding 4-sided cells), switching their connected edge with their neighbours, thereby each losing one edge, and then another two cells also chosen randomly (avoiding 9-sided cells), to be the neighbours of the initial two cells. To each of them is added an extra edge. The process was repeated many times and then the result represented as a histogram. The outcomes show a very good agreement with the experimental observations. This was implemented using a Matlab code which is presented in Appendix A.6.

4.5 Conclusion

To study the cell rearrangements in epithelial tissues for the distribution of the cell edges, the case of the cells undergoing the process of T1-transitions was examined. Firstly, the simulations approach were used using the vertex dynamics model for a tissue of hexagonal cells. After the appropriate values for the parameters of forces that act on the vertices were chosen, the histograms of the cell-edge distribution show significant stable agreement with the biological observations of proliferating cells. Moreover, a new dynamics code was built inside the Chaste software to deal with the cell rearrangements, especially the T1-transitions. The simulation observations indicated that there is a relationship between the number of edges in the cells that are

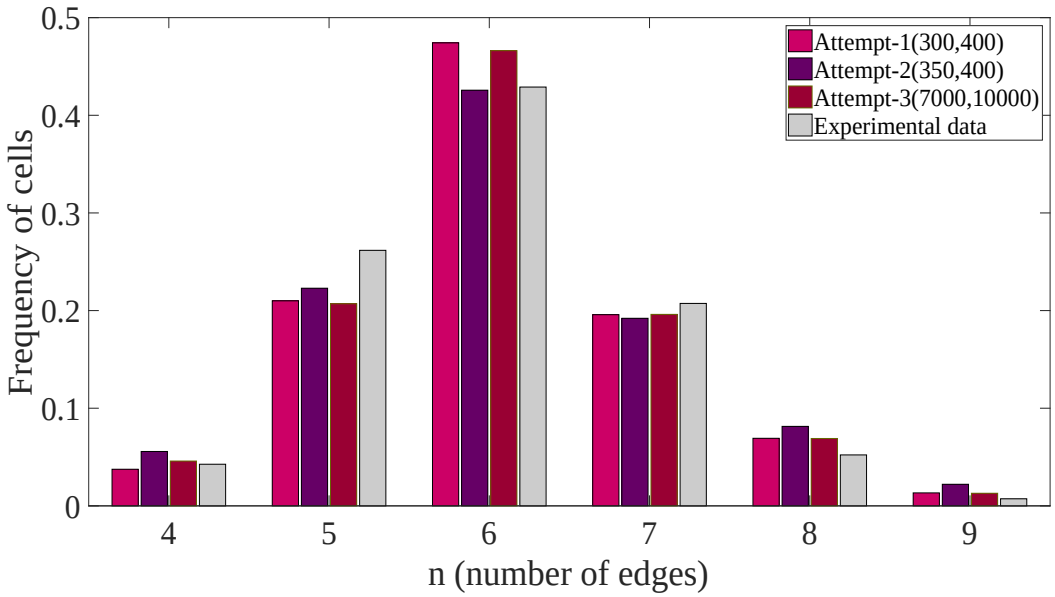

Figure 4.6: Cell-edge distribution in three realisations of cellular automata model as compared with the experimental observations, LZED, (grey). The first numbers in the brackets associated with the attempts refers to the number of cells and the second number refer to the number of iterations.

influenced by T1-transition and the probability of this T1-transition event occurring. In this study, a new mathematical model using the master equations was constructed to study the dynamical processes pertaining to the plastic deformations as a result of T1-processes.

The histogram of the results for this model shows significant disagreement with both the simulation observations and also with the experimental data, this being a result of assuming the equal probability of all cells to be undergoing the T1-transitions. Hence reformulating the model using the relationship between the number of edges of cells and the probability of the events of T1-transition occurring resulted in the histogram (Figure that shows that the model matches the experimental data for cell division.

Chapter 5

Conclusions and discussion

The aim of this thesis was to investigate some properties of the development of epithelial tissues using the vertex model. The study included the elasticity of the relaxations, the cell divisions and the rearrangements of the cells, limited to studying the process of T1-transition. This chapter starts with brief conclusions of the most fundamental results then presents the characteristics of the investigated topics by demonstrating the notable results in more detail. The results were compared with previous results where necessary. Finally, some aspects of future research relating to this study are raised.

5.1 The fundamental findings

This research focused on some behavioural aspects of the mechanical and dynamical properties of the epithelial tissue cells.

Chapter two dealt with the relaxation behaviour of the cells undergoing slight stretching/shrinking to test whether it is elastic or plastic. Initially, a single hexagonal cell was taken which had been subjected to forces: the tension force, the deformation force and the perimeter force. Consequently, the computational simulations and theoretical results indicated that the relaxation following slight stretching/shrinking is an exponential relaxation and, therefore, elastic. Moreover, the relaxation time when using three forces is half the relaxation time when exerting two forces, one necessarily the deformation force. Moreover, the relaxation behaviour when stretching /shrinking more than one cell and stretching a single cell with

different target lengths were examined. The simulation results in all these cases demonstrated that the relaxations are elastic and hence the relaxation times were determined. Finally, the analytical solution illustrated that the relaxation behaviour when stretching a tissue with an infinite number of cells (Tissues are composed of many cells. Therefore, considering infinite tissue in the model is justified) is elastic and has infinity relaxation time.

Chapter three was concerned with examining the cell divisions to find the distribution of cell edges, which has long been the subject of research, as reflected in the literature (25; 55; 79). The vertex dynamics model approach was employed using the open software, Chaste, to simulate the cell division behaviour. The simulation results showed that there exists an exponential relationship between the number of edges in the cells and the probability of these cells dividing, the opportunity for a cell to divide increasing as the number of edges increases. The histograms built for the cell-edge distribution obtained from the simulation results depicted a significant agreement when compared to those obtained from the biological data. A novel theoretical model was built to reproduce the cell-edge distribution using the master equations for three different scenarios: the uniformly oriented divisions, the binomially oriented divisions and the equal split divisions.

The histograms that were constructed showing the results for the cells in terms of the number of edges for these three models failed to be compatible with the biological observations. However, the models were reformulated using the exponential relationship and consequently the equal split histogram reflected a very good agreement with the biological observations, while the histograms relating to the two other scenarios improved significantly. In addition, an automata model was built to find the histogram of cell-edge distribution. This virtual model was based on the approach of the equal split model and the exponential relationship for dividing mother cells. The results also displayed a considerable agreement with the biological data observed in vitro (LZED).

Chapter four dealt with the dynamical behaviour of the epithelial tissues cells. To ease this area of investigation, first, some parts of the software Chaste was developed to render it more useful for the epithelial dynamical process. This new approach was based on the value of the tension force parameter. The dynamical behaviour of the

cells occurs as a consequence of the cell rearrangements. In biological observations, three of the different cell rearrangement processes were observed: T1-transitions, T2-transitions and T3-transitions. The focus of this research was T1-process as it is predominant in biological observations. The almost exponential relationship between the number of edges of the cells influenced by T1-process and the process of T1-transition occurring is one of the most interesting observations noted in the simulation outcomes. The cell-edge distribution histogram constructed from the simulation results show a very good agreement with the biological data of the cell divisions (Figure). In addition, a new theoretical model was presented to reproduce the cell-edge distribution for a tissue undergoing the T1-process, plastic deformation. Consequently, the CEDH associated with this exponential relationship also provides a considerable agreement with the biological observations of the cell divisions. An automata model was also built to reproduce the process of T1-transition using a Matlab code, the results of which are compatible with the simulation results for different times.

5.2 Elasticity behaviour in epithelial tissue

Elasticity is one of the material properties that provides resistance ability to any deformation and enables the material to be restored to its original status after removal of the external forces responsible for these created deformations. The deformation, in this case, is known as elastic; if not elastic, it is known as plastic. No ideal elastic material exists in nature; the materials that exhibit an elasticity are either those subjected to a slight deformation or subjected to external forces for a short time-scale. In physics, the elasticities for many materials have been studied intensively and the relating mathematical formulae found, such as the laws that govern the elasticity of stretching or compressing a spring (53; 58). In this research, the focus is the behaviour of epithelial cells when stretched/shrunk then released, having been subjected to some mechanical forces and for certain parameter values. Undoubtedly, the cytoskeleton, represented by its three principal elements, actin filament intermediate filaments and microtubule filaments, in addition to myosin, has a decisive influence in many cellular operations, such as cell divisions, motility,

adhesion and cell rearrangements. The cytoskeleton elements are polymer materials whose range of elasticity varies, the actin filaments possessing a wide range of elasticity in comparison to the other two filaments, and they together compose the elasticity of the cytoskeleton. Hence, the actomyosin is essential for providing the elasticity and maintaining the integrity of the epithelial cells (45; 48; 71). Moreover, a tissue which undergoes prolonged stretching or robust stretching may generate a plastic deformation (32).

This research concentrated on applying the mechanical forces F_i, F_d, and F_p to epithelial cells and stretching/shrinking these cells to show whether the produced relaxation after release from stretching/shrinking is elastic or not. Initially, it was proved numerically and analytically, that a cell stretched/shrank and subjected to two or three mechanical forces, so that the force F_d is always present, then released, shows an exponential relaxation and is therefore elastic.

For chosen arbitrary parameter values (see details in section 2.3), the relaxation time was halved from 16 in the case of applying two forces, to 8 in the case of applying the three forces. Then it was indicated numerically that the relaxation after stretching/shrinking more than one cell, alongside the application of the mechanical forces on the vertices of these cells, is also exponential and therefore elastic.

Also, the configuration shows an approximately linear relationship between the number of the cells and the relaxation times after a particular number of cells. In addition, a new force, the elastic force F_e (the modification of tension force by including the non-zero target length), was introduced instead of the tension force. The relaxation investigated for stretching is associated with applying the forces F_e, F_d, and F_p or the same forces without F_p on the vertices of a single cell for different edge target lengths to show the relaxation type that follows the release of stretching. The numerical work demonstrated that this relaxation is exponential and hence elastic. The results illustrate that the correlation between the relaxation times and the edge target lengths is quadratic in the first case and a bell curve in the second case.

Finally, the relaxation after stretching then releasing an infinite number of hexagonal epithelial cells after applying the three forces, which are tension, deformation and perimeter, indicated that this relaxation is exponential (elastic)

and has infinite relaxation time. In all these cases the values of the parameters of the forces-tension, deformation and perimeter- were $\sigma = 0.05$, $\rho = 1$ and $\gamma = 0.007$ respectively. These values were taken as default parameter values.

5.3 The characteristics of the cell-edge distribution model for the cell divisions

The apical side of epithelial cells take the polygonal shape with a different number of edges, for the study of which the vertex dynamics model is suitable. This model represents each cell geometrically, in two-dimensions, as a polygon. The vertex model has been used successfully in many cellular mechanisms, such as cell divisions and cell rearrangements (20; 68). The cell-edge distribution (CED) give the fractions with a various number of edges in a tissue. CED was intensively studied, experimentally, in the first half of the twentieth century by Lewis (54; 55) and has recently received attention in many studies, such as in GPNP and SWCN models (25; 79). However, all the theoretical attempts have failed to reproduce the CEDH that agrees with the empirical observations. Gibson and his co-workers have shown that the experimental data for different kinds of species exhibit a universal CEDH (25). However, in this research, a novel theoretical model was presented to reproduce the experimental observations with a significant agreement. The vertex dynamics model was also employed through the framework, Chaste, to simulate the CEDH, the outcomes being compatible with the theoretical and experimental results. The CEDH in all these approaches demonstrates that the hexagonal cells are predominant, with more than 40%, followed by the pentagonal and heptagonal cells, with each not less than 20%, then by the quadrilateral and octagonal cells, with each not less than 3%.

The GPNP model (25) is one of the main models used to study the CEDH which depends on some non-realistic assumptions. GPNP is a synchronous model which forces all cells to divide in each round of division, contradicting the fact that the division of the cells in a tissue is an asynchronous process by which a few cells can be divided with a short period of time. The other weakness of the GPNP model is in the way in which the edges of a mother cell are distributed between the two new

daughter cells, where the edges are distributed in a binomial random way between the daughter cells, following the donation of two of the mother edges to each new daughter. Moreover, this discrete model does not respect the order of the edges or vertices around the boundary of the cells. There is a congruence between the CEDH calculated by the GPNP model and that of the experimental observations for the wing disc Drosophila, except for one contradiction represented in the absence of quadrilateral cells.

SCWN models (79) have attempted to correct the drawbacks of the GPNP model whether related to the assumptions or related to the results. There are three SCWN models. The first model tried to solve the problem of the absence of the quadrilateral cells by allowing the three-edged cells to play the role of transition for acquiring the four-sided cells. The second and third models tried to solve the problem of the way in which the edges, and thereby the vertices, of a mother cell are distributed between the two daughter cells in order to render the results more unbiased, where the second model ignored the cells of less than four edges and distributed all the edges of the mother cells randomly between the two daughter cells, retaining the cells with four to nine edges. However, the absence of the four-sided cells in this model is inevitable as required by the mechanisms used in this model. The third model is similar to the second model except in allowing three-sided cells in order to acquire the cells with four edges. The CEDHs of all three of these models failed to agree with those of empirical observations. Therefore, a theoretical approach to reproducing the cell division process and its CEDH are presented in this thesis.

The mathematical model depends on creating master equations which depend on a basic formula that gives the rate of change of the fractions of the number of cells with respect to time. In this model, more realistic assumptions than the GPNP model or the SCWN models are taken. This model is asynchronous and respects the order of the vertices around the cells and also is a continuous model. The vertex dynamics model was the most suitable tool for dealing with the cell divisions as the apical sides of the epithelial cells take polygon shapes with the vertices and the edges are clear. Also, the results can be easily compared with those in vitro. However, the model outcomes remain far from those observed in vitro, unless the relationship between the number of edges in a cell and the probability of dividing this cell is

taking into account. In other words, the chance of dividing any cell depends on its number of edges: the more edges a cell has the faster it will divide. The CEDH of the equal split scenario, in this model, is in an approximate congruence to the CEDH of the empirical observations.

5.4 The characteristics of the cell-edge distribution model pertaining to plastic deformation

In this part of the research, the plastic deformations occurring that have run as a result of the cell rearrangement processes and precisely as a result of the T1-transitions were studied to describe the CEDH. For this, the vertex dynamics model was used through the open framework, Chaste, where an efficient part of a code was built within this framework to facilitate the case of the dynamical process of epithelial tissues, which depends on the parameter of the tension force. The dynamical mechanism enables a cell to move within the tissue that belongs to, through the processes of T1-transition. This process can occur as a result of removing an edge and generating a new edge shared between the two cells that contain the ends vertices of the removed edge. Moreover, since the length of a cell can be controlled through the value of the parameter σ, the code contains feedback factors that can increase or decrease the length of an edge which, in turn, may lead to the T1-transition occurring. The T1-transition with the other two processes, T2-transition and T3-transition, have the crucial role during the process of cell rearrangement.

As an initial condition, a dynamical simulation was implemented of a tissue with 1600 hexagonal cells subjects to T1-transitions. The outcomes illustrated two interesting observations. Firstly, the CEDHs for the results in different simulation times starting from 75 till 200, are almost identical to that CEDH related to the experimental observations of the cell divisions. Secondly, there is a relationship between the T1-transition occurring and the number of edges of the cells that are manipulated under the influence of this process. Moreover, a new theoretical model

was presented through building master equations that depend on a basic formula that takes into account the derivative of the fraction for the number of the cells with a certain number of edges with respect to time. The CEDH for the theoretical approach associated with the second observation of the simulation mentioned above is compatible with the CEDH of the outcomes of the simulation.

5.5 Future research

While working on this thesis, some concepts have been noted relating to this research which are anticipated to be the subject of future research. Here, these can briefly be summarized.

- In this study and through simulation, the elastic behaviour for the relaxation of stretching/shrinking a tissue was confirmed for many states, including for one cell or more than one cell. The relaxation behaviour that followed a slight stretching/shrinking was investigated with many different numbers of cells at zero and non-zero edge target length. However, in this work, the elasticity for a single cell and a tissue with an infinite number of cells was proven analytically. The analytical solutions for the other situations have been left aside for future research.

- Explore mechanisms that cause plastic deformations in tissues. Moreover, future work needs to focus on studying more properties and behaviours of the cell rearrangement, including studying behaviours of the T1-transition as well as T2-transition and T3-transition.

- During epithelial tissue development, cells migrate and this manifested by T1-transition events. However, experimental data on this process are not yet collect. This kind of experimental data would be used to validate our model.

- Analysis of mechanical properties of heterogeneous tissue.

- Any future work should focus more attention on the biological background to further understanding of the mechanical and dynamical properties of the cytoskeleton and its components, taking these properties into account in

simulations and theoretical research. Attempting to understand accumulated biological observations of the cell divisions, cell rearrangement and movement of cells will result in more realistic and robust mathematical approaches. More cooperation with biologists will be necessary for any future work.

- Understanding the behaviour of the tissue development and understanding the role of the cytoskeleton components will help to determine deviant behaviour such as abnormal divisions that can occur within the tissues and lead to serious diseases. This requires more thorough investigation and consideration in future research.

Appendix A

Codes

In this appendix, the Matlab codes are presented using different models for calculating the cell-edge distribution of cell divisions and as follows:

A.1 GPNP model and the second SCWN model

Lines 4 and 5, respectively, represent the formulae that used in the GPNP model and the second SCWN model. We constructed this code to make Figure 1.8 and the green histogram in Figure 1.9.

```
1  for n=4:9
2  for m=4:9
3     if (m≤n) && (m≥4)
4     T(n,m)=nchoosek(n-4,m-4)*1/(2^(n-4)); %GPNP Model
5     T(n,m)=nchoosek(n,m-2)*1/(2^n-2-2*n); %Second SCWN Model
6     else
7          T(n,m)=0;
8      end
9      if m==n+1
10         S(n,m)=1;
11     else
12         S(n,m)=0;
13     end
14 end
15 end
16 T=T(4:9,4:9);
17 S=S(4:9,4:9);
18 U=T*S
19 P0=[0 0 1 0 0 0]'
20 P=(U.'^10000)*P0
```

```
21  P_normalize= P/sum(P)
```

A.2 First and third SCWN models

Lines 4 and 5, respectively, represent the formulae that used in the first and third SCWN models. We constructed this code to make the first and third SCWN models Figure 1.9.

```
1  for n=3:9
2  for m=3:9
3     if (m≤n+1) && (m≥3)
4     T(n,m)=nchoosek(n-2,m-3)*1/(2^(n-2)); % Second SCWN Model
5     T(n,m)=nchoosek(n,m-2)*1/(2^n-2); % Third SCWN Model
6     else
7          T(n,m)=0;
8      end
9      if m==n+1
10         S(n,m)=1;
11     else
12         S(n,m)=0;
13     end
14 end
15 end
16 T=T(3:9,3:9);
17 S=S(3:9,3:9);
18 U=T*S;
19 P0=[0 0 0 1 0 0 0]';
20 P=(U.'^10000)*P0;
21 P_normalize_Third_SCWN = P/sum(P)
```

A.3 Analytical model represented by master equations in the case of cell division.

We constructed this code to make Figures 3.10 and 3.11. In the thesis σ_i is used instead of a_i, i=4,5,...,9.

```
1  function L=CED(S,C)
2  if S==1
3     a4=1; a5=1; a6=1; a7=1; a8=1; a9=1;
4  else
```

```
a4=0.0028;
a5=0.0080;
a6=0.0278;
a7=0.0939;
a8=0.2385;
a9=0.6290;
end
P=[0 0 1 0 0 0]';
for i=1:1:100000;
  s=1/(a4*P(1)+a5*P(2)+a6*P(3)+a7*P(4)+a8*P(5)+a9*P(6));
  s4=a4*s;s5=a5*s;s6=a6*s;s7=a7*s;s8=a8*s; s9=a9*s;
 if(C==1)
%-------------------------------------------------------------------------
% display('Uniformly oriented divisions')
%-------------------------------------------------------------------------

   A=[s4-3  s5   2/3*s6    2/4*s7    2/5*s8     2/6*s9;
       2    -3   2/3*s6    2/4*s7    2/5*s8     2/6*s9;
       0     2  -1/3*s6-3  2/4*s7    2/5*s8     2/6*s9;
       0     0   2        -2/4*s7-3  2/5*s8     2/6*s9;
       0     0   0           2      -3/5*s8-3   2/6*s9;
       0     0   0           0         2       -4/6*s9-1];
elseif(C==2)
%-------------------------------------------------------------------------
% display('Binomially oriented divisions')
%-------------------------------------------------------------------------
   A=[s4-3  s5    2/4*s6    2/8*s7    2/16*s8     2/32*s9;
       2    -3    s6        6/8*s7    8/16*s8     10/32*s9;
       0     2   -1/2*s6-3  6/8*s7    12/16*s8    20/32*s9;
       0     0     2       -6/8*s7-3  8/16*s8    20/32*s9;
       0     0     0         2       -14/16*s8-3  10/32*s9;
       0     0     0         0         2          -30/32*s9-1];
elseif(C==3)
%-------------------------------------------------------------------------
% display('Equal split divisions')
%-------------------------------------------------------------------------
A=[ s4-3    s5  0       0       0       0;
    2       -3  2*s6    s7      0       0;
    0       2   -s6-3   s7      2*s8    s9;
    0       0   2       -s7-3   0       s9;
    0       0   0       2       -s8-3   0;
    0       0   0       0       2       -s9-1];
 end
B=0.01*A+eye(6);
P=B*P;
end
P;
```

```
52 N=P/sum(P)
53 av_N=4*N(1)+5*N(2)+6*N(3)+7*N(4)+8*N(5)+9*N(6);
54 tot=sum(N)
55 end
```

A.4 Cellular automata model in the case of cell division

We constructed this code to make Figure 3.13

```
1  MinEdges= 4;
2  MaxEdges= 9;
3  MaxIterations= 100000;
4  N= 101;
5  format rat
6  %PC is the population of the cells accordingto the number of edges.
7  for i= 1:MaxEdges
8  PR(i)= 0;
9  PC(i)=0;
10 end
11
12 for i= MinEdges:MaxEdges
13  PR(i)= 4E-05*exp(1.1004*i);
14 % PR(i)=1.;
15 end
16 x=4:1:9;
17  plot(x,PR(x))
18 for i=MinEdges:MaxEdges
19 if mod(i,2)== 0
20 s(i)= (1/2)*i;
21 else
22     s(i)= (i+1)*(1/2);
23 end
24 DaughterOne([i],[1])=s(i)+2;
25 DaughterTwo([i],[1])= i+2-s(i);
26 end
27 for cell=1:N
28 CellEdges(cell)=randi([MinEdges,MaxEdges]);
29 PC(CellEdges(cell))=PC(CellEdges(cell))+1;
30 ICs(cell)=CellEdges(cell);
31 PC
32 end
33 for i=1:MaxIterations
```

```
DividingCell=randi([1,N]);
[m,n]=GetRandomNeighbours(DividingCell,CellEdges,N);m;n;
NumDividingCellEdges=CellEdges(DividingCell);
S=CellEdges(DividingCell);
R=randi([1,N])/N;
if R< PR(NumDividingCellEdges)
PC(CellEdges(DividingCell))= PC(CellEdges(DividingCell))-1;
NumOfDaughterEdges=randi([1,numel(DaughterOne(NumDividingCellEdges))]);
CellEdges(DividingCell)=DaughterOne([NumDividingCellEdges],[NumOfDaughterEdges]);
PC(CellEdges(DividingCell))=PC(CellEdges(DividingCell))+1;
CellEdges(N+1)=DaughterTwo([NumDividingCellEdges],[NumOfDaughterEdges]);
PC(CellEdges(N+1))=PC(CellEdges(N+1))+1;
CellEdges(m)=CellEdges(m)+1;
PC(CellEdges(m)-1)=PC(CellEdges(m)-1)-1;
PC(CellEdges(m))=PC(CellEdges(m))+1;
CellEdges(n)=CellEdges(n)+1;
PC(CellEdges(n)-1)=PC(CellEdges(n)-1)-1;
PC(CellEdges(n))=PC(CellEdges(n))+1;
N=N+1;
end
end
x = linspace(4,9);
PC;
F1=sum(PC);
FF1=PC/F1;
FFF1=[FF1(4),FF1(5),FF1(6),FF1(7),FF1(8),FF1(9)]
V=4:1:9;
p=plot(V,FFF1,'r','LineWidth',3)
PC=PC;
SumPC=sum(PC)
```

Subroutine to pick two neighbours randomly.

```
function [m,n]=GetRandomNeighbours(DividingCell,CellEdges,N)
NumIters=0;
%Find the first random cell...
notfound=1;
while notfound==1
 if NumIters > N
     print('Max Iterations Reached!')
     return
 end
 cellid=randi([1,N]);
 CellEdges(cellid);
 if DividingCell≠cellid && CellEdges(cellid)≠9
    m=cellid;
     notfound=2;
```

```
 end
 NumIters=NumIters+1;
end
NumIters=0;
%Find the second random cell...
notfound=1;
while notfound==1
 if NumIters > N
     print('Max Iterations Reached!')
     return
 end
 cellid=randi([1,N]);
 if DividingCell≠cellid && cellid ≠ m && CellEdges(cellid)≠9
    n=cellid;
     notfound=2;
 end
 NumIters=NumIters+1;
end
end
```

A.5 Analytical model that is represented by master equations in the case of plastic deformation

We constructed this code to make Figures Figures 4.4 and 5.1.

```
 function L=CED_T1(S)
if S==1
   a4d=1;a5d=1;a6d=1;a7d=1;a8d=1;a9d=1;a4i=1;a5i=1;a6i=1;a7i=1;a8i=1;a9i=1;
else
a4d=    0.015665993 ;   a4i=    0.379026104;
a5d=    0.036343297 ;   a5i=    0.301917398;
a6d=    0.134422909 ;   a6i=    0.151273031;
a7d=    0.259634634 ;   a7i=    0.073738651;
a8d=    0.265765941 ;   a8i=    0.052671697;
a9d=    0.288167226 ;   a9i=    0.041373119;
end
P=[0 0 1 0 0 0]';
for i=1:1:1000000
 sd=1/(a4d*P(1)+a5d*P(2)+a6d*P(3)+a7d*P(4)+a8d*P(5)+a9d*P(6));
    s4d=a4d*sd;s5d=a5d*sd;s6d=a6d*sd;s7d=a7d*sd;s8d=a8d*sd;s9d=a9d*sd;
  si=1/(a4i*P(1)+a5i*P(2)+a6i*P(3)+a7i*P(4)+a8i*P(5)+a9i*P(6));
```

```
  s4i=a4i*si;s5i=a5i*si;s6i=a6i*si;s7i=a7i*si;s8i=a8i*si;s9i=a9i*si;
 A=[-2*s4i  2*s5d       0     0     0     0;
       2*s4i    -2*s5d-2*s5i   2*s6d   0     0     0;
       0     2*s5i    -2*s6d-2*s6i   2*s7d    0     0;
       0     0   2*s6i    -2*s7d-2*s7i   2*s8d     0;
       0     0   0          2*s7i    -2*s8d-2*s8i   2*s9d;
       0     0   0           0         2*s8i    -2*s9d];
B=0.01*A+eye(6);
P=B*P;
end
P;
tot=sum(P);
N=P/sum(P)
end
```

A.6 Cellular automata model in the case of plastic deformation

We constructed this code to make Figure 4.6.

```
MinEdges= 4;
MaxEdges= 9;
MaxIterations=7000;
N= 10001;
for i= 1:MaxEdges;
PD(i)=0;
end
for cell=1:N;
CellEdges(cell)=6;
ICs(cell)=CellEdges(cell);
end
for i=1:MaxIterations;
T1CellDecreamentEdges1=randi([1,N]);
while CellEdges(T1CellDecreamentEdges1)==4
    T1CellDecreamentEdges1=randi([1,N]);
end
T1CellDecreamentEdges2=randi([1,N]);
while T1CellDecreamentEdges2==T1CellDecreamentEdges1
|CellEdges(T1CellDecreamentEdges2)==4
    T1CellDecreamentEdges2=randi([1,N]);
end
T1CellIncreamentEdges1=randi([1,N]);
while T1CellIncreamentEdges1==T1CellDecreamentEdges1
```

```
| T1CellIncreamentEdges1==T1CellDecreamentEdges2
|CellEdges(T1CellIncreamentEdges1)==9
    T1CellIncreamentEdges1=randi([1,N]);
end
T1CellIncreamentEdges2=randi([1,N]);
while T1CellIncreamentEdges2==T1CellDecreamentEdges1
| T1CellIncreamentEdges2==T1CellDecreamentEdges2
| T1CellIncreamentEdges2==T1CellIncreamentEdges1
| CellEdges(T1CellIncreamentEdges2)==9
    T1CellIncreamentEdges2=randi([1,N]);
end
CellEdges(T1CellDecreamentEdges1)=CellEdges(T1CellDecreamentEdges1)-1;
PD(CellEdges(T1CellDecreamentEdges1)+1)=PD(CellEdges(T1CellDecreamentEdges1)+1)+1;
CellEdges(T1CellDecreamentEdges2)=CellEdges(T1CellDecreamentEdges2)-1;
PD(CellEdges(T1CellDecreamentEdges2)+1)=PD(CellEdges(T1CellDecreamentEdges2)+1)+1;
CellEdges(T1CellIncreamentEdges1)=CellEdges(T1CellIncreamentEdges1)+1;
PD(CellEdges(T1CellIncreamentEdges1)-1)=PD(CellEdges(T1CellIncreamentEdges1)-1)+1;
CellEdges(T1CellIncreamentEdges2)=CellEdges(T1CellIncreamentEdges2)+1;
PD(CellEdges(T1CellIncreamentEdges2)-1)=PD(CellEdges(T1CellIncreamentEdges2)-1)+1;
end
format short
PD;
F=sum(PD);
FF=PD/F;
FFF=[FF(4),FF(5),FF(6),FF(7),FF(8),FF(9)]'
V=4:1:9;
plot(V,FFF)
```

Appendix B

Installing and dealing with Chaste

B.1 How to install and deal with Chaste

To install the open software Chaste which is described in detail at http://www.cs.ox.ac.uk/chaste, the following steps need to be taken

1. Download the operating system Linux, Ubuntu 14.04 LTS.

2. Download Qt Creator 3.0.1, for visualization of results.

3. Install the software Chaste that corresponds to Ubuntu 14.04 LTS, with trust Ubuntu code name, and all other required dependencies. Instructions for installing the open software Chaste can be found at https://chaste.cs.ox.ac.uk/trac/wiki/InstallGuides/UbuntuPackage.

4. Many other items need to be checked to ensure that they are installed. Some of them are mandatory for running the software Chaste, such as CMake, SCONS, Boost, PETSc, XMLTools and PyCml with its dependencies, and others are optional, such as VtkStatic and TextTest. All these details are given at https://chaste.cs.ox.ac.uk/trac/wiki/InstallGuides/InstallGuide and https://chaste.cs.ox.ac.uk/trac/wiki/DeveloperInstallGuide.

5. Install the integrated development environment, Eclipse IDE for C/C++ Developers. Version: Luna Service Release 2 (4.4.2) or any other version that deals with C++.

More details about how to deal with the software Chaste can be found on the CD disc/README.

Bibliography

[1] A. Abdullah, D. Avraam, O. Chepizhko, T. Vaccari, S. Zapperi, C. A. M. La Porta, and B. Vasiev. Universal statistics of epithelial tissue topology. 2017.

[2] D. A. Aboav. The arrangement of grains in a polycrystal. *Metallography*, 3(4):383 – 390, 1970.

[3] D. A. Aboav. The arrangement of cells in a net. *Metallography*, 13(1):43 – 58, 1980.

[4] P. J. Albert and U. S. Schwarz. Dynamics of cell shape and forces on micropatterned substrates predicted by a cellular Potts model. *Biophys. J.*, 106(11):2340–2352, 2014.

[5] B. Alberts, D. Bray, K. Hopkin, A. Johnson, J. Lewis, M. Raff, K. Roberts, and P. Walter. *Essential cell biology.* New York, USA : Garland Science, 2014.

[6] B. Alberts, A. Johnson, J. Lewis, D. Morgan, M. Raff, K. Roberts, P. Walter, J. Wilson, and T. Hunt. *Molecular biology of the cell.* New York, NY : Garland Science, Taylor and Francis Group, 2015.

[7] D. B. Alexander and G. S. Goldberg. Transfer of biologically important molecules between cells through gap junction channels. *Curr. Med. Chem.*, 10(19):2045–2058, 2003.

[8] A. R. Bausch, F. Ziemann, A. A. Boulbitch, K. Jacobson, and E. Sackmann. Local measurements of viscoelastic parameters of adherent cell surfaces by magnetic bead microrheometry. *Biophys. J.*, (4):2038–2049, 1998.

[9] C. Besson, F. Bernard, F. Corson, H. Rouault, E. Reynaud, A. Keder, K. Mazouni, and F. Schweisguth. Planar cell polarity breaks the symmetry of

par protein distribution prior to mitosis in drosophila sensory organ precursor cells. *Curr Biol*, 25(8):1104–10, 2015.

[10] G. W. Brodland. Computational modeling of cell sorting, tissue engulfment, and related phenomena: A review. *Appl. Mech. Rev.*, 57(1):47, 2004.

[11] G. W. Brodland and J. H. Veldhuis. Computer simulations of mitosis and interdependencies between mitosis orientation, cell shape and epithelia reshaping. *J. Biomech.*, 35(5):673 – 681, 2002.

[12] C. Bustamante, Y. R. Chemla, N. R. Forde, and D. Izhaky. Mechanical processes in biochemistry. *Annu. Rev. Biochem.*, 73:705–48, 2004.

[13] O. Canela-Xandri, F. Sagués, J. Casademunt, and J. Buceta. Dynamics and mechanical stability of the developing dorsoventral organizer of the wing imaginal disc. *PLoS Comput. Biol.*, 7(9):28–32, 2011.

[14] J. M. Churko and D. W. Laird. Gap junction remodeling in skin repair following wounding and disease. *Physiol.*, 28(27):190–198, 2013.

[15] G. M. Cooper and R. E. Hausman. *The cell.* Sinauer Associates Sunderland, 2000.

[16] G. M. Cooper and R. E. Hausman. *The cell: a molecular approach.* Washington, D.C. : ASM Press, 2009.

[17] R. David, O. Luu, E. W. Damm, J. W. H. Wen, M. Nagel, and R. Winklbauer. Tissue cohesion and the mechanics of cell rearrangement. *Development*, 141(19):3672–3682, 2014.

[18] X. Du, M. Osterfield, and S. Y. Shvartsman. Computational analysis of three-dimensional epithelial morphogenesis using vertex models. *Phys. Biol.*, 11(6):066007, 2014.

[19] A. Erber, D. Riemer, M. Bovenschulte, and K. Weber. Molecular phylogeny of metazoan intermediate filament proteins. *J. mol. evol.*, 47(6):751–762, 1998.

[20] R. Farhadifar, J. C. Röper, B. Aigouy, S. Eaton, and F. Jülicher. The Influence of Cell Mechanics, Cell-Cell Interactions, and Proliferation on Epithelial Packing. *Curr. Biol.*, 17(24):2095–2104, 2007.

[21] A. G. Fletcher, J. M. Osborne, P. K. Maini, and D. J. Gavaghan. Implementing vertex dynamics models of cell populations in biology within a consistent computational framework. *Prog. Biophys. Mol. Biol.*, 113(2):299–326, 2013.

[22] A. G. Fletcher, M. Osterfield, R. E. Baker, and S. Y. Shvartsman. Vertex models of epithelial morphogenesis. *Biophys. J.*, 106(11):2291–2304, 2014.

[23] D. Fristrom. The cellular basis of epithelial morphogenesis. A review. *Tissue and Cell*, 20(5):645–690, 1988.

[24] K. Fukushima, H. Fujita, T. Yamaguchi, M. Kawaguchi, H. Tsukaya, and M. Hasebe. Oriented cell division shapes carnivorous pitcher leaves of *Sarracenia purpurea. Nat. Commun.*, 6:6450, 2015.

[25] M. C. Gibson, A. B. Patel, R. Nagpal, and N. Perrimon. The emergence of geometric order in proliferating metazoan epithelia. *Nature*, 442(7106):1038–41, 2006.

[26] F. Gittes, B. Mickey, and J. Nettleton, J.and Howard. Flexural rigidity of microtubules and actin filaments measured from thermal fluctuations in shape. *J. Cell Biol.*, (4):923, 1993.

[27] J. A. Glazier and F. Graner. Simulation of the differential adhesion driven rearrangement of biological cells. *PHYSICAL REVIEW E*, 47(3):2128 – 2154, 1993.

[28] J. M. Gomez, L. Chumakova, N. A. Bulgakova, and N. H. Brown. Microtubule organization is determined by the shape of epithelial cells. *Nat. Commun.*, 7:13172, 2016.

[29] D. Goodenough and D. Paul. Gap junctions. *Cold Spring Harb. Perspect. Biol.*, 1:1–20, 2009.

[30] M. A. Gorokhovski and V. L. Saveliev. Analyses of Kolmogorov's model of breakup and its application into Lagrangian computation of liquid sprays under air-blast atomization. *Phys. of Fluids*, 15(1):184–192, 2003.

[31] F. Graner and J. A. Glazier. Simulation of biological cell sorting using a two-dimensional extended potts model. *Phys. Rev. Lett.*, 69(13):2013–2016, 1992.

[32] C. Guillot and T. Lencuit. Mechanics of Epithelial Tissue Homeostasis and Morphogenesis. *Science*, 340:1185–1189, 2013.

[33] J. A. Guttman and B. B. Finlay. Tight junctions as targets of infectious agents. *Biochim. Biophys. Acta, Biomembr.*, 1788(4):832–841, 2009.

[34] H. Harashima, N. Dissmeyer, and A. Schnittger. Cell cycle control across the eukaryotic kingdom. *Trends Cell Biol.*, 23(7):345–356, 2013.

[35] D. G. Harvey, A. G. Fletcher, J. M. Osborne, and J. Pitt-Francis. A parallel implementation of an off-lattice individual-based model of multicellular populations. *Comput. Phys. Commun.*, 192:130–137, 2015.

[36] W. Helfrich. Elastic properties of lipid bilayers: theory and possible experiments. *Z. Naturforsch*, 28c:693–703, 1973.

[37] H. Honda and G. Eguchi. How much does the cell boundary contract in a monolayered cell sheet? *J. Theor. Biol.*, 84(3):575–588, 1980.

[38] H. Honda and T. Nagai. Cell models lead to understanding of multi-cellular morphogenesis consisting of successive self-construction of cells. *J. Biochem.*, 157(3):129–136, 2015.

[39] H. Honda, T. Nagai, and M. Tanemura. Two different mechanisms of planar cell intercalation leading to tissue elongation. *Dev. Dyn.*, 237(7):1826–1836, 2008.

[40] H. Honda, Y. Ogita, S. Higuchi, and K. Kani. Cell Movements in a Living Mammalian Tissue : Long-term Observation of Individual Cells in Wounded Corneal Endothelia of Cats. *J. Morphol.*, 174(1):25–39, 1982.

[41] H. Honda, M. Tanemura, and T. Nagai. A three-dimensional vertex dynamics cell model of space-filling polyhedra simulating cell behavior in a cell aggregate. *J. Theor. Biol.*, 226(4):439–453, 2004.

[42] J. Howard. *Mechanics of motor proteins and the cytoskeleton.* Sinauer Associates Inc. Sunderland, MA, 2001.

[43] R. O. Hynes. Integrins: Versatility, modulation, and signaling in cell adhesion. *Cell*, 69(1):11–25, 1992.

[44] Y. Ishimoto and Y. Morishita. Bubbly vertex dynamics: A dynamical and geometrical model for epithelial tissues with curved cell shapes. *Phys. Rev. E*, 90(5):052711, 2014.

[45] P. A. Janmey, U. Euteneuer, P. Traub, and M. Schliwa. Viscoelastic Properties of Vimentin Compared With Other Filamentous Biopolymer Networks. *J. Cell Biol.*, 113(1):155–160, 1991.

[46] P. A. Janmey and R. T. Miller. Mechanisms of mechanical signaling in development and disease. *J. Cell Sci.*, 124(Pt 1):9–18, 2011.

[47] J.-F. Joanny. Active behavior of the cell cytoskeleton. *Prog. Theor. Phys. Suppl.*, (165):100–102, 2006.

[48] F. Jülicher, K. Kruse, J. Prost, and J. F. Joanny. Active behavior of the Cytoskeleton. *Phys. Rep.*, 449(1-3):3–28, 2007.

[49] K. Kawasaki and K. Nagai, T.and Nakashima. Vertex model for two-dimensional grain growth. *Phil. Mag. B*, 60(3):399–421, 1989.

[50] A. N. Kolmogorov. Über das logarithmisch normale Verteilungsgesetz der Dimensionen der Teilchen bei Zerstückelung. *Dokl. Akad. Nauk SSSR*, 31:99–101, 1941.

[51] D. Kuipers, A. Mehonic, M. Kajita, L. Peter, Y. Fujita, T. Duke, G. Charras, and J. E. Gale. Epithelial repair is a two-stage process driven first by dying cells and then by their neighbours. *J. Cell Sci.*, 127(6):1229–1241, 2014.

[52] C. A. M. La Porta and S. Zapperi. *The Physics of Cancer.* Cambridge University Press, 2017.

[53] L. D. Landau and E. M. Lifshits. *Theory of elasticity.* Course of theoretical physics (Landau and Lifshits): 7. London: Pergamon, 1959.

[54] F. T. Lewis. The effect of cell division on the shape and size of hexagonal cells. *Anat. Rec.*, 33(5):331–355, 1926.

[55] F. T. Lewis. The correlation between cell division and the shapes and sizes of prismatic cells in the epidermis of cucumis. *Anat. Rec.*, 38(3):341–376, 1928.

[56] F. T. Lewis. A volumetric study of growth and cell division in two types of epithelium, the longitudinally prismatic epidermal cells of tradescantia and the radially prismatic epidermal cells of cucumis. *Anat. Rec.*, 47(1):59–99, 1930.

[57] H. Lodish, A. Berk, C. A. Kaiser, M. Krieger, A. Bretcher, H. Ploegh, A. Amon, and M. P. Scott. *Molecular cell biology.* New York : W.H. Freeman & Co., 2013.

[58] A. Maceri. *Theory of elasticity.* Berlin ; London : Springer, 2010.

[59] R. Malgat, F. Faure, and A. Boudaoud. A mechanical model to interpret cell-scale indentation experiments on plant tissues in terms of cell wall elasticity and turgor pressure. *Front. Plant Sci.*, 7:1351, 2016.

[60] M. Marder. Soap-bubble growth. *Phys. Rev. A*, 36(1):438–440, 1987.

[61] P. Marmottanta, A. Mgharbel, J. Käfer, B. Audren, J.-P. Rieu, J.-C. Vial, B. van der Sanden, A. F. M. Mare, F. Graner, H. Delanoë-Ayari, and R. H. Austin. The role of fluctuations and stress on the effective viscosity of cell aggregates. *Proc. Natl. Acad. Sci. U.S.A.*, (41):17271, 2009.

[62] F. A. Meineke, C. S. Potten, and M. Loeffler. Cell migration and organization in the intestinal crypt using a lattice-free model. *Cell Prolif.*, 34(4):253 – 266, 2001.

[63] R. M. H. Merks and J. A. Glazier. A cell-centered approach to developmental biology. *Physica A*, 352(1):113–130, 2005.

[64] G. R. Mirams, C. J. Arthurs, M. O. Bernabeu, R. Bordas, J. Cooper, A. Corrias, Y. Davit, S. J. Dunn, A. G. Fletcher, D. G. Harvey, M. E. Marsh, J. M. Osborne, P. Pathmanathan, J. Pitt-Francis, J. Southern, N. Zemzemi, and D. J. Gavaghan. Chaste: An Open Source C++ Library for Computational Physiology and Biology. *PLoS Comput. Biol.*, 9(3):e1002970, 2013.

[65] L. L. Mitic and J. M. Anderson. Molecular architecture of tight junctions. *Annu. Rev. Physiol.*, 60:121–142, 1998.

[66] J. D. Murray. *Mathematical Biology I: An Introduction.* Springer New York, 3 edition, 2002.

[67] J. D. Murray. *Mathematical Biology II: Spatial Models and Biomedical Applications.* Springer New York, 3 edition, 2003.

[68] T. Nagai and H. Honda. A dynamic cell model for the formation of epithelial tissues. *Philos. Mag. B*, 81(7):699–719, 2001.

[69] T. Nagai and H. Honda. Computer simulation of wound closure in epithelial tissues: Cell-basal-lamina adhesion. *Phys. Rev. E*, 80(6):061903, 2009.

[70] W. J. Nelson. Adaptation of core mechanisms to generate cell polarity. *Nature*, 422(6933):766–74, 2003.

[71] S. A. Newman and R. Bhat. Dynamical patterning modules: physico-genetic determinants of morphological development and evolution. *Phys. Biol.*, 5(1):066007, 2008.

[72] S. Okuda, Y. Inoue, M. Eiraku, T. Adachi, and Y. Sasai. Vertex dynamics simulations of viscosity-dependent deformation during tissue morphogenesis. *Biomech. Model. Mechanobiol.*, 14(2):413–425, 2015.

[73] T. Okuzono and K. Kawasaki. Intermittent flow behavior of random foams: A computer experiment on foam rheology. *Phys. Rev. E*, 51(2):1246–1253, 1995.

[74] J. M. Osborne, A. Walter, S. K. Kershaw, G. R. Mirams, A. G. Fletcher, P. Pathmanathan, D. Gavaghan, O. E. Jensen, P. K. Maini, and H. M. Byrne.

A hybrid approach to multi-scale modelling of cancer. *Philos. Trans. R. Soc. London, Ser. A*, 368(1930):5013–5028, 2010.

[75] A. B. Patel, W. T. Gibson, M. C. Gibson, and R. Nagpal. Modeling and inferring cleavage patterns in proliferating epithelia. *PLoS Comput. Biol.*, 5(6):e1000412, 2009.

[76] J. Pitt-Francis, P. Pathmanathan, M. O. Bernabeu, R. Bordas, J. Cooper, A. G. Fletcher, G. R. Mirams, P. Murray, J. M. Osborne, A. Walter, S. J. Chapman, A. Garny, I. M. M. Van Leeuwen, P. K. Maini, B. Rodríguez, S. L. Waters, J. P. Whiteley, H. M. Byrne, and D. J. Gavaghan. Chaste: A test-driven approach to software development for biological modelling. *Comput. Phys. Commun.*, 180(12):2452–2471, 2009.

[77] G. Plopper, E. Sikorski, D. Sharp, and B. Lewin. *Lewin's cells.* Burlington, MA : Jones Bartlett, 2015.

[78] P. Sahlin and H. Jönsson. A modeling study on how cell division affects properties of epithelial tissues under isotropic growth. *PLoS ONE*, 5(7):e11750, 2010.

[79] S. A. Sandersius, M. Chuai, C. J. Weijer, and T. J. Newman. Correlating cell behavior with tissue topology in embryonic epithelia. *PLoS ONE*, 6(4):e18081, 2011.

[80] F. Schock and N. Perrimon. Molecular mechanisms of epithelial morphogenesis. *Annu. Rev. Cell Dev. Biol*, 18:463–93, 2002.

[81] M. J. Siedlik and C. M. Nelson. Regulation of tissue morphodynamics: An important role for actomyosin contractility. *Curr. Opin. Genet. Dev.*, 32:80–85, 2015.

[82] I. M. Skerrett and J. B. Williams. A structural and functional comparison of gap junction channels composed of connexins and innexins. *Developmental Neurobiology*, 77(5):522 – 547, 2016.

[83] J Stavans. The evolution of cellular structures. *Rep. Prog. Phys.*, 56(6):733, 1993.

[84] B. Stroustrup. *The C++ programming language.* 3 edition, 1997.

[85] C. M. Van Itallie and J. M. Anderson. Architecture of tight junctions and principles of molecular composition. *Semin. Cell Dev. Biol.*, 36:157–165, 2014.

[86] I. M. M. van Leeuwen, G. R. Mirams, A. Walter, A. Fletcher, P. Murray, J. Osborne, S. Varma, S. J. Young, J. Cooper, B. Doyle, J. Pitt-Francis, L. Momtahan, P. Pathmanathan, J. P. Whiteley, S. J. Chapman, D. J. Gavaghan, O. E. Jensen, J. R. King, P. K. Maini, S. L. Waters, and H. M. Byrne. An integrative computational model for intestinal tissue renewal. *Cell Prolif.*, 42(5):617 – 636, 2009.

[87] G. Vincze, I. Zsoldos, and A. Szasz. On the Aboav-Weaire law. *J. Geom. Phys.*, 51(1):1–12, 2004.

[88] D. Weaire. Some remarks on the arrangement of grains in a polycrystal. *Metallography*, 7(2):157–160, 1974.

[89] D. L. Weaire and S. Hutzler. *The physics of foams.* Oxford University Press, 1999.

[90] Q. Wen and P. A. Janmey. Polymer physics of the cytoskeleton. *Curr. Opin. Solid State Mater. Sci.*, 15(5):177–182, 2011.

[91] S. J. Winder and K. R. Ayscough. Actin-binding proteins. *J. Cell Sci.*, 118(4):651–654, 2005.

[92] L. Wolpert, C. Tickle, A. M. Arias, P. Lawrence, A. Lumsden, E. Robertson, E. Meyerowitz, and J. Smith. In *Principles of Development.* Oxford University Press, Oxford, 5 edition, 2015.

[93] C. Zihni, C. Mills, K. Matter, and M. S. Balda. Tight junctions: from simple barriers to multifunctional molecular gates. *Nat. Rev. Mol. Cell Biol.*, 17(9):564–580, 2016.

[94] D. Zöllner. On the Aboav-Weaire-law for junction limited grain growth in two dimensions. *Comput. Mater. Sci.*, 79:759–762, 2013.